INFORMATION TO USERS

The most advanced technology has been used to photograph and reproduce this manuscript from the microfilm master. UMI films the text directly from the original or copy submitted. Thus, some thesis and dissertation copies are in typewriter face, while others may be from any type of computer printer.

The quality of this reproduction is dependent upon the quality of the copy submitted. Broken or indistinct print, colored or poor quality illustrations and photographs, print bleedthrough, substandard margins, and improper alignment can adversely affect reproduction.

In the unlikely event that the author did not send UMI a complete manuscript and there are missing pages, these will be noted. Also, if unauthorized copyright material had to be removed, a note will indicate the deletion.

Oversize materials (e.g., maps, drawings, charts) are reproduced by sectioning the original, beginning at the upper left-hand corner and continuing from left to right in equal sections with small overlaps. Each original is also photographed in one exposure and is included in reduced form at the back of the book.

Photographs included in the original manuscript have been reproduced xerographically in this copy. Higher quality 6" x 9" black and white photographic prints are available for any photographs or illustrations appearing in this copy for an additional charge. Contact UMI directly to order.

U·M·I

University Microfilms International
A Bell & Howell Information Company
300 North Zeeb Road, Ann Arbor, MI 48106-1346 USA
313/761-4700 800/521-0600

Order Number 9108164

Laser and spectroscopic properties of chromium-doped forsterite

Petričević, Vladimir, Ph.D.

City University of New York, 1990

U·M·I
300 N. Zeeb Rd.
Ann Arbor, MI 48106

LASER AND SPECTROSCOPIC PROPERTIES OF CHROMIUM-DOPED FORSTERITE

A

by

Vladimir Petričević

A dissertation submitted to the Graduate Faculty in Engineering in partial fulfillment of the requirements for the degree of Doctor of Philosophy, The City University of New York.

1990

This manuscript has been read and accepted for the Graduate Faculty in Engineering in satisfaction of the dissertation requirement for the degree of Doctor of Philosophy.

9/28/90
Date

Robert R Alfano
Chair of Examining Committee

9/28/90
Date

Gerard G. Gouesbet
Executive Officer

Professor S. Ahmed
Professor P. Karmel
Professor P. P. Ho
Dr. B. D. Guenther
Dr. F. Allario
Professor S. K. Gayen

Supervisory Committee

The City University of New York

Abstract

LASER AND SPECTROSCOPIC PROPERTIES OF CHROMIUM-DOPED FORSTERITE

by

Vladimir Petričević

Adviser: Robert R. Alfano, Distinguished Professor of Science and Engineering.

This thesis describes the discovery of a new tunable solid state laser, chromium-doped forsterite ($Cr:Mg_2SiO_4$), its spectroscopic, quantum electronic and laser characteristics.

The main goal of spectroscopic investigations was to identify optically active ions in chromium-doped forsterite. The spectroscopic studies performed on $Cr:Mg_2SiO_4$ crystals grown under different conditions include: measurements of the polarized absorption and fluorescence spectra, polarized excitation spectra, temperature and wavelength dependence of the fluorescence lifetime, relative quantum efficiency, and theoretical calculations using Tanabe-Sugano formalism. The conclusions based on these measurements and calculations are as follows. (1) There are at least three inequivalent optically active centers in chromium-doped forsterite. (2) Trivalent chromium (Cr^{3+}) substitutes for divalent magnesium (Mg^{2+}) in two distinct octahedrally coordinated sites, one with mirror (C_s) and the other with inversion (C_i) symmetry. (3) Tetravalent chromium (Cr^{4+}) substitutes for tetrahedrally coordinated silicon (Si^{4+}). (4) Absorption and emission spectra show contributions from all three centers. (5) Center responsible for laser operation in the near-infrared spectral region is tetrahedral Cr^{4+} ion.

Laser properties of chromium-doped forsterite for different modes of operation were investigated. Pulsed laser operation was obtained for 532-nm, 578-nm, 629-nm, and 1064-nm pumping, with repetition rate ranging from 10 Hz to 6.5 kHz. Tuning range covers the 1167 - 1345 nm wavelength region. Highest slope efficiency for pulsed operation obtained so far is ~23%. Continuous-wave operation was demonstrated by pumping the crystal with the 1064-nm radiation from a cw Nd:YAG laser. Highest slope efficiency for continuous-wave operation is ~38%. Limiting slope efficiency that may be obtained if all passive losses are eliminated is estimated to be >65%. Effective gain cross section was measured using the pump-and-probe technique. The peak gain cross section is estimated to be 1.9×10^{-19} cm^2 at 1215 nm which is comparable to the peak value of ~2.1×10^{-19} cm^2 predicted by fluorescence linewidth and lifetime measurements. The results of the effective gain measurements indicate that excited-state absorption is not a major loss mechanism in chromium-doped forsterite laser for wavelengths shorter than 1.3 μm. There is an indication of the onset of weak excited-state absorption in the wavelength region beyond 1.3 μm.

Further research and development of chromium-doped forsterite laser is suggested. The research to be performed is devoted to investigation of fundamental processes in this crystal such as nonradiative transition and phonon dynamics. The development aspect of this project points to various modes of operation, such as flashlamp-pumped operation, diode pumping, active and passive mode locking and Q-switching and building different configurations of oscillators and amplifiers for applications. The development of new lasers based on tetravalent chromium and other transition metal ions with identical electronic configuration in various host crystals is proposed.

To my parents, Vaso and Slavče Petričević.

ACKNOWLEDGMENTS

I would like to gratefuly acknowledge my thesis adviser Robert R. Alfano, Distinguished Professor of Science and Engineering, for his patient guidance, rigorous training, critical reviewing of all my work and most of all, for his creative discussions and suggestions during the course of this research. Most importantly, this thesis research would not have taken place without his recognizing the potential of the forsterite crystal.

I am particularly grateful to Professor Swapan K. Gayen for his valuable theoretical and experimental instruction and fruitful cooperation. His presence and support during the most critical period of my research is deeply appreciated.

I wish to express my sincere thanks to Professor Roger Dorsinville for his advice, support and valuable discussions.

I am grateful to Dr. Bob Guenther of Army Research Office and Dr. Frank Allario of NASA Langley Research Center who made this research possible by providing the financial support and who closely and enthusiastically followed the exciting developments of this research.

I would like to express my appreciation to Mitsui Mining and Smelting Company of Japan for providing the forsterite crystals used in this research.

I am grateful to Professors Samir Ahmed, Paul Karmel and Ping Pei Ho for serving on the doctoral committee.

I would also like to thank Antonios Seas and Yuri Budansky for their friendly support and valuable technical assistance.

TABLE OF CONTENTS

LIST OF FIGURES

CHAPTER 1

CHAPTER 2

CHAPTER 3

CHAPTER 5

LIST OF TABLES

CHAPTER 2

CHAPTER 3

CHAPTER 4

CHAPTER 5

CHAPTER 1

INTRODUCTION

1.1 Tunable Solid-State Lasers

Eversince the first report of laser action in ruby[1] in 1960, solid-state lasers have been used as reliable sources of coherent optical radiation for various applications. Most of the existing solid-state lasers use dielectric hosts containing paramagnetic ions.[2] Host materials vary from glasses to single crystals. Due to superior thermomechanical properties crystalline hosts are more attractive for most applications. Active ions in these hosts come from two groups of elements: the transition-metal group and the rare-earth group of ions in the Periodic Table. The majority of transition-metal ion-doped crystals are characterized by broad fluorescence bands which can be utilized for wavelength-tunable laser operation. These tunable solid-state lasers form an important class of lasers belonging to a larger group of tunable lasers which, before the first successful room-temperature laser operation of alexandrite[3] in 1979, consisted mainly of various gas and organic dye lasers. Gas lasers usually exhibit laser action on several discrete wavelengths, while organic dye lasers can be tuned continuously over a relatively wide spectral range.

The first tunable laser operation was that of flashlamp-pumped Ni^{2+}:MgF_2.[4] Soon after that, laser operation was obtained in a variety of Ni^{2+}-, Co^{2+}-, and V^{2+}-doped host crystals.[5-7] However, these lasers had several disadvantages, the most

serious one being the need for cryogenic cooling. This disadvantage, together with the appearance of tunable dye lasers, caused reduced interest in further research on tunable solid-state lasers. There were no major advances reported until late 1970s.

The major breakthrough in the field of tunable solid-state laser occured in 1979 with the first room-temperature, broadly wavelength-tunable laser operation in alexandrite,[3,8] (Cr^{3+}-doped $BeAl_2O_4$), and soon afterwords, in emerald,[9,10] (Cr^{3+}-doped $Be_3Al_2(SiO_3)_6$).

Prompted by the successful operation of alexandrite and emerald lasers, the surge in research activities on tunable solid-state lasers has been extensive in the 1980s. The thrust of these research endeavors has been twofold: first to look for new host materials for the trivalent chromium ion, and second, to search for new ions that will exhibit laser action in commonly used host crysatals. These efforts have been rewarded by the successful wavelength-tunable laser operation of Cr^{3+} in a number of hosts,[11-13] by the discovery of a new lasing ion trivalent titanium (Ti^{3+}),[14,15] as well as by "rediscovery"[16-21] of tunable phonon-terminated lasers based on divalent ions Ni^{2+}, Co^{2+}, and V^{2+}.

As a consequence of these research efforts, during the last 10 years tunable solid-state lasers have emerged as an alternative to dye lasers. Although dye lasers have significant advantages, such as high gain and low cost, many disadvantages, such as toxicity, poor long term reliability, and narrow tuning range when compared to solid-state lasers, make dye lasers unsuitable for hospital, airborne, mobile or spaceborne use. Tunable solid-state lasers are more expensive to build and are characterized by lower gain coefficient. However, the importance of tunable solid-state lasers stems from their many advantages over dye lasers, such as broad tuning range, high reliability, compactness (particularly when pumped by semiconductor

diode lasers), and longer operational lifetime. These properties make them suitable for spaceborne remote sensing, ranging, lidar and optical communications. Tunable solid-state lasers also have a high potential for various medical, industrial, and basic scientific research applications.

1.2 Thesis Statement and Organization

The subject of this thesis is the discovery of chromium-doped forsterite ($Cr:Mg_2SiO_4$), a new tunable solid-state laser crystal with many unique properties, and the study of its spectroscopic and laser characteristics. Chromium-doped forsterite laser has emerged as an important member of the ever growing family of tunable solid-state lasers based on chromium ion as the lasing center. Both pulsed and continuous-wave laser operation have been obtained for 532-nm (doubled Nd:YAG), 578-nm (copper-vapor laser), 629-nm (SRS of 532-nm frequency-doubled Nd:YAG radiation in ethanol), and 1064-nm (fundamental Nd:YAG radiation) pumping.[21-23,26] Pulsed operation with repetition rate from 10 Hz (Q-switched Nd:YAG) to 6.5 kHz (copper vapor laser) has been demonstrated. The tuning range covers the 1167 - 1345 nm spectral range.[24] This wavelength range is of great technological importance since it covers the region of minimal dispersion in optical fibers. Together with the chromium-based lasers tabulated by Payne et al.,[11] and more recently developed chromium-doped crystals of Ca-gallogermanate structure,[12] as well as chromium-doped YAG crystal,[13] lasers based on chromium ion as the active center now span the broad spectral range of 695 -1450 nm. The most interesting and distinguishing feature of laser action in $Cr:Mg_2SiO_4$, which will be apparent from research in this thesis, is that the lasing ion is not trivalent chromium (Cr^{3+}), as is the case with the rest of the chromium-based lasers.

Available experimental data presented in this thesis suggest that the active ion in this crystal is tetravalent chromium (Cr^{4+}).[23,26-29]

$Cr:Mg_2SiO_4$ is the first laser crystal in which the laser-active center is identified as tetravalent chromium.[23,26] As of this writing, chromium-doped forsterite is the only laser, besides Cr:YAG,[13] where tetravalent chromium is the ion responsible for laser action. A list of most important chromium-doped tunable solid-state lasers with corresponding tuning ranges is shown in Figure 1.2.1.

The thesis research has three goals: 1. Spectroscopic measurements and calculations, 2. Measurements of laser characteristics of the chromium-doped forsterite laser, and 3. Measurements of the effective gain cross section. The objective of the thesis study is to fully understand the complex spectroscopic properties of Cr:forsterite, explain its basic physical properties relevant to laser operation, and evaluate and improve the performance of this new important laser system.

In the first part of the thesis, basic spectroscopic measurements in $Cr:Mg_2Si0_4$, such as room-temperature and liquid-nitrogen temperature absorption and fluorescence spectra were investigated to determine the potentials of this crystal as a laser material and to obtain design parameters for laser cavity to be used in lasing experiments.

Room temperature and liquid nitrogen temperature absorption and fluorescence spectra of Cr:forsterite, its excitation spectra measured at two different wavelengths, as well as laser operation for both 532-nm and 1064-nm pumping, which will be described in the second part, clearly indicate that a center other than

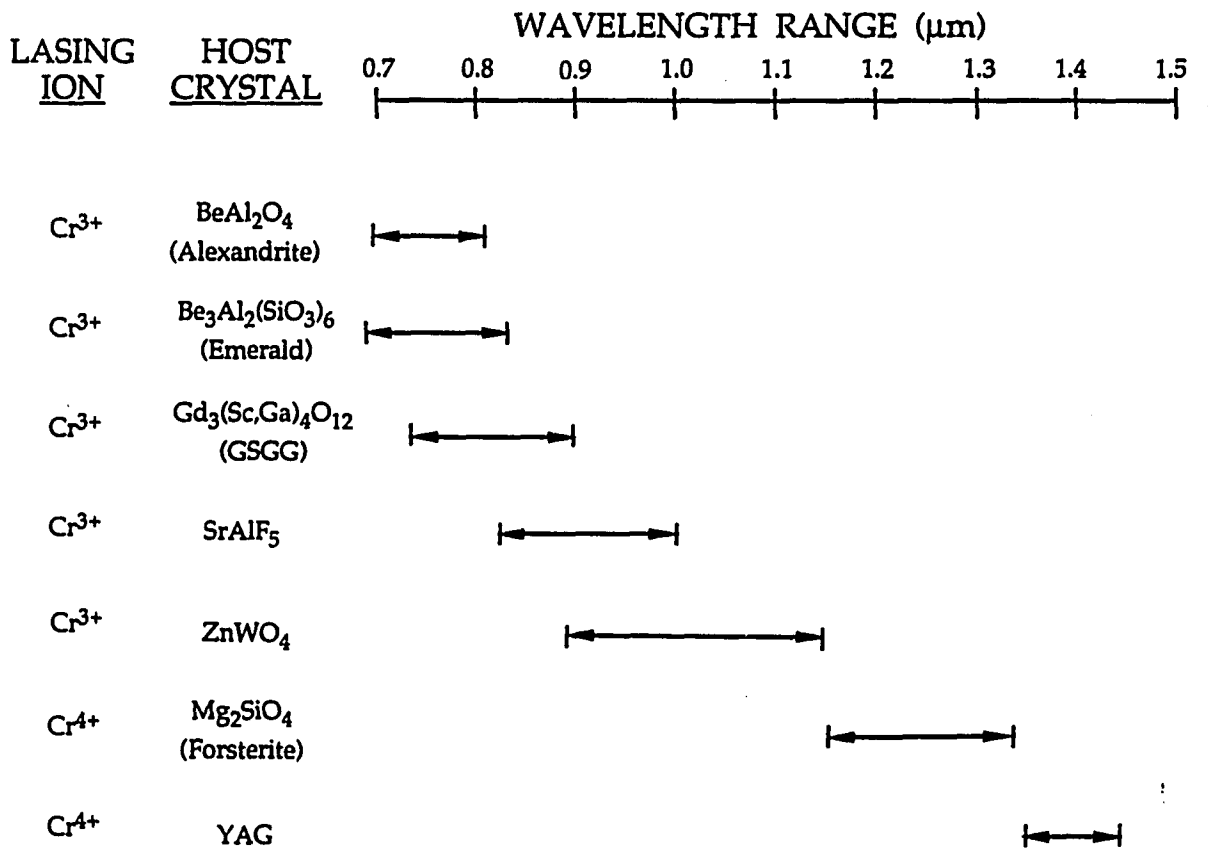

Fig. 1.2.1 Most important chromium-based tunable solid state lasers and their tuning ranges.

the trivalent chromium (Cr^{3+}) is responsible for the 850-1200 nm absorption and for the laser action in the near infrared. Spectroscopic research was performed to show that this center is tetravalent chromium (Cr^{4+}) in a tetrahedrally coordinated site where it substitutes for Si^{4+}. This hypothesis is supported by comparing the bands in the absorption spectrum and transitions predicted by Tanabe-Sugano diagrams for tetrahedral and octahedral coordination. Theoretical calculations were done to account for the peaks observed in the absorption spectrum. From the absorption spectrum, bands are assigned to Cr^{3+} and Cr^{4+} transitions. To account for all the features of the spectrum the same formalism was used simultaneously for Cr^{3+} in an octahedrally coordinated site and Cr^{4+} in tetrahedral site, by using corresponding Tanabe-Sugano diagrams and theoretical computations based on the Tanabe-Sugano formalism.

Further evidence to support the Cr^{4+} hypothesis was obtained from studying chromium-doped forsterite crystals grown under different conditions. It is expected that crystals grown in reducing atmosphere show mostly Cr^{3+} transitions in the absorption spectrum, whereas crystals grown in oxidizing atmosphere show more of Cr^{4+} features in the spectrum, such as enhanced absorption in the 850-1100 nm region. The results of these spectroscopic measurements were compared with theoretical calculations.

The hypothesis that there are several inequivalent optically active centers in chromium-doped forsterite is further substantiated by measuring the excitation spectra and performing time resolved measurements to determine fluorescence lifetimes corresponding to different chromium ions in different sites.

The following approaches were taken in order to explain spectroscopic properties of chromium-doped forsterite:

A. Study Cr:Mg_2SiO_4 crystals grown under different growing conditions by measuring:

1. Polarized absorption and fluorescence spectra at room-temperature and liquid nitrogen temperature.

2. Temperature dependence of the fluorescence lifetime as a function of wavelength.

3. Relative quantum efficiency.

4. Polarized excitation spectra.

B. Use the Tanabe-Sugano formalism to qualitatively explain the features of Cr:Mg_2SiO_4 spectra for crystals grown under different growing conditions.

The second part of the thesis deals with the laser performance of the chromium-doped forsterite laser for different modes of operation. This part is divided in three sections:

A. In the first section room temperature-pulsed laser action in Cr:Mg_2SiO_4 for both 532 nm and 1064 nm excitation is described. Basic parameters of pulsed laser action, such as slope efficiency and the spectrum of the laser emission, are presented. The highest slope efficiency of Cr:forsterite laser was measured to be 23%. By meausuring laser parameters, such as slope efficiency and lasing threshold energy for different laser cavities, gain cross section and passive loss were estimated.

B. Continuous wavelength-tunable operation has been demonstrated and is presented in this section. Tuning was accomplished by using a birefringent plate as

an intracavity wavelength-selective element. Tuning range spans the 1167 - 1345 nm wavelength region.

C. Continuous-wave laser operation at room temperature has been obtained. Output power slope efficiency and spectrum of the laser emission were measured. Gain cross section, passive loss and threshold population inversion were calculated by using experimental data. Slope efficiencies were measured for three different output couplers in order to determine the limiting slope efficiency, which is possible to achieve in chromium-doped forsterite laser in the absence of passive losses.

The topic of the third part of the thesis is measurements of the effective gain cross section and estimate of the effect of excited-state absorption. Effective gain measurements were performed using a standard pump-and-probe experimental arrangement. The effective (net) gain cross section was measured over the part of the lasing wavelength region. The results of the pump-and-probe mesurements were compared with the gain cross section values predicted using data obtained by spectroscopic measurements. The close agreement between the measured and the predicted values indicates that excited-state absorption is not a major loss mechanism in chromium-doped forsterite laser.

The final chapter of the thesis gives my conclusions and describes the possible future research.

1.3 References

1. T. H. Maiman, Nature **187**, 493 (1960).

2. P. F. Moulton, Tunable Paramagnetic-Ion Lasers, in: *Laser Handbook*, edited by M. Bass and M. L. Stitch, Elseviers Science Publishers B. V., (1985).

3. J. C. Walling, H. P. Jenssen, R. C. Morris, E. W. O'Dell, and O. G. Peterson, Opt. Lett. **4**, 182 (1979).

4. L. F. Johnson, R. E. Dietz, and H. J. Guggenheim, Phys. Rev. Lett. **11**, 318 (1963).

5. L. F. Johnson, R. E. Dietz, and H. J. Guggenheim, Appl. Phys. Lett. **5**, 21 (1964).

6. L. F. Johnson, R. E. Dietz, H. J. Guggenheim, and R. A. Thomas, Phys. Rev. **149**, 179 (1966).

7. L. F. Johnson and H. J. Guggenheim, J. Appl. Phys. **38**, 4837 (1967).

8. J. C. Walling, H. P. Jenssen, R. C. Morris, E. W. O'Dell, and O. G. Peterson, IEEE J. Quantum Electron. **QE-16**, 1302 (1980).

9. M. L. Shand and J. C. Walling, IEEE J. Quantum Electron. **QE-18**, 1829 (1982).

10. J. Buchert, A. Katz, and R. R. Alfano, IEEE J. Quantum Electron. **QE-19**, 1477 (1983); and R. R. Alfano and J. Buchert, U. S. Patent No. 4,464,761, August 7, 1984.

11. S. A. Payne, L. L. Chase, L. K. Smith, W. L. Kway, and H. W. Newkirk, J. Appl. Phys. **66**, 1051 (1989).

12. A. A. Kaminskii, A. V. Butashin, A. A. Demidovich, V. G. Koptev, B. V. Mill, and A. P. Shkadarevich, Phys. Stat. Sol. (a) **112**, 197 (1989).

13. N. B. Angert, N. I. Borodin, V. M. Garmash, V. A. Zhitnyuk, A. G. Okhrimchuk, O. G. Siyuchenko, and A. V. Shestakov, Sov. J. Quantum Electron. **18**, 73 (1988).

14. P. F. Moulton, J. Opt. Soc. Am. B **3**, 125 (1986).

15. A. I. Alimpiev, G. V. Bukin, V. N. Matrosov, E. V. Pestryakov, V. P. Solntsev, V. I Trunov, E. G. Tsvetkov, and V. P. Chebotaev, Sov. J. Quantum Electron. **16**, 579 (1986).

16. P. F. Moulton and A. Mooradian, Appl. Phys. Lett. 35, 838 (1979).

17. P. F. Moulton, IEEE J. Quantum Electron. **QE-18**, 1185 (1982).

18. P. F. Moulton, IEEE J. Quantum Electron. **QE-21**, 1582 (1985).

19. V. Brauch and U. Durr, Opt. Commun. **55**, 35 (1985).

20. W. E. Knierim, A. Honold, V. Brauch, and U. Durr, J. Opt. Soc. Am. B **3**,119 (1986) and references therein.

21. V. Petričević, S. K. Gayen, R. R. Alfano, K. Yamagishi, H. Anzai, and Y. Yamaguchi, Appl. Phys. Lett. **52**, 1040 (1988).

22. V. Petričević, S. K. Gayen, and R. R. Alfano, Appl. Opt. **27**, 4162 (1988).

23. V. Petričević, S. K. Gayen, and R. R. Alfano, Appl. Phys. Lett. **53**, 2590 (1988).

24. V. Petričević, S. K. Gayen, and R. R. Alfano, Appl. Opt. **28**, 1609 (1989).

25. V. Petričević, S. K. Gayen, and R. R. Alfano, Opt. Lett. **14**, 612 (1989).

26. H. R. Verdun, L. M. Thomas, D. M. Andrauskas, T. McCollum, and A. Pinto, Appl. Phys. Lett. **53**, 2593 (1988)

27. V. Petričević, S. K. Gayen, and R. R. Alfano, in *Tunable Solid-State Lasers*, Vol. 5 of the OSA Proceeding Series, M. L. Shand and H. P. Jenssen, eds. (Optical Society of America, Washington, D.C., 1989), pp. 77-84.

28. H. R. Verdun, L. M. Thomas, and D. M. Andrauskas, in *Tunable Solid-State Lasers*, Vol. 5 of the OSA Proceeding Series, M. L. Shand and H. P. Jenssen, eds. (Optical Society of America, Washington, D.C., 1989), pp. 85-92.

29. R. Moncorge, D. J. Simkin, G. Cormier, and J. A. Capobianco, in *Tunable Solid-State Lasers*, Vol. 5 of the OSA Proceeding Series, M. L. Shand and H. P. Jenssen, eds. (Optical Society of America, Washington, D.C., 1989), pp. 93-97.

CHAPTER 2

SPECTROSCOPIC IDENTIFICATION OF THE LASING CENTER IN CHROMIUM-DOPED FORSTERITE

2. 1 Introduction

Chromium-doped forsterite ($Cr:Mg_2SiO_4$) has emerged[1-7] as an important member of the growing family of tunable solid-state lasers based on chromium ion as the lasing center. Besides the development as a practical laser system, chromium-doped forsterite has continued to receive attention due to its most unusual and intriguing spectroscopic properties. The most interesting and distinguishing feature of laser action in $Cr:Mg_2SiO_4$ is that the lasing ion is not the trivalent chromium (Cr^{3+}) in octahedral site as is the case with the rest of the chromium-based lasers. Available experimental data suggest that the active ion responsible for laser action is tetrahedrally coordinated tetravalent chromium (Cr^{4+}).[4,5,8-10] This has opened up the possibility of developing crystals in which Cr^{4+} will be the only active ion. Such crystals have potential for extending the tuning range of chromium-based lasers further into the near infrared than is currently possible with Cr^{3+}-doped crystals.[11,12] The potential for extending the tuning range of Cr^{4+}-based systems further into infrared has already been demonstrated by the successful operation of Cr:YAG laser.[13]

The identification of the tetravalent chromium ion as the lasing ion in Cr:forsterite has been one of the most important goals of this thesis. In this chapter,

measurements of the absorption, excitation and fluorescence spectra as well as the fluorescence lifetime in three chromium-doped forsterite crystals grown under different conditions are presented. The crystal grown in a relatively reducing atmosphere contains fewer Cr^{4+} ions and more Cr^{3+} ions, than the sample grown in an oxidizing atmosphere. A detailed comparison of the spectroscopic properties of the three samples, as well as theoretical considerations, indicate that the lasing ion is tetravalent chromium.

In section 2.2 basic physical properties of Cr-doped forsterite crystal are reviewed and the three samples that were used in this study are described. Section 2.3 outlines the experimental methods and parameters, while section 2.4 details the experimental results. Implications of these results are then discussed in section 2.5 and in section 2.6 conclusions are drawn.

2.2 Crystal Structure and Samples Characteristics

Forsterite (Mg_2SiO_4) is a member of the olivine family of crystals and is a naturally occuring gem. Single crystals of chromium-doped forsterite have been grown successfully using the Czochralski method,[14,15] as well as the laser-heated-pedestal-growth (LHPG) technique.[5] Some basic physical properties of forsterite compared with YAG crystal are listed in Table 2.2.1.

A unit cell of forsterite has four formula units in an orthorhombic structure of the space group Pbnm.[16,17] The unit cell dimensions are a =4.76 Å, b =10.22 Å and c =5.99 Å. A unit cell of Mg_2SiO_4 viewed along the c axis is shown in Fig. 2.2.1. Trivalent chromium (Cr^{3+}) enters substitutionally for the divalent magnesium (Mg^{2+}) ion in two crystallographically distinct octahedrally coordinated sites:

TABLE 2.2.1: Basic Physical Properties of Forsterite and YAG Crystals

Property	Forsterite	YAG
Chemical Formula	Mg_2SiO_4	$Y_3Al_5O_{12}$
Melting Point (° C)	1890	1970
Density (g/cm^3)	3.22	4.56
Moh's Hardness	7	8.5
Thermal Expansion Coefficient	9.5×10^{-6}	8.0×10^{-6}
Thermal Conductivity (W/cmK)	0.08 (@ 300 K)	0.13 (@ 300 K)
dn/dT (K^{-1})	Not Measured	7.3×10^{-6}
Index of Refraction	1.635	1.82 (@ 1.0 μm)

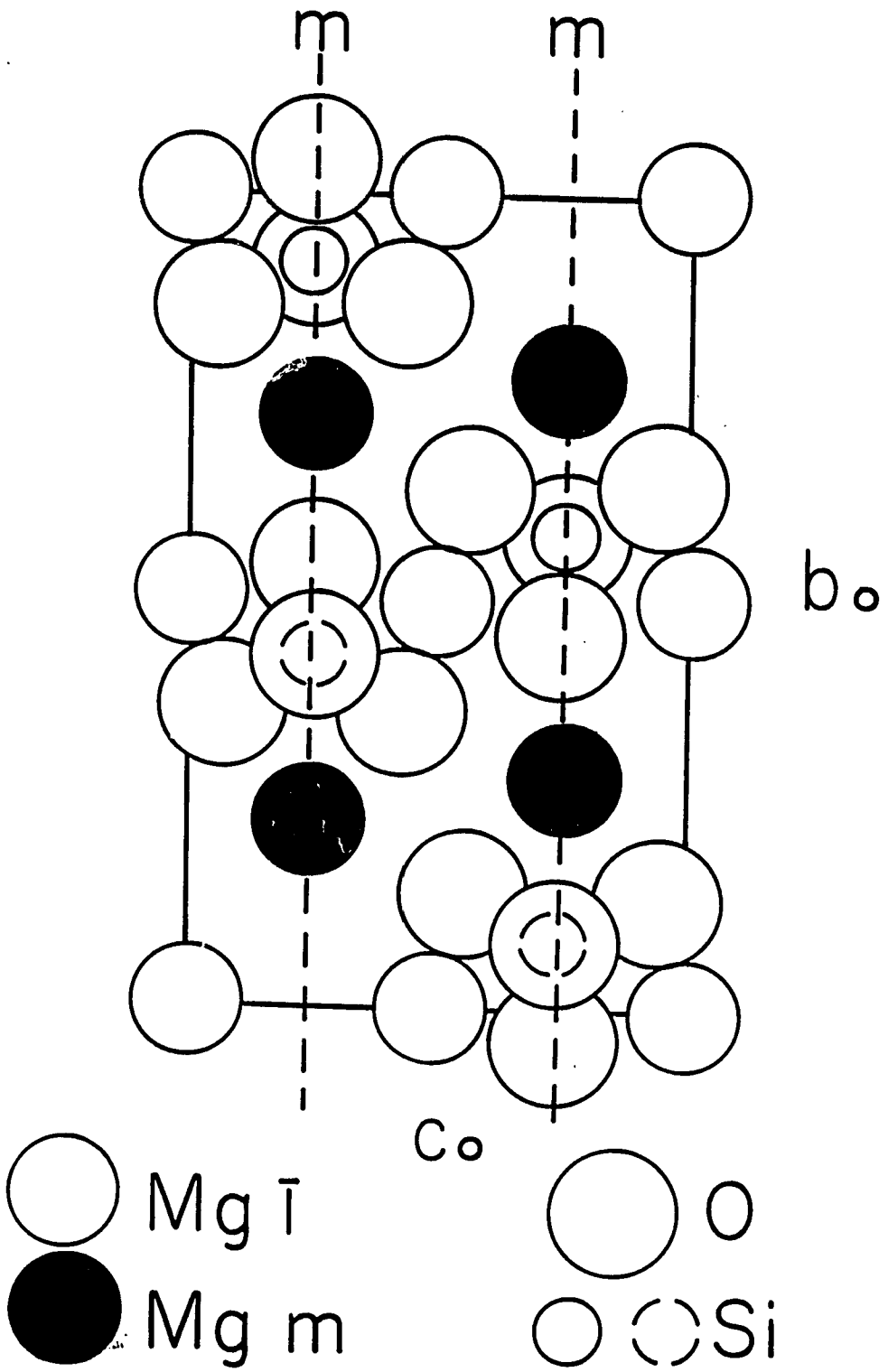

Fig. 2.2.1 Unit cell of forsterite (Mg_2SiO_4) viewed along the *a* axis using Pbnm orientation (after Ref. 17).

one with inversion symmetry (C_i), and the other with mirror symmetry (C_s). The method of charge compensation is not well understood. The occupation ratio of the inversion to mirror sites by Cr^{3+} ions is 3:2. The occupancy of the two sites in that ratio has been verified by EPR and ENDOR measurements.[18,19]

Earlier spectroscopic work[15] on chromium-doped forsterite was based on the assumption that the trivalent chromium substituting for magnesium is the only optically active ion in chromium-doped forsterite. The unusual features in the absorption spectra observed by those authors, particularly the absence of the violet-blue absorption band characteristic for Cr^{3+} in octahedral field, was explained by considering a reduced symmetry of the mirror site in Mg_2SiO_4. However, subsequent laser operation of Cr:forsterite for infrared pumping[3-5] and spectroscopic investigations[8-10] of the system have promoted the hypothesis that in addition to Cr^{3+}, tetravalent chromium (Cr^{4+}) is present in forsterite grown in an atmosphere containing oxygen, and is responsible for laser action. The Cr^{4+} ion is presumed to substitute for the Si^{4+} ion, which is tetrahedrally coordinated by four oxygen ions.

All three single crystals of chromium-doped forsterite used in this study were grown by the Czochralski method at the Electronic Materials Research Laboratory of the Mitsui Mining and Smelting Co., Ltd., Japan. The first sample (referred to as sample 1, henceforth), used for initial spectroscopic and laser experiments is a 4.5 mm x 9 mm x 9 mm rectangular parallelepiped with the three mutually orthogonal axes oriented along the *b*, *c*, and *a* crystallographic axes of the crystal. The *a* axis is parallel to the 4.5 mm side of the crystal and perpendicular to the 9 mm x 9 mm face. The crystal contains 0.04 at. % of Cr ions, which is equivalent to a chromium ion concentration of 1.1×10^{19} ions/cm^3. Growing conditions for sample 1 are not known, but presence of Cr^{4+} features in the absorption spectra indicate that growing

TABLE 2.2.2: Cr: Mg_2SiO_4 Crystals Used in Spectroscopic and Laser Measurements

Sample #	Dimension in millimeters	Total Cr-ion Concentration	Growth Atmosphere (Oxygen Partial Presssure)	Optically Active Ions and Coordination
1	4.5 x 9 x 9	~1.1 x 10^{19}	Oxidizing (~1 %)	Cr^{3+}(oct), Cr^{4+}(tet)
2	30 x 6 x 6	~5.5 x 10^{18}	Oxidizing (~1 %)	Cr^{3+}(oct), Cr^{4+}(tet)
3	30 x 6 x 6	~5.5 x 10^{18}	Reducing (~0.01 %)	Cr^{2+}(oct), Cr^{3+}(oct)

atmosphere must have been partly oxidizing. The other two crystals are 30 mm x 6 mm x 6 mm rectangular parallelepipeds with three mutually orthogonal axes oriented along the *a, b, c* crystallographic axes. The *a* axis is perpendicular to the 6 mm x 6 mm face of the crystal in both the samples. The chromium ion concentration in these two crystals is ~5.5 x 10^{18} cm^{-3}. The relative concentration of Cr^{4+} and Cr^{3+} ions was found to depend strongly on the growth atmosphere. By growing the crystal in a reducing atmosphere the concentration of Cr^{4+} ions can be decreased and that of Cr^{3+} increased. The growth atmosphere is usually a controlled mixture of oxygen and nitrogen. Since $Cr:Mg_2SiO_4$ has relatively high melting temperature (1890 ^{o}C, see Table 2.2.1), iridium crucible must be used to contain the melt. Oxygen partial pressure cannot exceed 3% in order to prevent crucible erosion. One of our samples was grown in a more oxidizing (~1% oxygen partial pressure) atmosphere (sample 2), while the other (sample 3) was grown in a more reducing atmosphere (less than 0.01 % oxygen partial pressure. Properties of the three samples studied in this thesis are summarized in Table 2.2.2.

2.3 Experimental Methods

The absorption spectra of all samples of $Cr:Mg_2SiO_4$ used in this study were taken with a Perkin-Elmer Lambda-9 spectrophotometer. The fluorescence spectra were excited by a chopped 488-nm excitation from an Ar^{+}-ion laser. Fluorescence was detected by a Hamamatsu P394A uncooled PbS detector and PAR Model HR-8 lock-in amplifier. PbS detector was placed at the exit slit of a SPEX Minimate 0.25-m monochromator equipped with a 1000-nm blazed grating. To resolve features at shorter wavelengths the PbS detector was supplemented by a photomultiplier tube with S-20 response. Chopped 1064-nm radiation from a Spectra Physics cw Nd:YAG

laser was also used to selectively excite the Cr^{4+} transitions. Basic experimental setup for fluorescence measurements is shown in Fig. 2.3.1.

The excitation spectra were measured by monitoring the intensity of emission in two different wavelength ranges, around λ = 900 nm and λ > 1100 nm as a function of excitation wavelength. The unpolarized radiation from a 1 kW Oriel tungsten halogen lamp was passed through a monochromator to produce a continuously tunable excitation source. The excitation beam was polarized using a Glan-Thompson polarizer after the exit slit of the monochromator. The beam was chopped and focused onto the sample. The fluorescence intensity for λ > 1100 nm was monitored by a PbS detector with a long-pass filter and lock-in amplifier. The fluorescence at 900 nm was measured using a photomultiplier tube with S-1 response with a 900-nm narrow-band filter and lock-in amplifier. The experimental setup is shown in Fig. 2.3.2.

The fluorescence lifetime in the 800-1400 nm spectral range was measured using a streak camera (Hamamatsu model C 1587 with M1953 slow single-sweep unit) coupled to a spectrometer. The emission in the 1100-1400 nm range was excited by 1064-nm pulsed radiation from a Q-switched Nd:YAG laser, while that in the 800-1100 nm range by the second harmonic (532 nm) radiation of the same laser. Fluorescence lifetime around 700 nm was measured by a photomultiplier tube with S-20 response and an oscilloscope using pulsed 532-nm radiation as the excitation source. The experimental arrangement for measurements of the fluorescence lifetime is shown schematically in Fig. 2.3.3.

Absorption and fluorescence spectra and fluorescence lifetime were measured as a function of sample temperature as well.

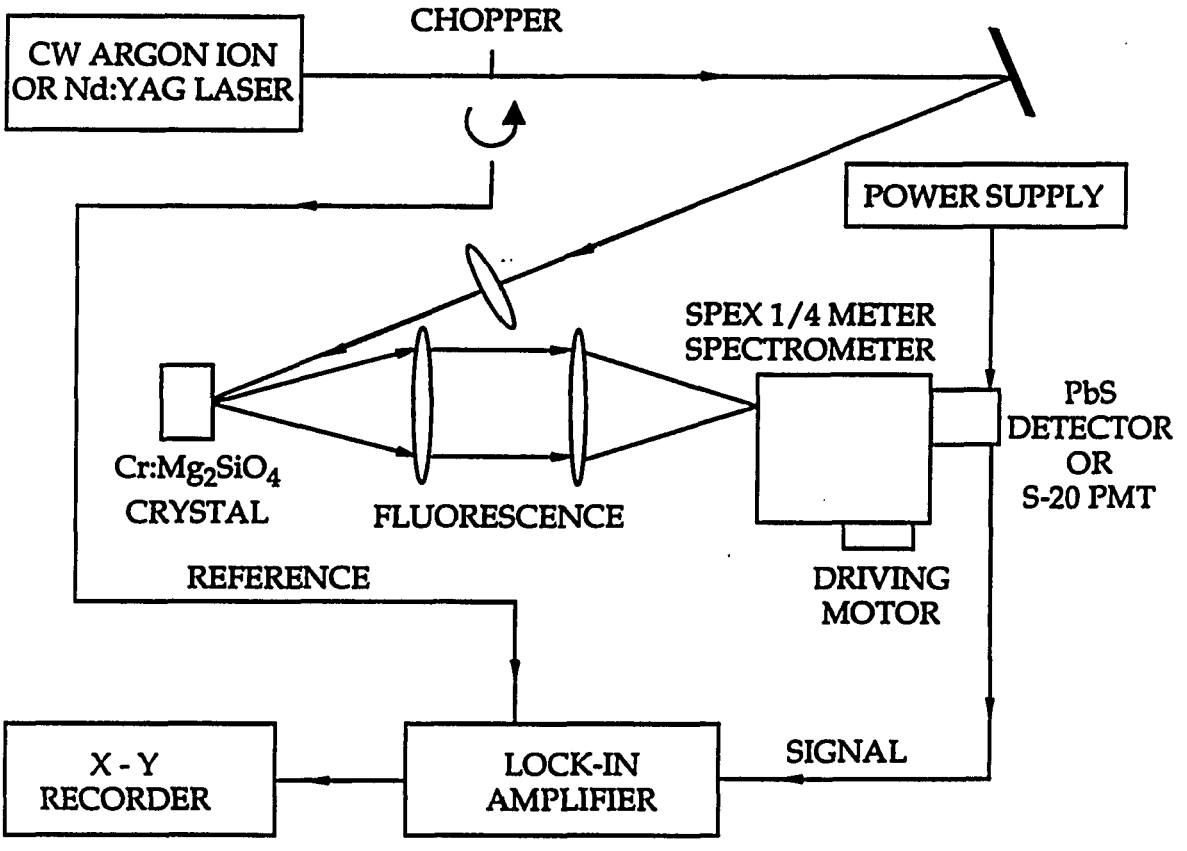

Fig. 2.3.1 Experimental setup for measurement of the fluorescence spectra of Cr: Mg_2SiO_4.

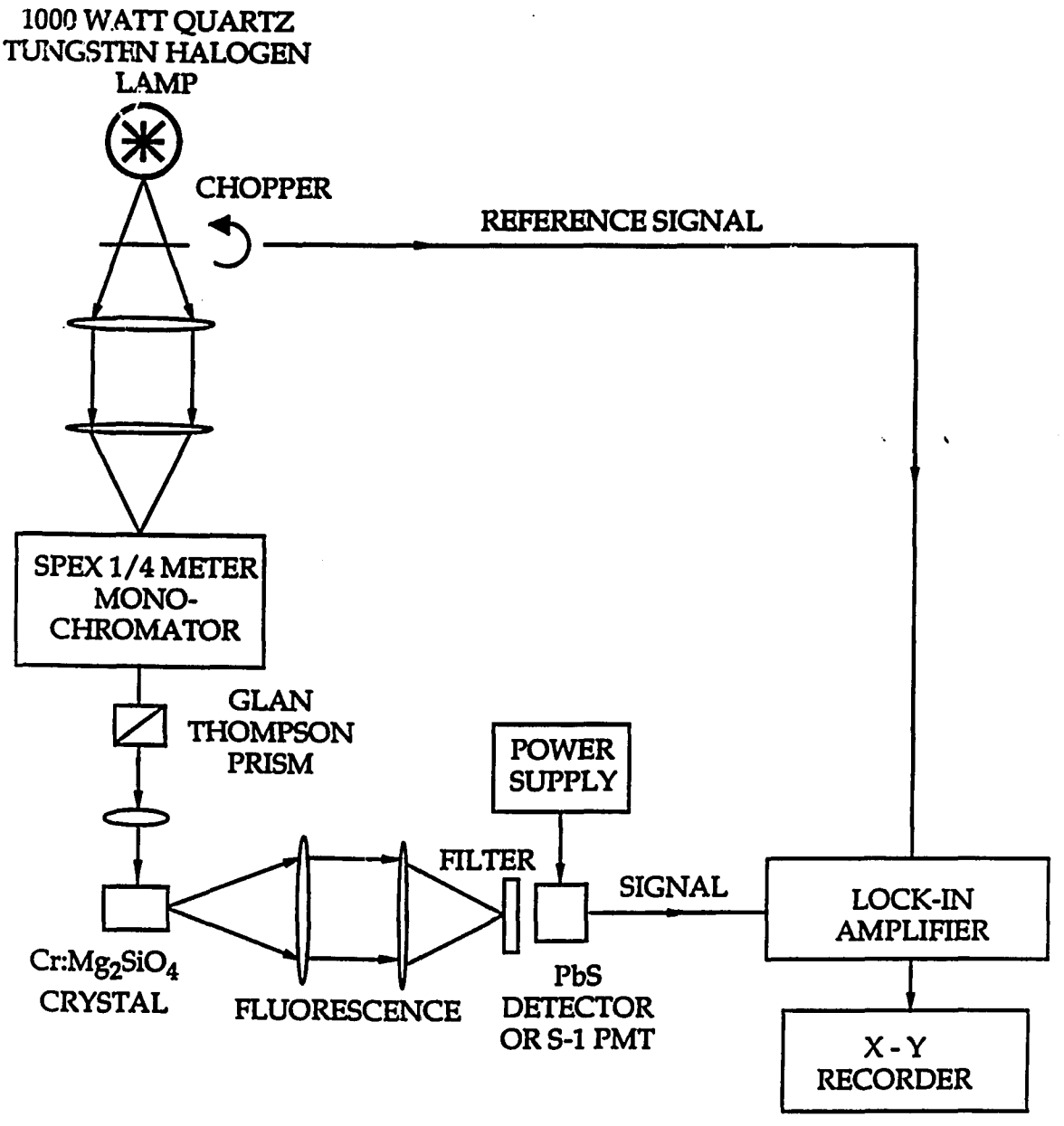

Fig. 2.3.2 Experimental setup for measurement of the excitation spectra of Cr: Mg_2SiO_4.

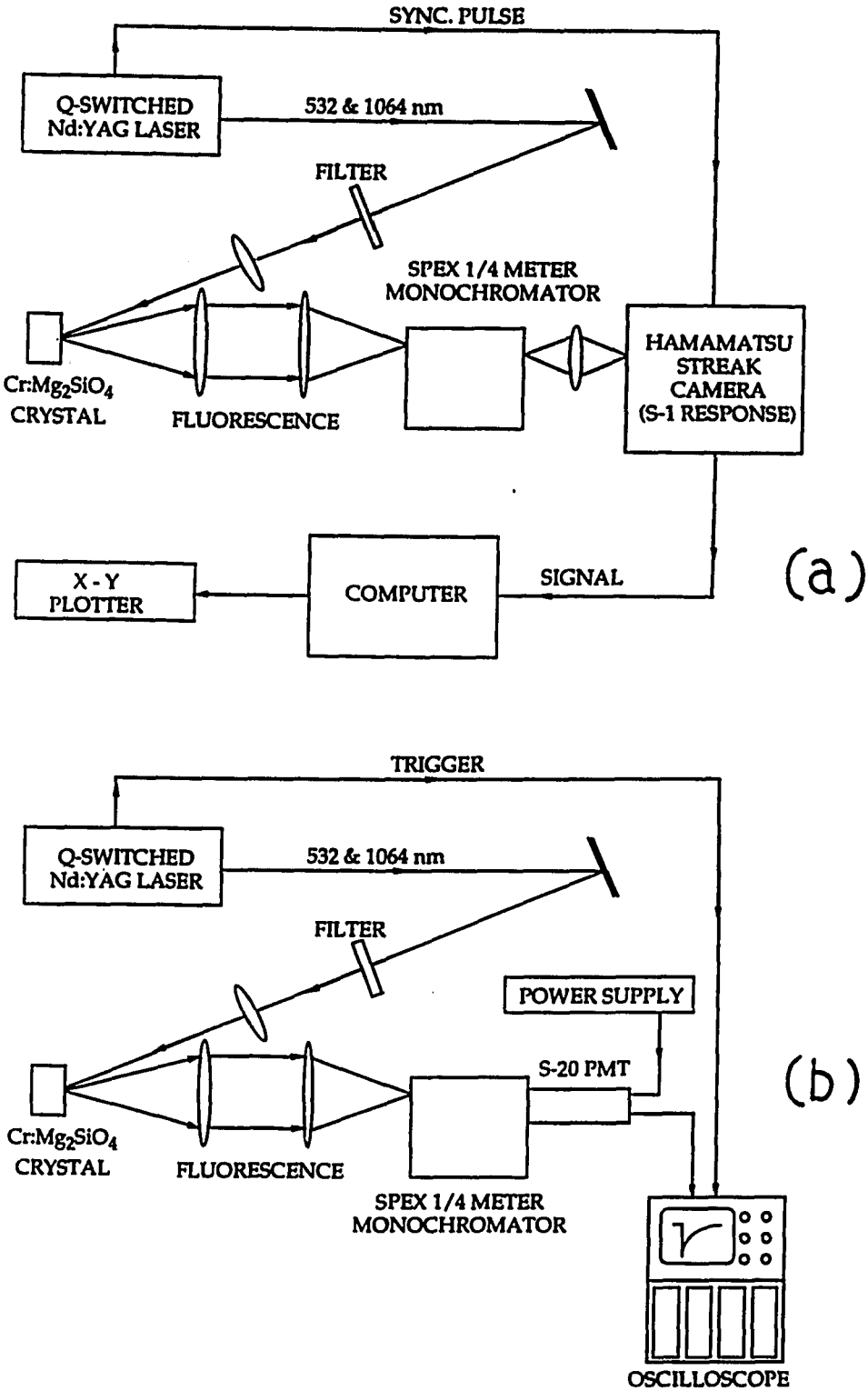

Fig. 2.3.3 Experimental setup for measurement of the fluorescence lifetime in Cr: Mg_2SiO_4: (a) using a streak camera, and (b) using a photomultiplier tube and oscilloscope.

2.4 Experimental Results and Discussion

2.4.1 Absorption Spectra

The absorption spectra of $Cr:Mg_2SiO_4$ grown under standard conditions, (samples 1 and 2), show identical features, the only difference being the factor-of-two lower absorbance measured for sample 2 due to lower chromium ion concentration. Relative distribution of Cr^{3+} and Cr^{4+} ions is the same in both the samples, since the factor-of-two difference between the two spectra appears to hold for both Cr^{3+} and Cr^{4+} peaks in the spectra. The absorption spectra of sample 2 for different orientation of the crystal are shown in Fig. 2.4.1. The spectra were taken along the 6-mm path length of the crystal. The spectra are characterized by three broad absorption bands spanning the near ultraviolet to near infrared spectral regions. The absorption spectra depend strongly on the polarization of the incident radiation with respect to the crystallographic axes of the host. In particular, the peak position of the strongest band in the red-green spectral region shifts considerably with the polarization. Smaller shift has been observed in the near infrared region as well. The polarization dependence of the absorption spectra may be explained in terms of lower site symmetry of the Cr^{4+} ions invoking the polarization selection rules.[9]

Optical properties of chromium-doped forsterite have been studied for various reasons in the past.[14,15] Polarized absorption spectra of $Cr:Mg_2SiO_4$ grown by Czochralski method, reported in these papers exhibit features that are most unusual for octahedral Cr^{3+}. Rager and Weiser[15] tried to explain the spectra by describing the local symmetry of the mirror (M2) site by the orthorhombic point group D_2. This model does not predict the absorption band in the 1-μm region, which these authors failed to observe. One possible explanation for the 1-μm band was the existence of other impurity, such as Fe^{3+}, which is a commonly occurring impurity in olivines,

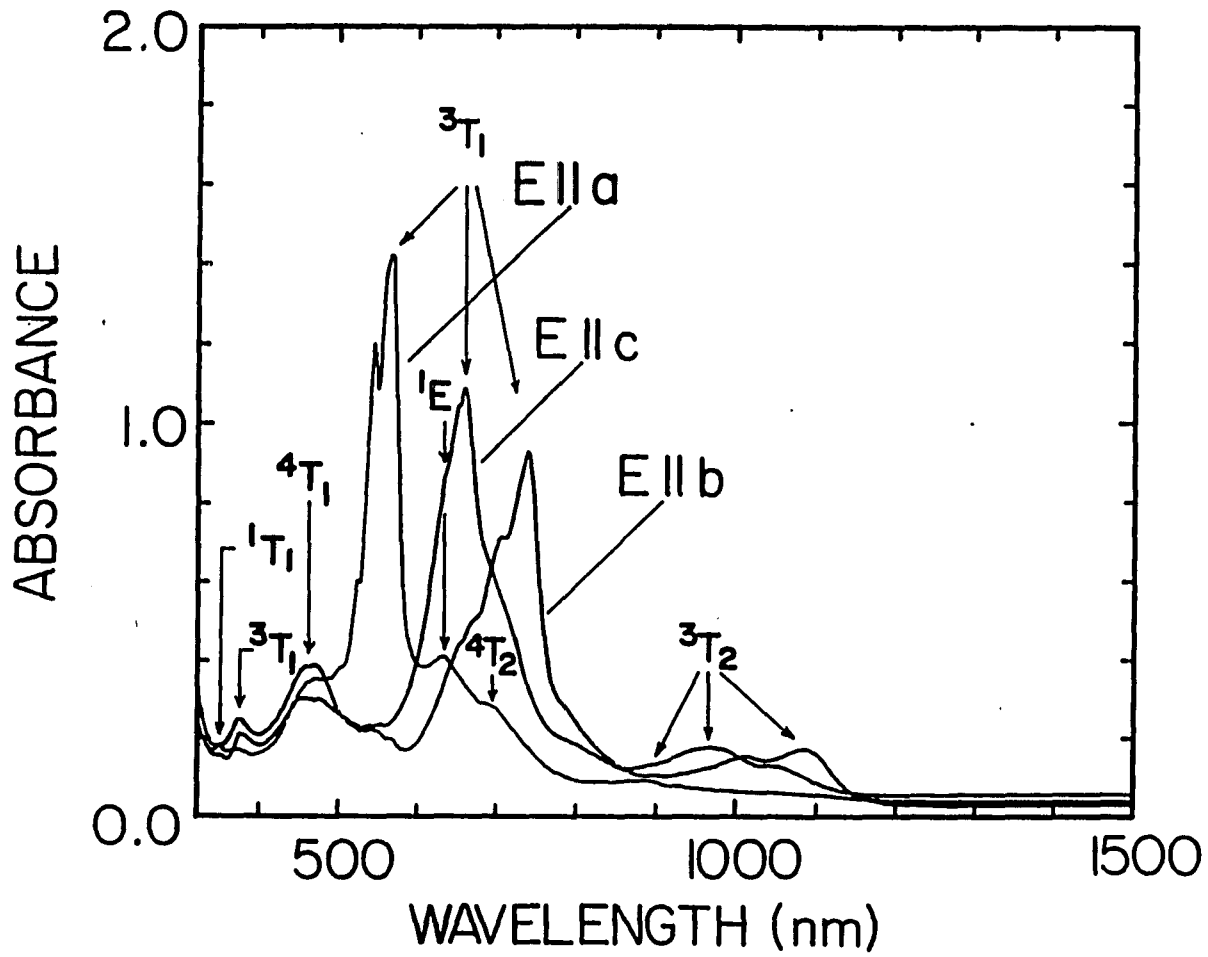

Fig. 2.4.1 Room temperature absorption spectrum of Cr:Mg_2SiO_4 grown under standard conditions (sample 2) for all three crystal orientations and 6-mm path length. Absorbance A or optical density OD is defined as $A=\log_{10}(I/I_o)$, where I_o is light intensity incident on the sample and I is the intensity of the transmitted radiation.

and exhibits similar absorption band in the near infrared. However, chemical analysis, as well as electron-spin resonance spectra of samples used in this study did not indicate sufficient iron content to account for the observed absorption.

A similar 850 - 1200 nm absorption band observed[20-23] in Nd,Cr:GSGG was first assumed[21] to be due to Cr^{2+}, and has finally been attributed to tetrahedral Cr^{4+} centers.[22,23] Almost identical band was observed in other garnets as well. In one of them, chromium-doped YAG, tunable laser operation was demonstrated[13] in the 1350 - 1450 nm region when pumped by 1064-nm Nd:YAG laser radiation. In view of the similarities between the near-infrared absorption band in chromium-doped garnet crystals and chromium-doped forsterite, the center responsible for this band was tentatively identified as a tetrahedrally coordinated tetravalent chromium (Cr^{4+}).

The observed absorption spectra of sample 2 shown in Fig. 2.4.1 deviate significantly from what would be normally expected from octahedral Cr^{3+} in the visible and near ultra-violet spectral region as well. In particular, the structures observed in 350 - 400 nm and 500 - 600 nm regions cannot be attributed to C^{3+} ion. The tremendous shift of the yellow-red absorption band for different polarization cannot be explained as a Cr^{3+} feature either.

Similar absorption spectra were observed for tetrahedrally coordinated trivalent vanadium[24] (V^{3+}) which is isoelectronic with Cr^{4+}, and octahedrally coordinated divalent nickel[25] (Ni^{2+}) whose energy level structure is also expected to be similar.

The hypothesis that there are both Cr^{3+} and Cr^{4+} centers in chromium-doped forsterite is further supported by spectroscopic measurements in chromium-doped

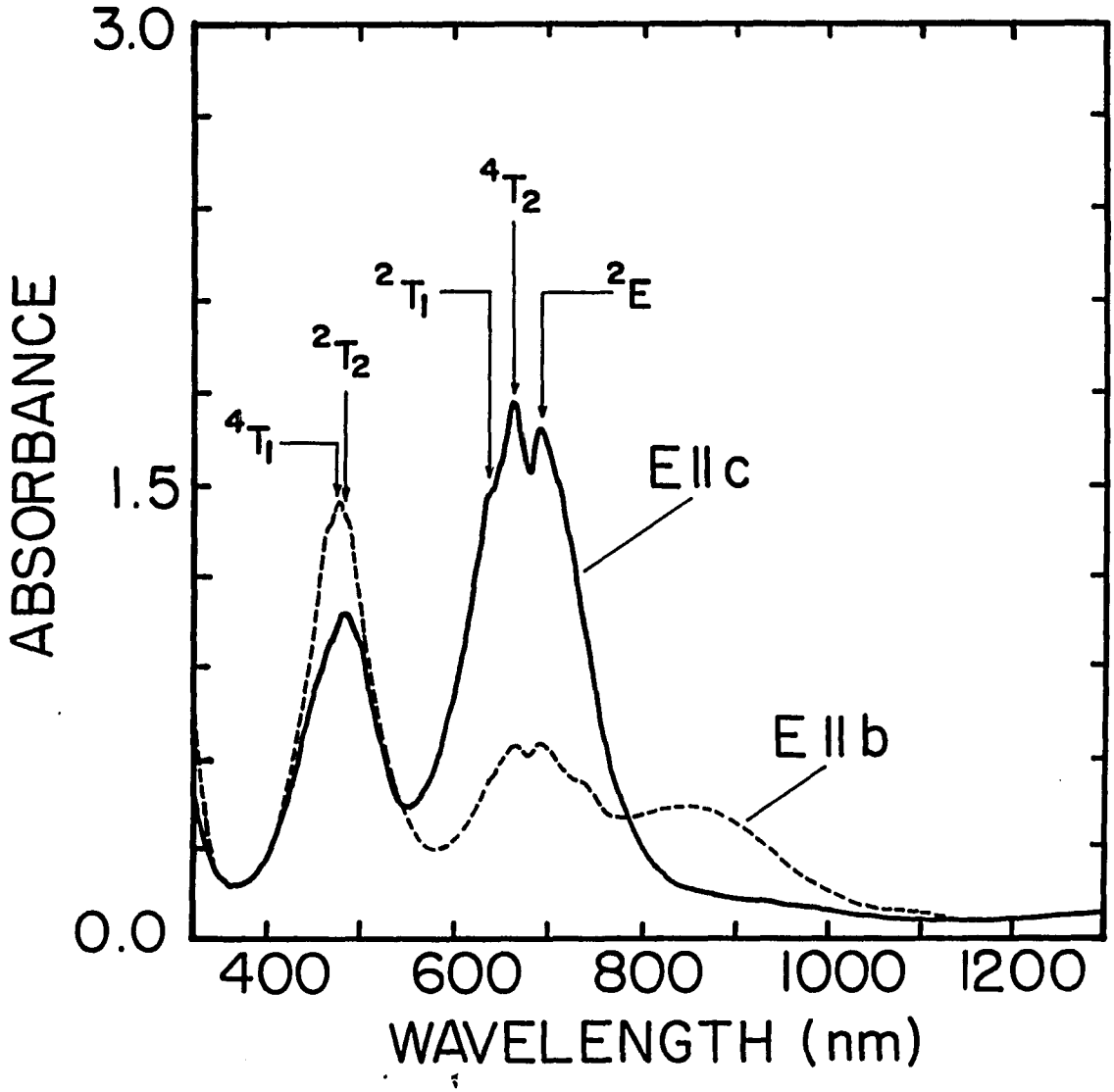

Fig. 2.4.2 Room temperature absorption spectrum of Cr:Mg_2SiO_4 grown in a reducing atmosphere (sample 3) for two different crystal orientations and 6-mm path length. Broad band with maximum at 850 nm is due to Cr^{2+}.

forsterite grown under different conditions. To distinguish between the contributions from Cr^{3+} and Cr^{4+} ions to the absorption spectra, we have complemented the absorption spectrum in Fig. 2.4.1 by the spectrum of sample 3, shown in Fig. 2.4.2. Sample 3 was grown in a reducing atmosphere and contains mostly Cr^{3+} ions as compared to samples 1 and 2 which have both the Cr^{3+} and Cr^{4+} centers. The absorption spectra of chromium-doped forsterite grown in a reducing atmosphere shown in Fig. 2.4.2 are very similar to the spectra of chromium-doped $LiSrAlF_6$ and other laser crystals[26] where the lasing ion is without any doubt octahedral Cr^{3+}. The near-infrared absorption band around 1 μm is almost completely missing, which implies that the 1-μm band is due to transitions within the states of Cr^{4+} ion. Also, the features in the visible and UV spectral regions that could not be attributed to Cr^{3+}, that were found in samples 1 and 2, were not observed. For one polarization only, ($E \| a$), very diminished 570-nm absorption band was observed, indicating that there are still some Cr^{4+} ions present in this crystal. These spectra show another interesting feature: two broad absorption bands centered at 850 nm and ~2 μm. Identical bands were observed in diffuse reflectance spectra of divalent chromium-doped forsterite.[27,28] It has been indicated[28] that Cr^{2+} can substitute for Mg^{2+} in a distorted M1 site in olivines and be stable. Therefore, it is quite natural to attribute these new bands to octahedrally coordinated divalent chromium, especially having in mind that reducing atmosphere should promote some of trivalent chromium into less oxidized divalent state.

2.4.2 Analysis of Absorption Spectra Using Tanabe-Sugano Formalism

Based on what was presented in section 2.4.1, the following conclusions can be made: (1) The spectra of chromium-doped forsterite grown in oxidizing atmosphere (samples 1 and 2) consist of two overlapping spectra corresponding to Cr^{3+} and Cr^{4+}

ions, and (2) The spectra of chromium-doped forsterite grown in a reducing atmosphere (sample 3) show mostly features of octahedral Cr^{3+}. In the near infrared spectral region it is relatively easy to make difference since no absorption is expected for Cr^{3+} ion. However, for the visible and the near ultraviolet absorption the contributions from the two valence states cannot be distinguished so easily. The absorption spectra due to Cr^{3+} and Cr^{4+} ions overlap in these spectral regions. To separate contributions of the two ions, we have analyzed both the spectra in terms of Tanabe-Sugano formalism.[29]

When a transition-metal ion, such as Cr^{3+} or Cr^{4+} is incorporated in a host crystal during the crystal-growing process its free-ion energy levels split due to the electric field (crystal field) produced by surrounding (so-called ligand) ions. The effect of ligand ions on the impurity ion depends on the number of ligand ions around the impurity ion and the symmetry of the site occupied by the ion. Energy levels of transition-metal ions are particularly strongly affected by the crystal field. Tanabe and Sugano[29] have developed a series of diagrams for $3d^N$ ions in a octahedral coordination showing energy levels of an ion as a function of crystal field parameter Dq and Racah parameters B and C. Tanabe-Sugano diagrams can be used for tetrahedrally coordinated ions as well. A general rule[30]

$$d^n(tetr)=d^{10-n}(oct),$$

where the symbol $d^n(tetr)$ represents the energy level order for a d^n system in a tetrahedral field and $d^{10-n}(oct)$ represents the energy level order for a d^{10-n} system in an octahedral field, allows us to use the Tanabe-Sugano diagram for $3d^8$ system in an octahedral environment (e.g. Ni^{2+}) to predict the behavior of Cr^{4+}, which is $3d^2$ system, in a tetrahedral environment.

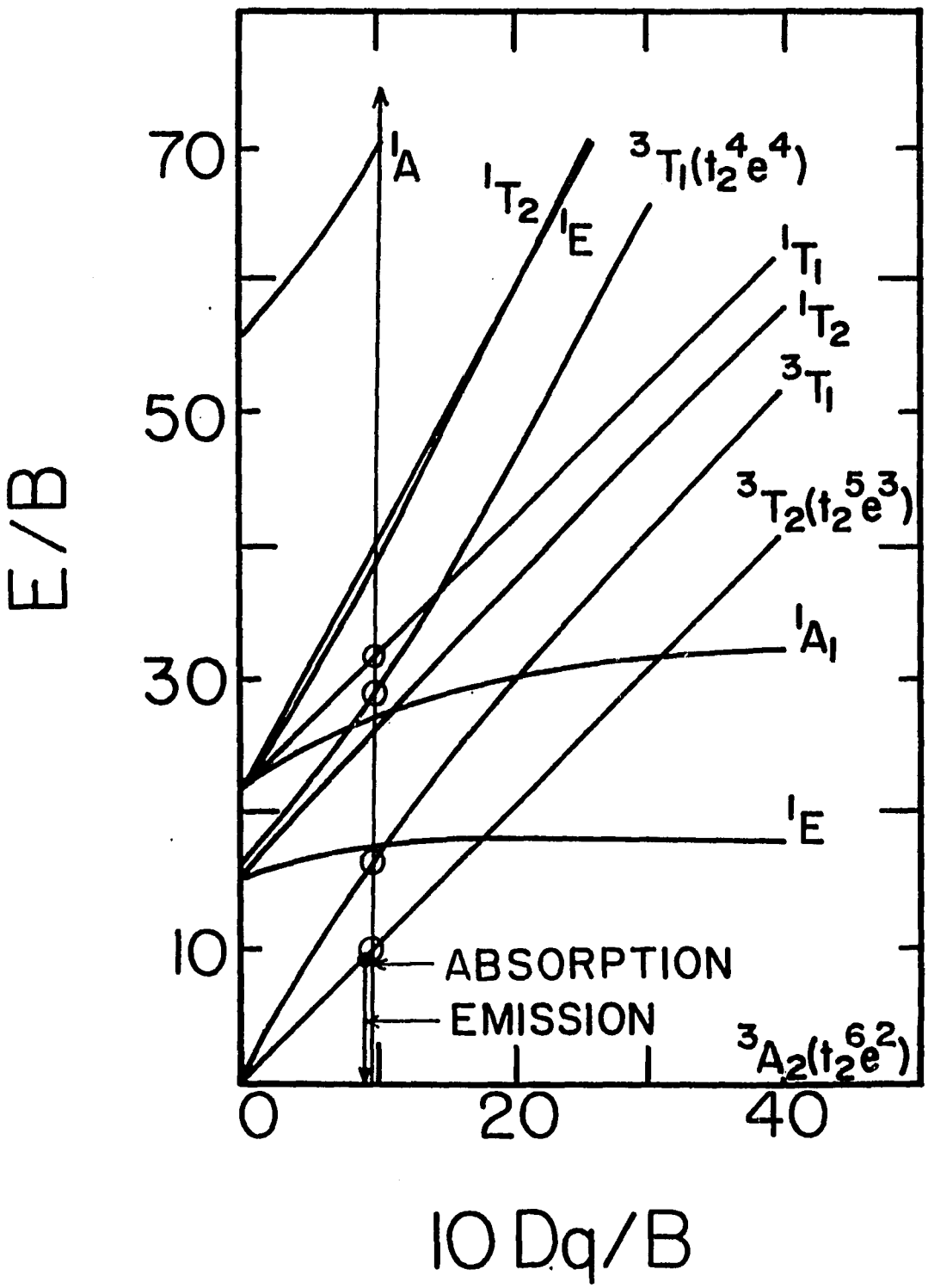

Fig. 2.4.3 Tanabe-Sugano diagram for Cr^{4+} in tetrahedral coordination. The values Dq=915 cm^{-1} and B=970 cm^{-1} were used to assign transitions shown in Fig. 2.4.1 and listed in Table 2.4.1.

TABLE 2.4.1: Energy Levels of Cr^{4+}:Mg_2SiO_4

	Energy (cm^{-1})	
Transition	Measured	Predicted
$^3A_2 \rightarrow {}^3T_2$	9,150	(9,150)
$^3A_2 \rightarrow {}^3T_1$	15,430	15,150
$^3A_2 \rightarrow {}^1E$	15,875	16,245
$^3A_2 \rightarrow {}^3T_1$	26,810	26,800
$^3A_2 \rightarrow {}^1T_1$	28,735	28,700
$^3T_2 \rightarrow {}^3A_2$	8,750	(8,750)

Predicted values are based on Tanabe-Sugano diagram for tetrahedral Cr^{4+} with parameters: B=970 cm^{-1}, C=3,980 cm^{-1}, and Dq=915 cm^{-1}. For bands whose position vary with the polarization of the incident light, average position (the centroid of three bands marked $^3T_1$ in Fig. 2.4.1) is taken for this analysis.

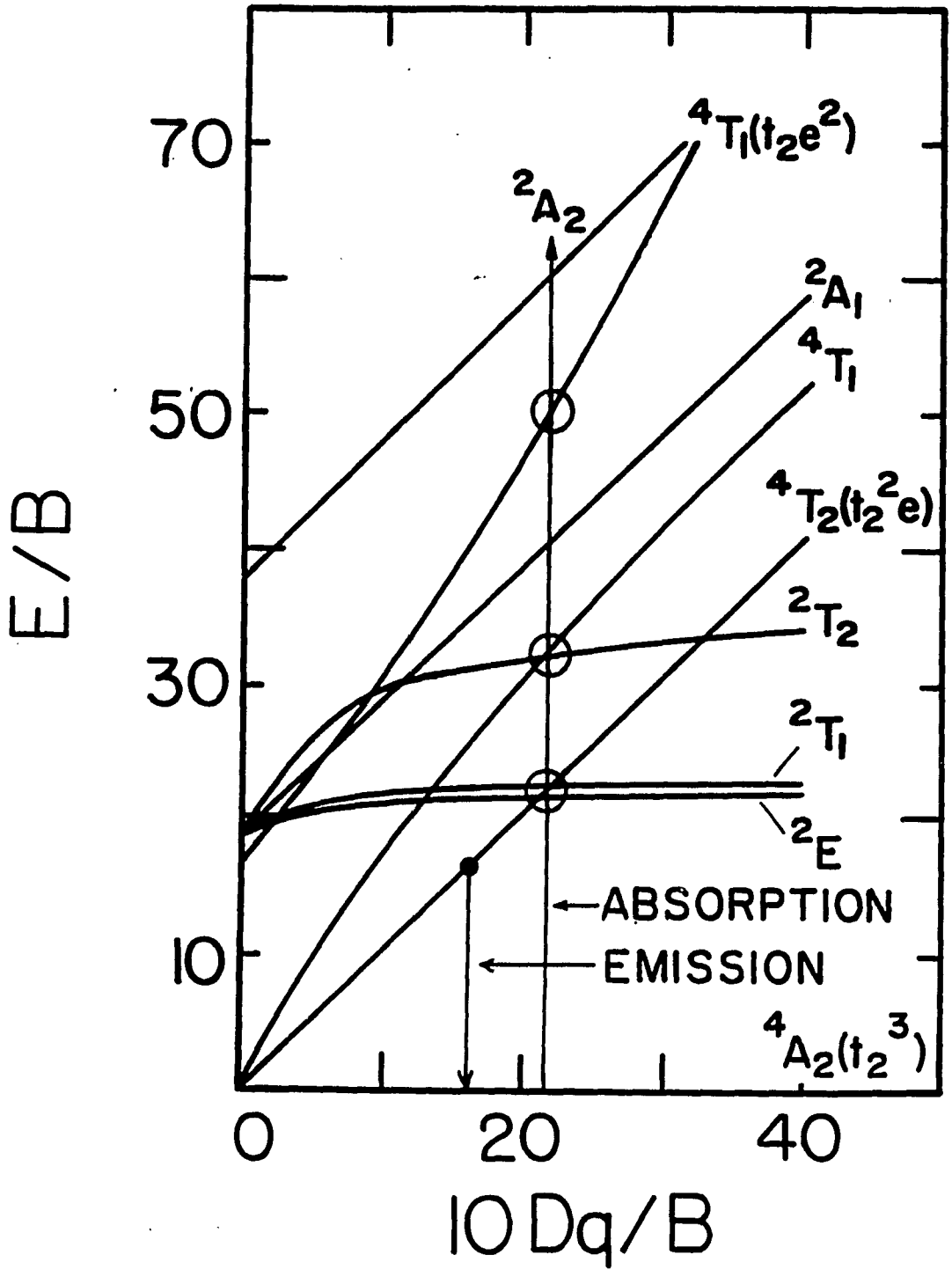

Fig. 2.4.4 Tanabe-Sugano diagram for Cr^{3+} in octahedral coordination. The values Dq=1510 cm^{-1} and B=695 cm^{-1} were used to assign transitions shown in Fig. 2.4.2 and listed in Table 2.4.2.

TABLE 2.4.2: Energy Levels of Cr^{3+}:Mg_2SiO_4

	Energy (cm^{-1})	
Transition	Measured	Predicted
$^4A_2 \rightarrow {}^4T_2$	15,100	(15,100)
$^4A_2 \rightarrow {}^2E$	14,450	14,600
$^4A_2 \rightarrow {}^2T_1$	15,380	15,300
$^4A_2 \rightarrow {}^2T_2$	21,050	21,300
$^4A_2 \rightarrow {}^4T_{1a}$	21,500	21,780
$^4A_2 \rightarrow {}^4T_{1b}$	33,780	33,940
$^4T_2 \rightarrow {}^4A_2$	11,100	(11,100)
$^2E \rightarrow {}^4A_2$	14,450	14,600

Predicted values are based on the Tanabe-Sugano diagram for octahedral Cr^{3+} with parameters: B=695 cm^{-1}, C=3,130 cm^{-1}, and Dq=1,510 cm^{-1}.

Tanabe-Sugano diagrams for octahedral $3d^3$ ion and tetrahedral $3d^2$ ion were used to explain all the features observed in the absorption spectra of chromium-doped forsterite grown under different conditions. In these considerations Cr^{3+} ion was assumed to be in octahedrally coordinated site and Cr^{4+} ion to be in tetrahedrally coordinated site.

Energy levels were calculated by diagonalizing the Tanabe-Sugano matrices[31] using Dq and B as fitting parameters and assuming that the ratio C/B does not change from the value for the free ion. Tanabe-Sugano matrices for tetrahedral $3d^2$ ions and octahedral $3d^3$ ions and the procedure for fitting the experimental data are given in the Appendix.

Comparison of the predicted values of tetrahedral Cr^{4+} and octahedral Cr^{3+} in forsterite with the measured values are presented in Tables 2.4.1 and 2.4.2, respectively. The values of crystal field parameter Dq and Raccah parameters B and C that were used to fit the positions of the absorption peaks are also listed. The transition assignments in Figs. 2.4.1 and 2.4.2 follow from this analysis. The corresponding Tanabe-Sugano diagrams, with transitions indicated, are presented in Figs. 2.4.3 and 2.4.4.

2.4.3 Fluorescence Spectra

Fluorescence spectra of three different samples for various crystal orientations measured at room temperature and liquid nitrogen temperature, presented in Figs. 2.4.5 - 2.4.7, show contributions from at least three optically active centers in chromium-doped forsterite. The fluorescence spectra of the Cr^{4+}-rich sample (sample 1), for three different crystal orientations, are shown in Figs. 2.4.5 and 2.4.6, and that of sample 2 (with lower Cr-ion concentration) for $E \| b$ in Fig. 2.4.7.

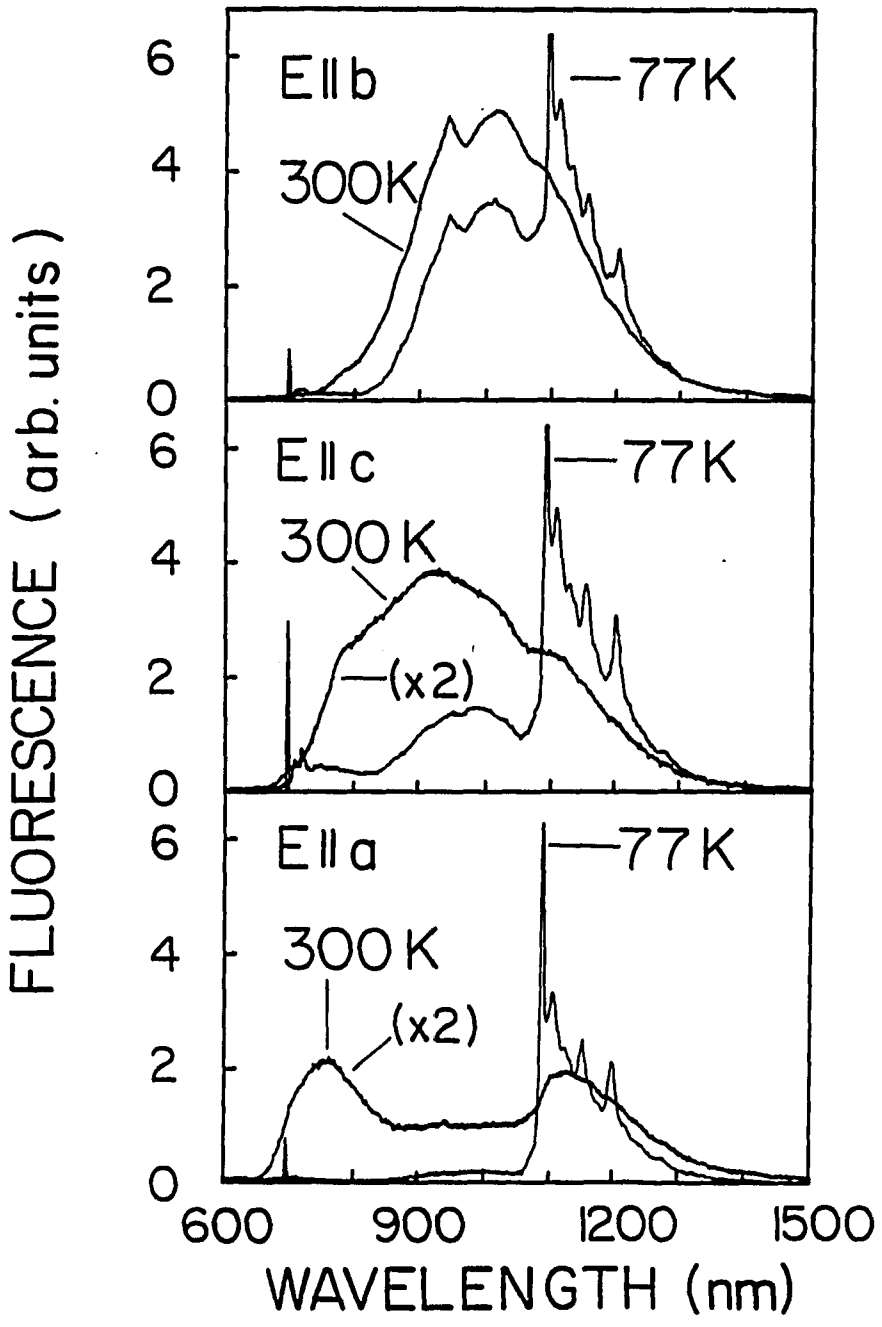

Fig. 2.4.5 Room temperature and liquid nitrogen temperature fluorescence spectra of Cr:Mg_2SiO_4 grown under standard conditions (Sample 1) for 488-nm excitation for three different crystal orientations. The spectra were recorded with a PbS detector.

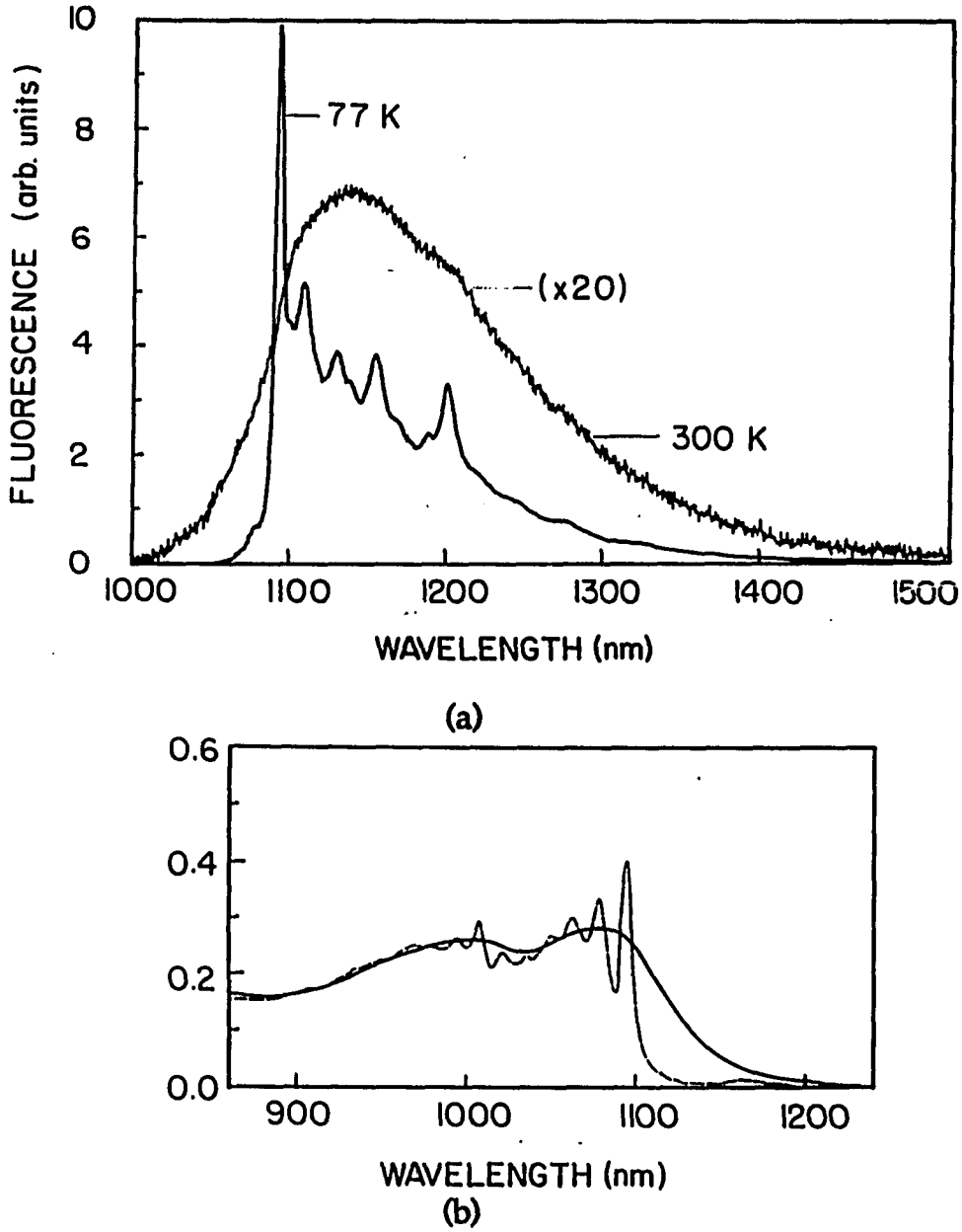

Fig. 2.4.6 Near infrared absorption and fluorescence spectra of Cr:Mg_2SiO_4 grown under standard conditions (sample 1): a) Absorption spectra at room temperature (solid line) and liquid nitrogen temperature (broken line) for E $\|$ *b* axis and propagation along *a* axis. b) Fluorescence spectra (fluorescence excited by 1064-nm radiation polarized along *b* axis) at room temperature and liquid nitrogen temperature.

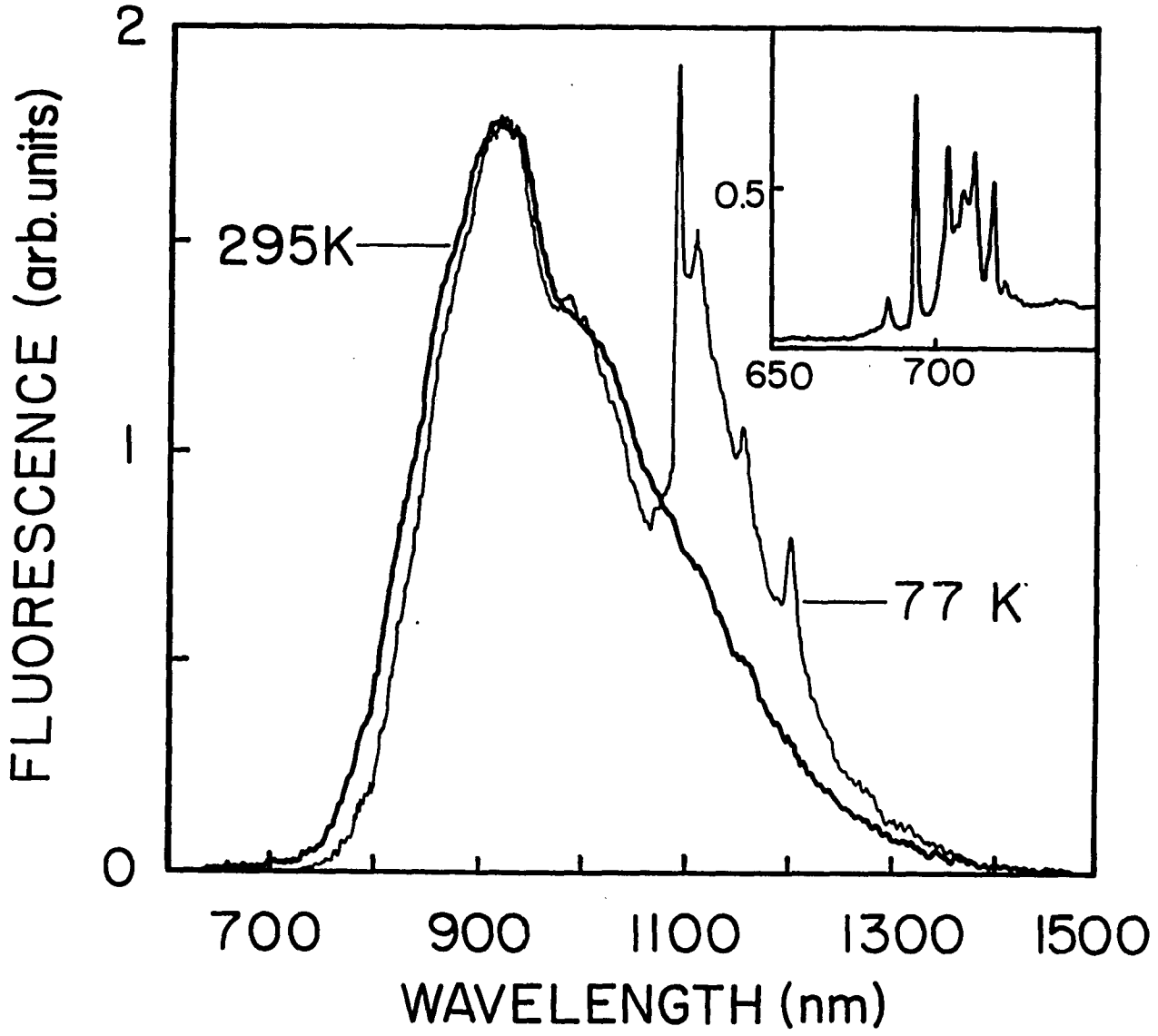

Fig. 2.4.7 Room temperature (thicker line) and liquid nitrogen temperature (thin line) fluorescence spectra of Cr:Mg_2SiO_4 grown under standard conditions (sample 2) for 488-nm excitation parallel to *b* axis. The spectra were taken with PbS detector which was not sensitive enough to detect the 693-nm zero-phonon line and its sideband shown in the inset. These features were resolved with a photomultiplier tube with S-20 response.

The room temperature spectrum measured with sample 1, excited by the 488-nm line of argon-ion laser, is a broad band spanning 680 - 1400 nm range. At liquid nitrogen temperature, the spectrum breaks up into three structured bands.

Most interesting feature, consisting of a strong and sharp line at 1096 nm followed by a vibrational sideband, was observed in the 1096 - 1400 nm range. These spectral features clearly indicate that the fluorescence in this region is closely related to the absorption band in the near infrared. The emission in this range is the Stokes-shifted counterpart of the near infrared absorption, and is attributed to $^3T_2 \rightarrow {}^3A_2$ transitions in Cr^{4+} ion. The sharp zero-phonon line at 1096 nm corresponds to purely electronic transition between the $^3T_2$ and $^3A_2$ states of the Cr^{4+} ion and appears as a prominent feature in both the absorption and emission spectra at low temperatures. Near infrared room-temperature and liquid-nitrogen-temperature absorption and fluorescence spectra (fluorescence excited by 1064-nm radiation from a cw Nd:YAG laser) of sample 1 for $E \| b$ axis are shown in Fig. 2.4.6. Similar structure in the 1100 - 1400 nm range was observed in the liquid nitrogen spectra of sample 2, displayed in Fig. 2.4.7.

Low temperature absorption and fluorescence spectra of sample 1, shown in Fig. 2.4.6 were the key results for identification of the unknown center and for future development of the forsterite laser. The zero-phonon line appeared in both the absorption and fluorescence spectra at 1096 nm and the structured sideband in the emission spectrum is a mirror image of the sideband in the absorption spectrum. This means that the absorption in the near infrared is not a "parasitic" absorption due to some undesirable impurity but is actually related to the fluorescence band and can be used as a pump band of the Cr:forsterite laser.

Some features displayed in Figs. 2.4.5, 2.4.6 and 2.4.7 are completely absent from the near infrared spectra of sample 3, shown in Fig. 2.4.8. In particular, the 1096-nm zero-phonon line and its sideband extending to 1400 nm were not observed in this sample which was grown in a reducing atmosphere. The absence of the structure that may be attributed to tetrahedrally coordinated Cr^{4+} ions in the spectrum of sample 3 can be explained by the effect of the growth atmosphere on changing of the valence state of the chromium ion. In a reducing atmosphere, it is highly unlikely to expect that any of the Cr^{3+} ions will be promoted into higher oxidation state. It is more realistic to expect some of the Cr^{3+} ions to be reduced, and that has indeed been confirmed by absorption spectra of sample 3, which show features which can be assigned to Cr^{2+} ion. The room temperature emission spectrum of sample 3 is slightly narrower than the corresponding spectrum of sample 2, extending only to 1300 nm, and shows contribution from Cr^{3+} ions predominantly.

A strong broad fluorescence band with a maximum at 900 nm, observed in all three samples, is attributed to $^4T_2 \rightarrow {}^4A_2$ vibronic transition of the Cr^{3+} ion in the mirror site. This band remains unchanged at liquid nitrogen temperature for all three samples. This emission is typical for Cr^{3+} ions in a low crystal field site lacking inversion, for which the ^2E state lies above the $^4T_2$ state. In this case, all radiative transitions originate from the bottom of the $^4T_2$ state, resulting in broad vibronic emission with relatively short fluorescence lifetimes in the μs range.

A sharp line is observed at 693 nm at liquid nitrogen temperature in all the samples. However, this line and its sideband, easily detected with PbS detector for sample 1, could not be observed in samples 2 and 3. For these two samples these features were recorded with a photomultiplier tube with S-20 photocathode and are shown as insets in Figs. 2.4.7 and 2.4.8. The 693-nm line, followed by a structured

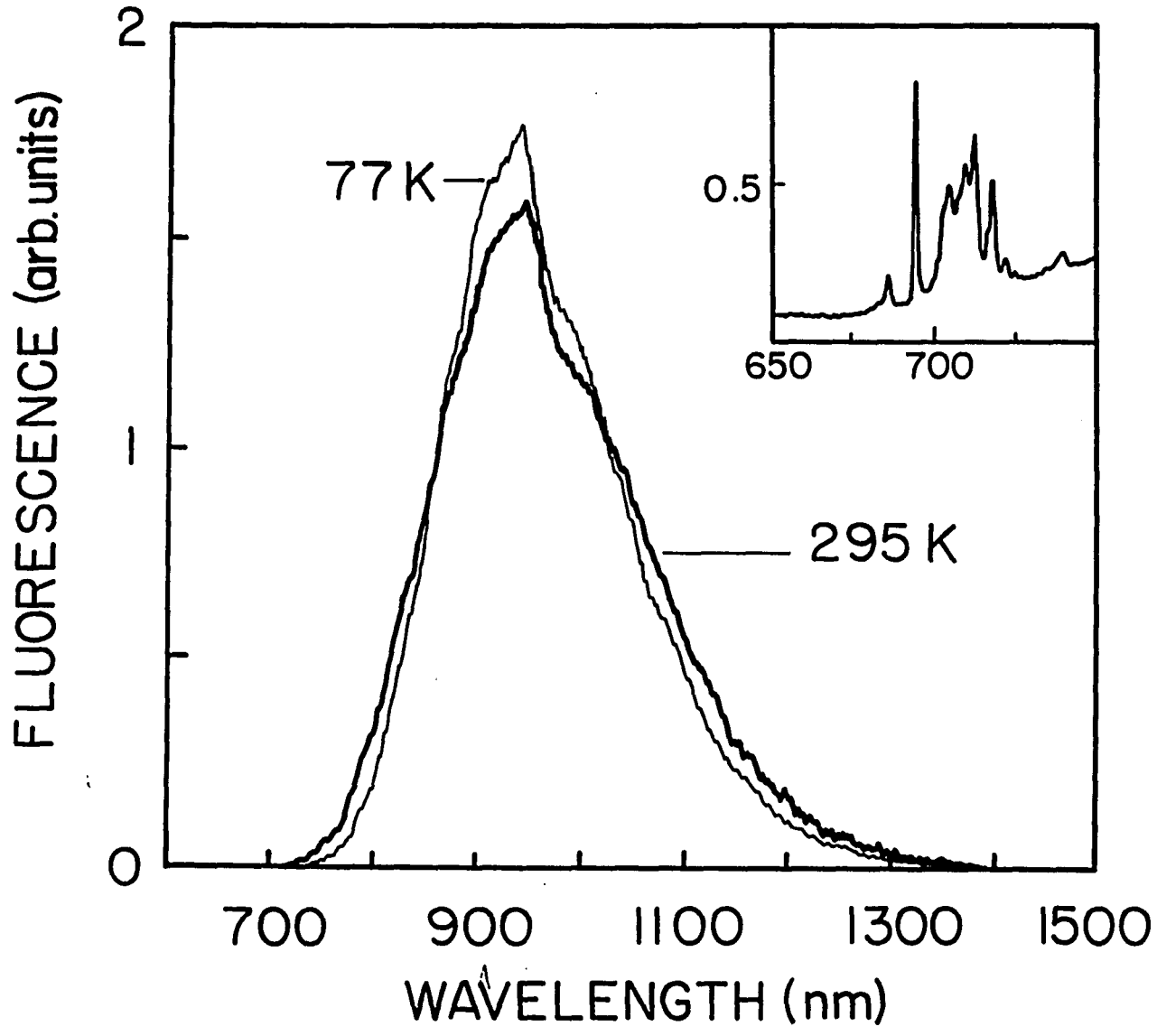

Fig. 2.4.8 Room temperature (thicker line) and liquid nitrogen temperature (thin line) fluorescence spectrum of Cr:Mg_2SiO_4 grown in a reducing atmosphere (sample 3) for 488-nm excitation and E || *b* axis. The spectra were taken with PbS detector which was not sensitive enough to detect the 693-nm zero-phonon line and its sideband shown in the inset. These features were resolved with a photomultiplier tube with S-20 response.

sideband that extends to 750 nm is attributed to $^2E \rightarrow {}^4A_2$ transition (R-line) in Cr^{3+} ions in the intermediate-field sites with inversion symmetry. The lowest-lying excited state of the Cr^{3+} ion in this case is the ^2E state. At low temperatures, most of the radiation is emitted via $^2E \rightarrow {}^4A_2$ transition. The $^2E \rightarrow {}^4A_2$ transition is both spin- and parity-forbidden and gives rise to sharp-line emission with fluorescence lifetime in the ms range.

The conclusions about the various active centers in chromium-doped forsterite, based on fluorescence measurements, are supported by the results of the fluorescence lifetime measurements, as will be shown in the next section.

The emission transitions for both Cr^{4+} and Cr^{3+} ions are also indicated in the Tanabe-Sugano diagrams (Figs. 2.4.3 and 2.4.4, respectively).

2.4.4 Fluorescence Lifetime

The fluorescence lifetime has been measured as a function of wavelength both at room and liquid nitrogen temperatures. Several different lifetimes were measured, indicating existence of several inequivalent optically active centers. Fluorescence decays at different wavelengths and for different excitations at room temperature and at liquid nitrogen temperature are presented in Figs. 2.4.9-2.4.13. The results of fluorescence lifetime measurements are summarized in Table 2.4.3.

The broad band fluorescence in the 800 - 1200 nm wavelength range is characterized by 13-μs lifetime for all three samples. Fluorescence decay of $Cr:Mg_2SiO_4$ (sample 2), showing single-exponential time dependence, measured at 900 nm for 532-nm excitation is presented in Fig. 2.4.9. Identical decay times were observed for samples 1 and 3 in the same wavelength region. The 13-μs fluorescence lifetime did not change significantly at liquid nitrogen temperature, and is attributed

TABLE 2.4.3: Fluorescence Lifetime as a Function of Temperature and Wavelength

Wavelength (nm)	Sample Temperature: Room Temperature (295 K)	Sample Temperature: Liquid Nitrogen Temperature (77 K)	Sample #
683*	-	5.4 ms	1,2,3
693*	330 μs	0.9 ms	1,2,3
700-800*	330 μs	0.9 ms	1,2,3
750-1150*	13 μs	13 μs	1,2,3
1100-1400†	2.7 μs	25 μs	1,2

*Excitation wavelength: 532 nm

†Excitation wavelength: 1064 nm

Lifetimes measured in the 700-1150 nm wavelength range using 532-nm excitation were the same for all three samples . 1064-nm excitation was used for samples 1 and 2 only, since sample 3 does not have absorption in the infrared region.

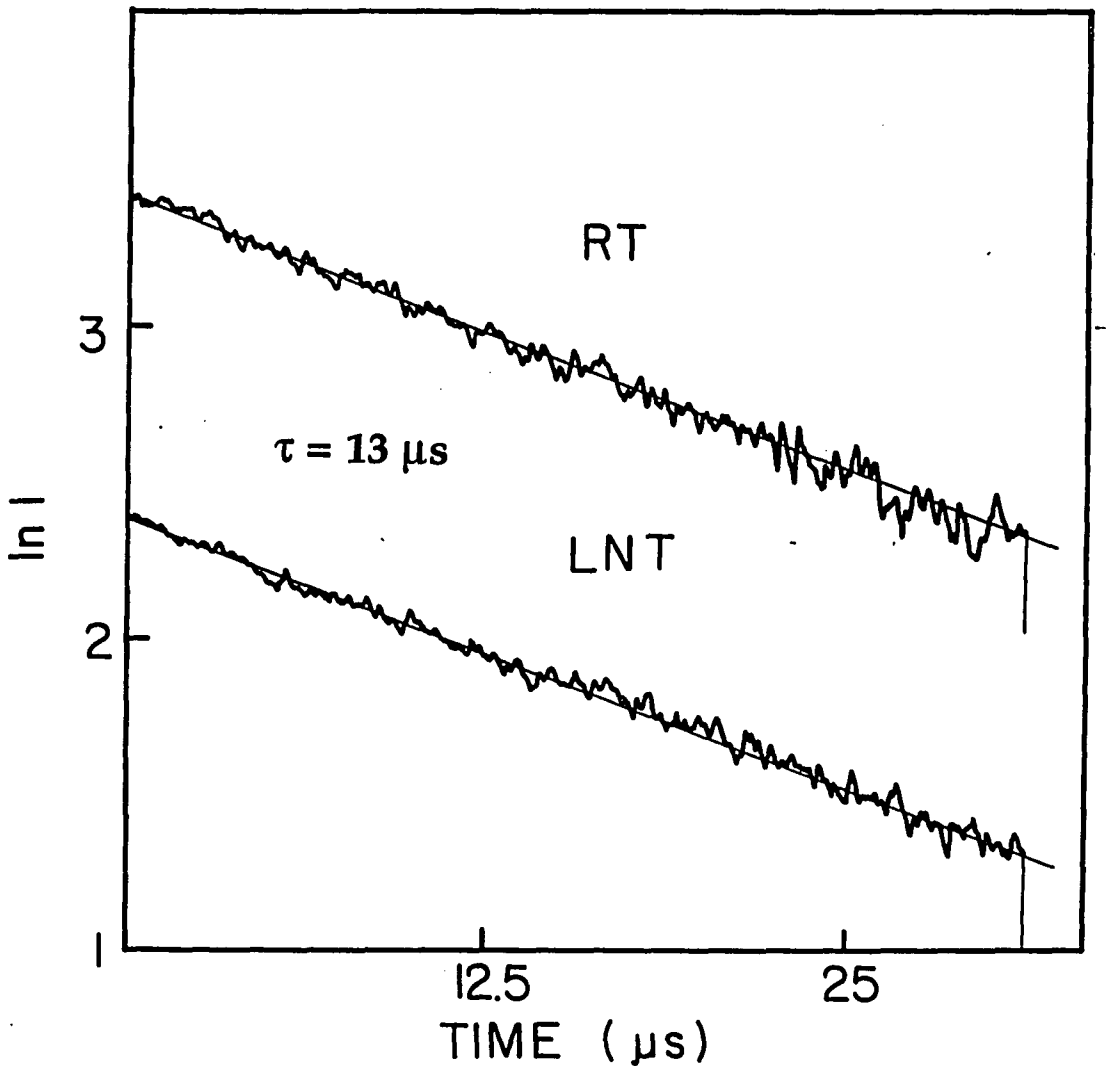

Fig. 2.4.9 Fluorescence decay of Cr:Mg_2SiO_4 for 532-nm excitation at 900 nm at room temperature (RT) and liquid nitrogen temperature (LNT); no change in fluorescence lifetime between two temperatures has been observed. Identical decay times were observed for samples 2 and 3; decay curves for sample 2 are shown.

to the $^4T_2 \rightarrow {}^4A_2$ vibronic emission of the low-field Cr^{3+} centers with mirror symmetry (C_s). The relatively short lifetime can be explained as follows.

For both $3d^2$ and $3d^3$ ions all optical transitions occur within the states of the same configuration. Therefore, all electric dipole transitions are parity forbidden. The electric dipole transitions that are observed are a consequence of the effect of dynamic and static odd-parity fields of the crystal on the ion. In chromium-doped forsterite, Cr^{3+} ions occupy two types of sites: one with mirror and one with inversion symmetry. The mirror site provides odd-parity field necessary to relax the parity selection rule, making electric dipole transitions possible. The relatively short 13-μs lifetime is therefore attributed to the mirror site Cr^{3+} ions. This lifetime is comparable to the estimated intrinsic lifetime of 7.1 μs of the $^4T_2$ state of the mirror site Cr^{3+} in alexandrite.[32]

In the 700 - 800 nm region, at room temperature, another component with a lifetime of ~350 μs was measured for all three samples, for 532-nm excitation. The fluorescence decay curve of sample 2 measured at 750 nm is shown in Fig. 2.4.10 (a). The decay exhibits a two-component time dependence. The fast component has lifetime of 13 μs and it corresponds to the high-energy tail of the $^4T_2 \rightarrow {}^4A_2$ transition of the low-field mirror site Cr^{3+} ion. The slower 350-μs lifetime is typical for intermediate-field Cr^{3+} ions in the site with inversion symmetry (C_i), where there is a competition between the emission from higher-lying level ($^4T_2$) with shorter intrinsic decay time, and lower-lying level (^2E) with longer intrinsic lifetime. The fluorescence decay measured with a streak camera at 700 nm is shown on a longer time scale in Fig. 2.4.10 (b). The 350-μs lifetime corresponds to the room-temperature emission. At liquid nitrogen temperature, the lifetime increases to 0.9 ms.

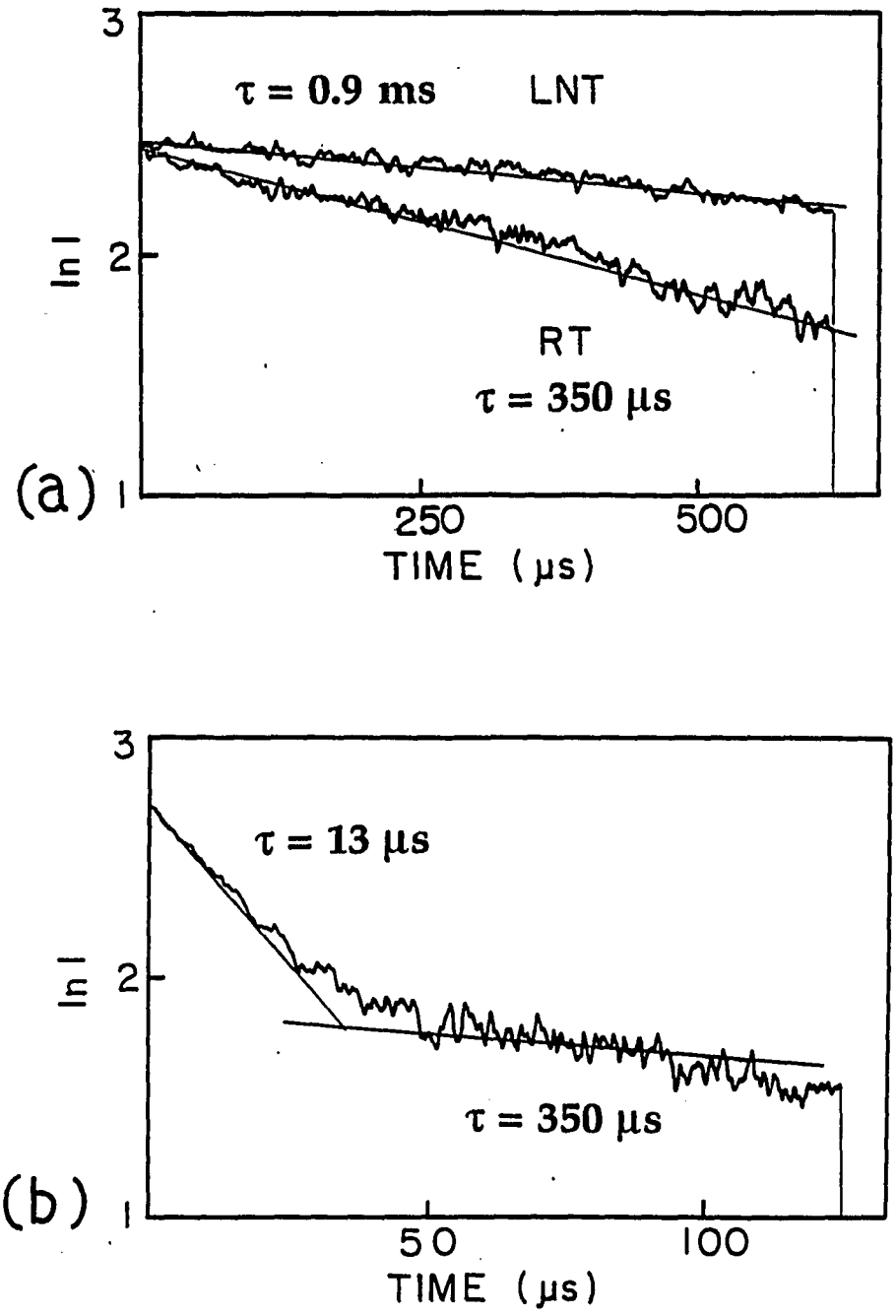

Fig. 2.4.10 Fluorescence decay of Cr:Mg_2SiO_4 for 532-nm excitation: (a) At 693 nm, room temperature (RT) and liquid nitrogen temperature (LNT); (b) At 750 nm, room temperature; note two component decay. Identical decay times were observed for samples 2 and 3; decay curves for sample 2 are shown.

As shown in previous section in Figs. 2.4.5 and 2.4.7, at liquid nitrogen temperature, fine spectral structure has been observed in the same spectral range, around 700 nm, on the high energy side of the broadband emission. The sharp lines are assigned to the $^2E \rightarrow {}^4A_2$ emission (R-lines) from Cr^{3+} ions at the inversion site. Two different lifetimes of the structures were measured using highly sensitive S-20 photomultiplier tube and oscilloscope. These lifetimes were measured to be much longer than the lifetime of the broadband fluorescence, which did not change significantly from its room temperature value of 13 μs. Fluorescence decays of $Cr:Mg_2SiO_4$ (sample 1) for 532-nm excitation at liquid nitrogen temperature, at 693 nm and 683 nm, recorded with S-20 photomultiplier tube are shown in Figs. 2.4.11 (a) and (b), respectively. Two lifetimes were observed: 0.9-ms component corresponding to the sharp line at 693 nm and its sideband (same result as in the streak camera measurements) and 5.4-ms component corresponding to the small sharp peak at 683 nm that could not be detected with a streak camera. These two lifetimes represent the intrinsic lifetimes of the ^2E state of the two inequivalent intermediate-field inversion site Cr^{3+} centers. Two different lifetimes of 0.9 ms and 5.4 ms from two inequivalent inversion site Cr^{3+} centers most likely arise from different possible mechanisms of charge compensation.

Room temperature fluorescence decay measured at 1150 nm for 532-nm and 1064-nm excitations is shown in Fig. 2.4.12. First decay curve, measured in sample 2 for 532-nm excitation, shown in Fig. 2.4.12 (a), exhibits a two-component time dependence. Identical behavior was observed in sample 1. The slower component of 13 μs corresponds to the low energy tail of the $^4T_2 \rightarrow {}^4A_2$ transition of the low-field mirror site Cr^{3+} ion. The 2.7-μs component was attributed to tetrahedrally coordinated Cr^{4+}. The decay curve presented in Fig. 2.4.12 (a) indicates that the 532-nm radiation simultaneously excites Cr^{3+} and Cr^{4+} ions which then decay with

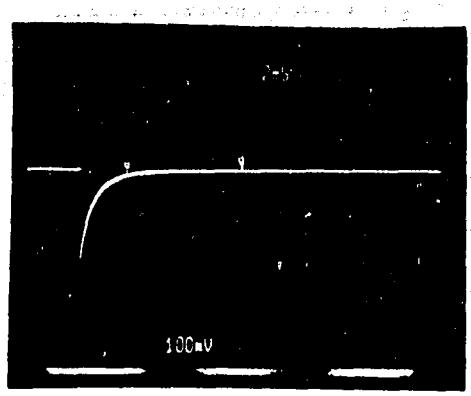

(a)

(b)

Figure 2.4.11 Fluorescence decay of Cr:Mg_2SiO_4 (sample 1) at liquid nitrogen temperature recorded with S-20 photomultiplier tube: (a) Decay corresponding to the main peak at 693 nm; (b) Decay corresponding to the smaller peak at 683 nm. Excitation wavelength is 532 nm in both cases. Time scale: 2 ms/division. Identical decay times were observed for samples 2 and 3.

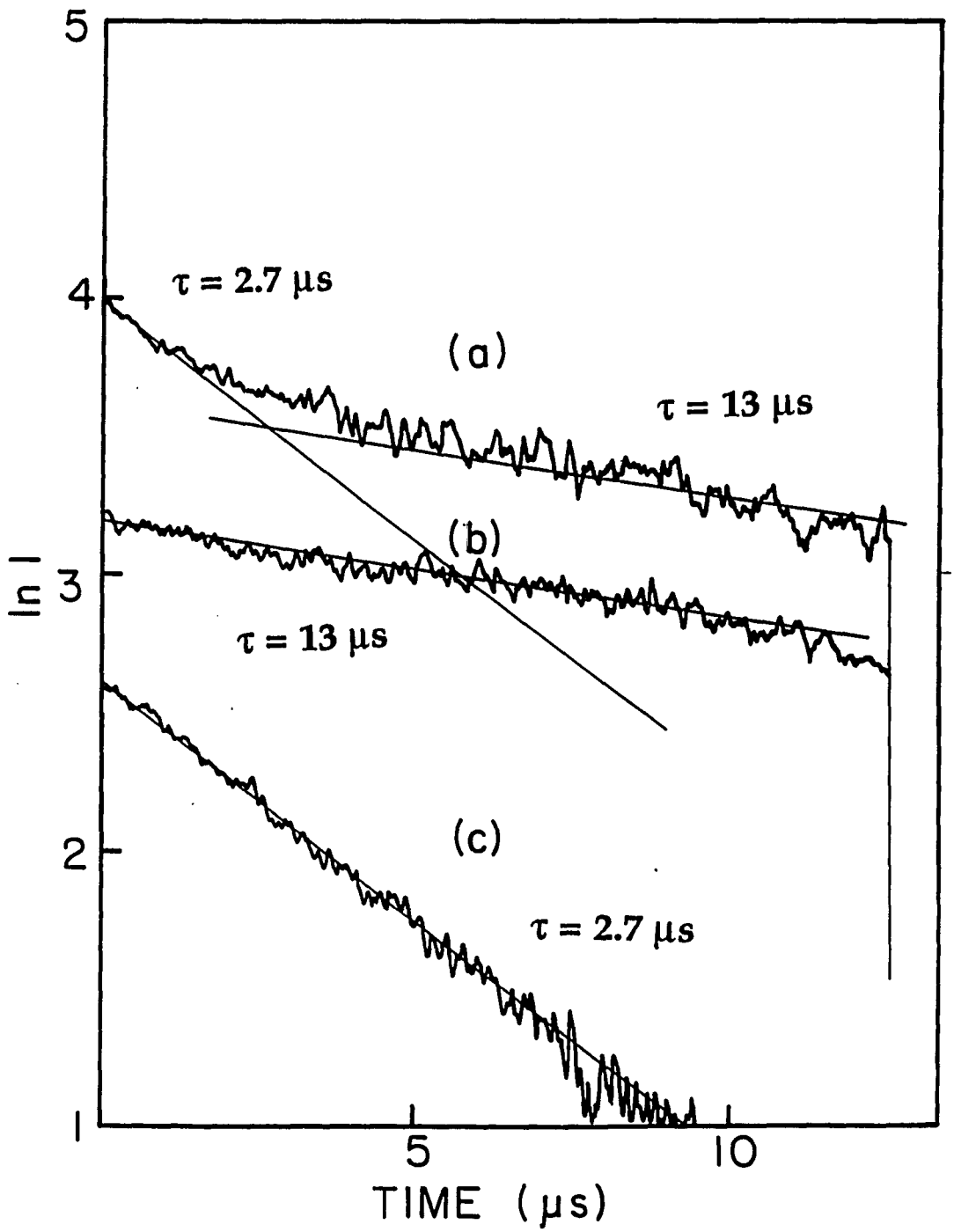

Fig. 2.4.12 Room temperature fluorescence decay of Cr:Mg_2SiO_4 measured at 1150 nm: (a) Sample 2, 532-nm excitation; note two component decay; (b) Sample 3, 532-nm excitation; (c) Sample 2, 1064-nm excitation.

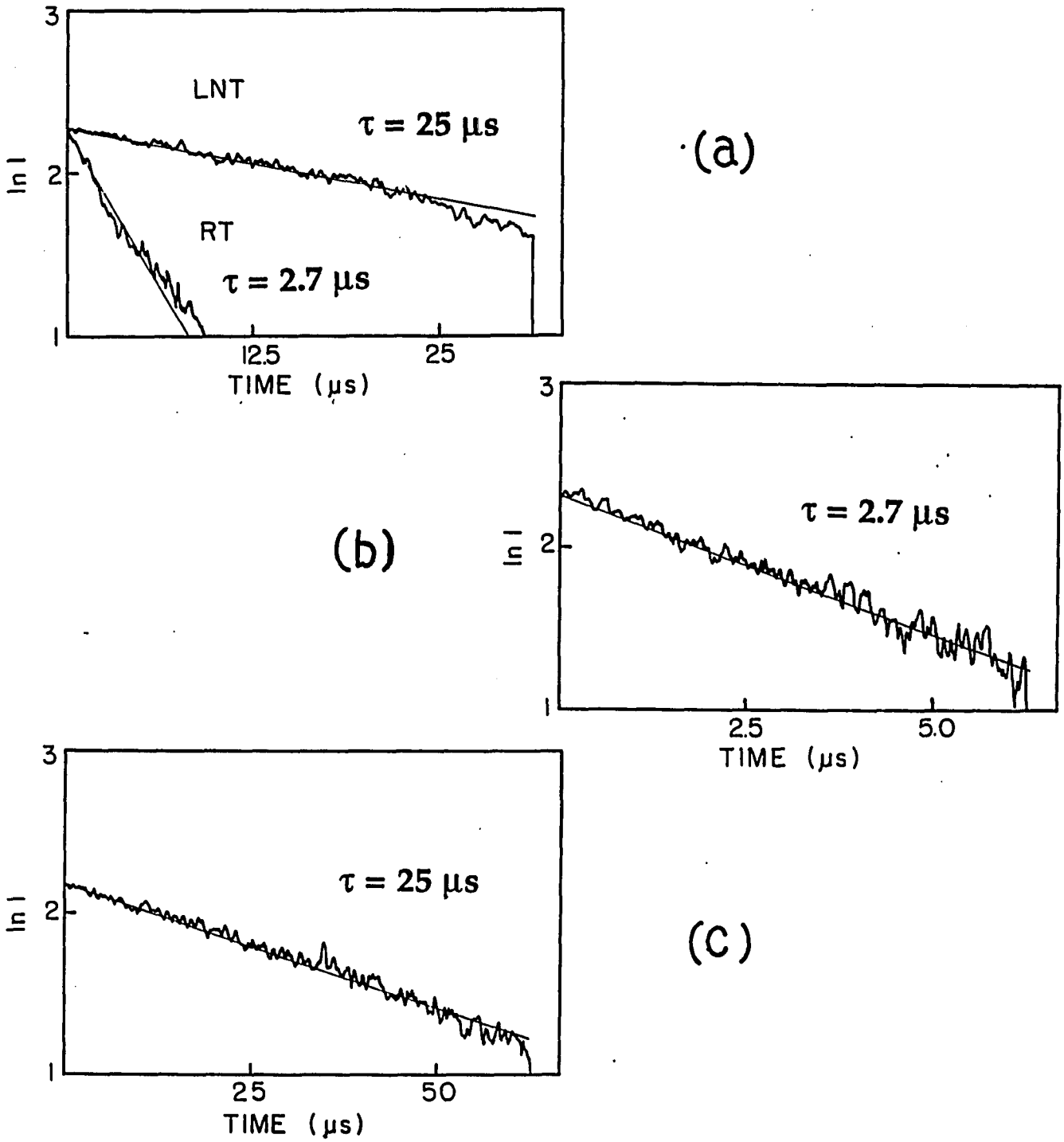

Fig. 2.4.13 Fluorescence decay of Cr:Mg_2SiO_4 at 1150 nm for 1064-nm excitation: (a) At room temperature (RT) and liquid nitrogen temperature (LNT); (b) At room temperature, expanded scale; (c) At liquid nitrogen temperature, compressed scale. Identical decay times were observed for samples 1 and 2; decay curves for sample 1 are shown.

different lifetimes. To prove this claim, we have measured the fluorescence lifetime of Cr:Mg_2SiO_4 grown in a reducing atmosphere (sample 3) at 1150 nm, for 532-nm excitation. Since this sample does not contain much Cr^{4+} we did not expect to observe the fast 2.7 μs component attributed to Cr^{4+} ion. This was indeed the case, as shown in Fig. 2.4.12 (b). In sample 3, only the 13-μs component corresponding to the mirror-site Cr^{3+} was observed. Finally, to selectively excite only Cr^{4+} ions, sample 2 was pumped by 1064-nm radiation. The single-exponential fluorescence decay characterized by 2.7 μs lifetime corresponding to the tetrahedrally coordinated Cr^{4+} ion was observed and is shown in Fig. 2.4.12 (c). Identical result was obtained for sample 1, as well.

At liquid nitrogen temperature, fluorescence lifetime of 25 μs was observed in samples 1 and 2, in the 1100 - 1400 nm range, for 1064-nm excitation. Fluorescence decays measured in sample 1, at 1150 nm, for 1064-nm excitation at room temperature and at liquid nitrogen temperature are shown in Fig. 2.4.13. Identical results were obtained in sample 2.

A lifetime of 2.7 μs at room temperature, and 25 μs at liquid nitrogen temperature, measured in samples 1 and 2, in the 1100-1400 nm range, is attributed to $^3T_2 \rightarrow {}^3A_2$ radiative transition of Cr^{4+} ion. The tetrahedral site where Cr^{4+} substitutes for Si^{4+} also lacks inversion symmetry and provides odd-symmetry field which makes electric dipole transitions possible. This explains lifetimes in the μs range and high transition strengths observed in the spectra.

A temperature dependence of the fluorescence lifetime, as well as temperature dependence of the relative quantum efficiency of the $^3T_2 \rightarrow {}^3A_2$ transition in Cr^{4+} ion were measured in the 77-320 K temperature range. These measurements were performed on sample 1 only. Identical results may be expected from sample 2, since

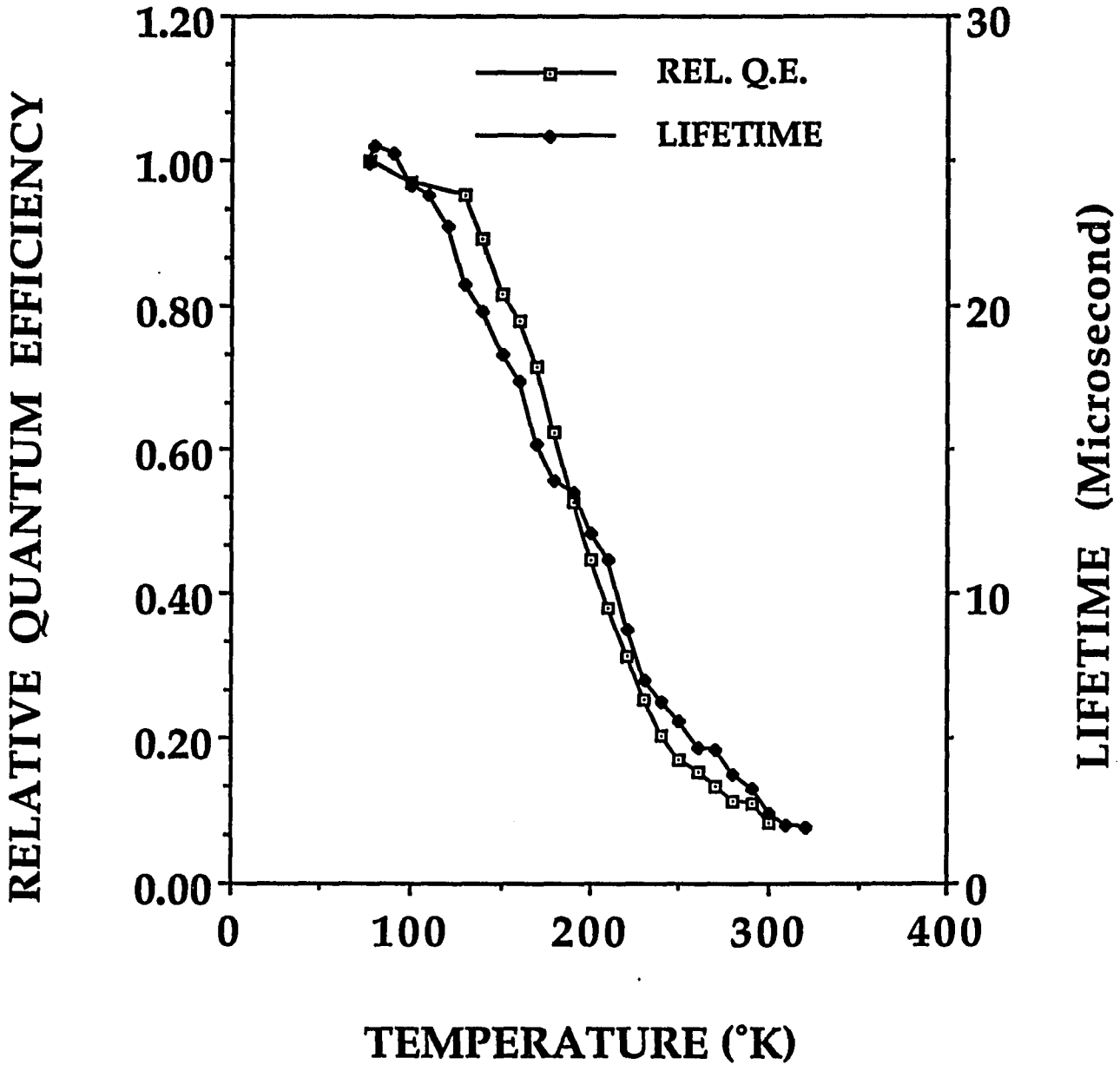

Fig. 2.4.14 Temperature dependence of the fluorescence lifetime and relative quantum efficiency of $Cr:Mg_2SiO_4$ (sample 1) emission in the 1100-1400 nm wavelength range, for 1064-nm excitation. The emission is attributed to tetrahedral Cr^{4+}.

the room temperature and the liquid nitrogen temperature lifetimes in the same wavelength region (1100 - 1400 nm) were identical for the two samples. The results are presented in Figure 2.4.14. Temperature dependence of the fluorescence lifetime and relative quantum efficiency indicate presence of strong nonradiative relaxation for Cr^{4+} ions, which is not so prominent for Cr^{3+} ions in this temperature range.

2.4.5 Excitation Spectra

Excitation spectra of sample 1 were measured in two different wavelength ranges, around $\lambda = 900$ nm and $\lambda > 1100$ nm in order to separate contributions from different optically active centers. The excitation spectra, corrected for the excitation intensity, are presented in Figs. 2.4.15 and 2.4.16. The excitation spectrum monitored at 900 nm, close to the peak of the Cr^{3+} emission, clearly resembles the absorption spectrum of Cr^{3+} in forsterite grown in a reducing atmosphere (sample 3) which does not contain Cr^{4+}. For $\lambda > 1100$ nm excitation spectrum is analogous to the absorption spectra of samples 1 and 2, where the dominant features are those attributed to tetrahedrally coordinated Cr^{4+}.

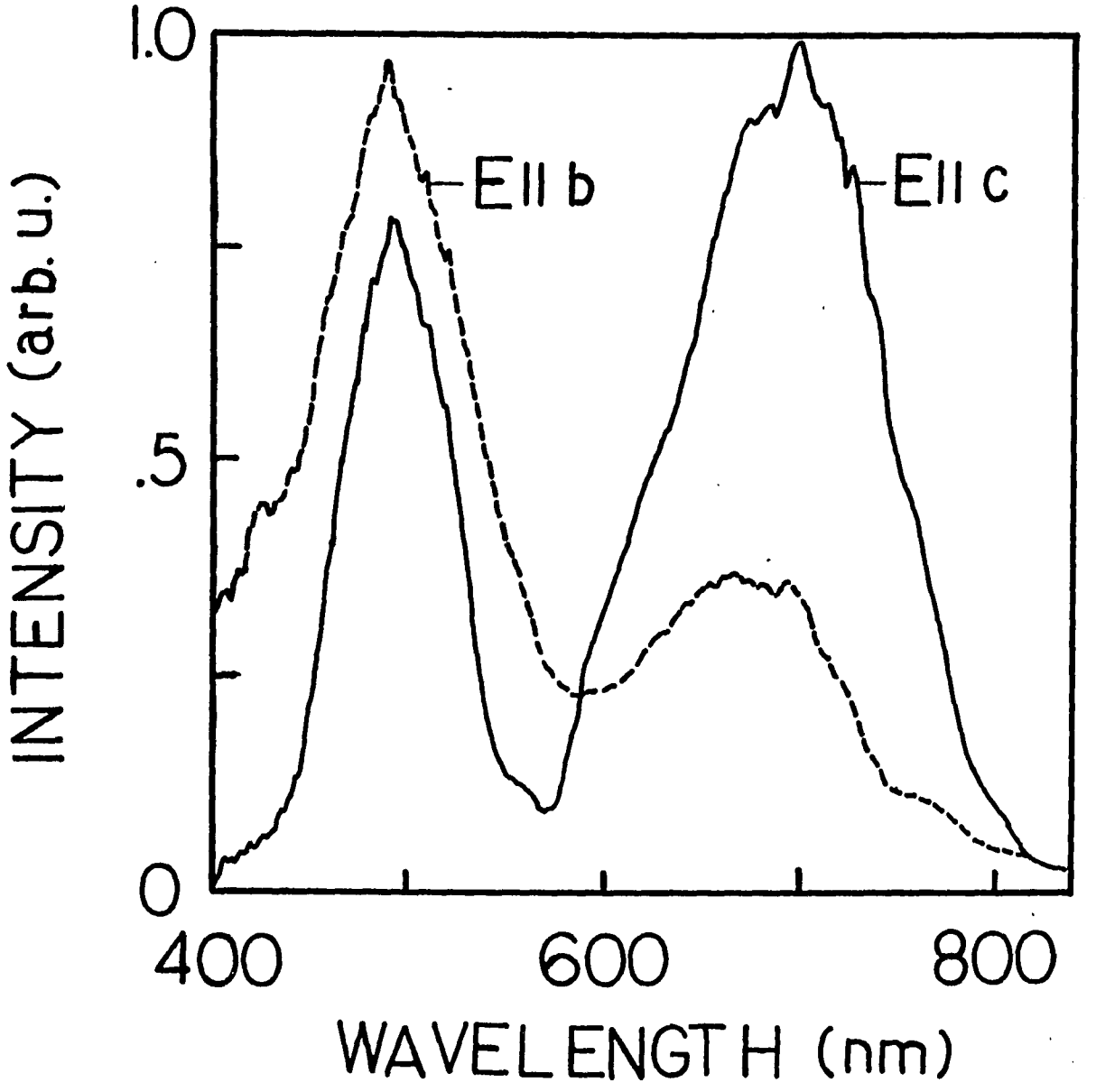

Fig. 2.4.15 Room-temperature excitation spectrum of Cr:Mg_2SiO_4 (Sample 1) monitored at 900 nm for two different orientations.

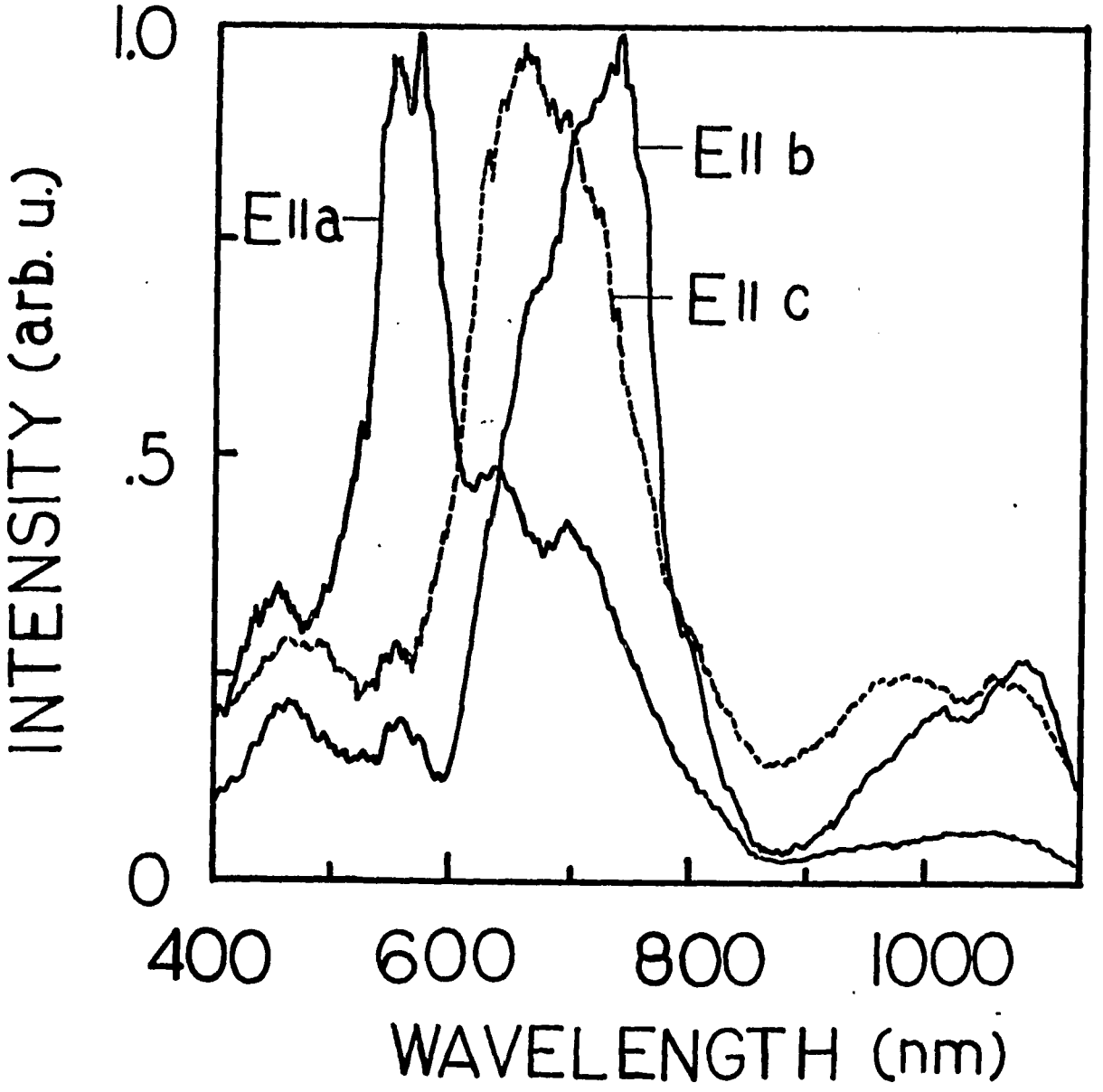

Fig 2.4.16 Room-temperature excitation spectrum of Cr:Mg_2SiO_4 (Sample 1) monitored in the wavelength range $\lambda > 1100$ nm for all three crystallographic orientations.

2.5 Conclusions

Measurements of the absorption, emission and excitation spectra, as well as the wavelength dependence of fluorescence lifetime provide convincing evidence that chromium ion may enter forsterite (Mg_2SiO_4) host in more than one valence states. Trivalent chromium (Cr^{3+}) enters substitutionally for divalent magnesium (Mg^{2+}) in two inequivalent octahedrally coordinated sites, while tetravalent chromium (Cr^{4+}) substitutes for Si^{4+} at tetrahedrally coordinated sites. Of the two Cr^{3+} centers, the one with mirror symmetry (C_s) is optically active and accounts for a number of features in the absorption and emission spectra. The center with inversion symmetry (C_i) is characterized with longer lifetimes that show strong temperature dependence. Features attributed to the Cr^{3+} ion in the inversion site are much more prominent in the sample 1 which has higher chromium ion concentration. The absorption and emission due to transitions within the states of Cr^{4+} ion overlap with those within the states of Cr^{3+} ion. The absorption in the near infrared spectral region between 850 and 1150 nm is primarily due to transitions between the $^3A_2$ ground state and the first excited state $^3T_2$, of the Cr^{4+} ion. The four-level, vibronic mode of laser operation in Cr-doped forsterite feeds on $^3T_2 \rightarrow {}^3A_2$ transition.

2.6 Appendices

2.6.1 Tanabe-Sugano Matrices for Tetrahedral $3d^2$ Ions[31]

Energy Matrices for the Configuration d^2 in a Cubic Field

$^1A_1$	t^2	10B + 5C - 10Dq	$\sqrt{6}$(2B + C)
	e^2	$\sqrt{6}$(2B + C)	8B + 4C + 10Dq
$^3A_2$	t^2	-8B + 10Dq	
^1E	t^2	B + 2C - 10Dq	$-2\sqrt{3}$B
	e^2	$-2\sqrt{3}$B	2C + 10Dq
$^1T_1$	et	4B + 2C	
$^3T_1$	t^2	-5B - 10Dq	6B
	et	6B	4B
$^1T_2$	t^2	B + 2C - 10Dq	$2\sqrt{3}$B
	et	$2\sqrt{3}$B	2C
$^3T_2$	et	-8B	

2.6.2 Tanabe-Sugano Matrices for Octahedral $3d^3$ Ions[31]

Energy Matrices for the Configuration d^3 in a Cubic Field

$^2T_2(a^2D,b^2D,^2F,^2G,^2H)$					
t^3	-12Dq + 5C	-3√3B	-5√3B	4B + 2C	2B
$t^2(^3T_1)e$		-2Dq - 6B + 3C	3B	-3√3B	-3√3B
$t^2(^1T_2)e$			-2Dq + 4B + 3C	-√3B	√3B
$te^2(^1A_1)$				8Dq + 6B + 5C	10B
$te^2(^1E)$					8Dq - 2B + 3C

$^2T_1(^2P,^2F,^2G,^2H)$					
t^3	-12Dq - 6B + 3C	3B	3B	0	-2√3B
$t^2(^3T_1)e$		-2Dq + 3C	-3B	3B	3√3B
$t^2(^1T_2)e$			-2Dq - 6B + 3C	-3B	-√3B
$te^2(^3A_2)$				8Dq - 6B + 3C	2√3B
$te^2(^1E)$					8Dq - 2B + 3C

$^2E(a^2D,b^2D,^2G,^2H)$				
t^3	-12Dq - 6B + 3C	-6√2B	-3√2B	0
$t^2(^1A_1)e$		-2Dq+ 8B + 6C	10B	√3(2B + C)
$t^2(^1E)e$			-2Dq - B + 3C	2√3B
e^3				18Dq - 8B + 4C

$^4T_1(^4P,^4F)$		
$t^2(^3T_1)e$	-2Dq - 3B	6B
$te^2(^3A_2)e$		8Dq - 12B

$^4A_2(^4F)t^3$	-12Dq - 15B
$^4T_2(^4F)t^2(^3T_1)e$	-2Dq - 15B
$^2A_1(^2G)t^2(^1E)e$	-2Dq - 11B + 3C
$^2A_2(^2F)t^2(^1E)e$	-2Dq + 9B + 3C

2.6.3 The Procedure for Fitting the Experimental Data

Tanabe -Sugano matrices given in sections A 2.1 and A 2.2 were diagonalized in order to calculate the energy levels for Cr^{3+} and Cr^{4+} ions in chromium-doped forsterite which are given in Tables 2.4.1 and 2.4.2. Sharp features in the spectra such as $^1T_1$ and $^3T_1$ bands in the UV spectral region and 1E band in the visible, for Cr^{4+} were used to obtain initial estimates for Dq and B parameters, which are used as fitting parameters in this model. Parameter C was calculated assuming that the ratio C/B does not change from its free-ion value. Deviation of the B parameter value from the free-ion value is explained as a consequence of effects of covalency. The sign of the crystal field parameter Dq was changed for the tetrahedral $3d^2$ ion.[31] For bands whose position varies with the polarization of the incident light and the orientation of the crystal, average position (the centroid of three bands marked $^3T_1$ in Fig. 2.4.1, for example) is taken for this analysis.

2.7 References

1. V. Petričević, S. K. Gayen, R. R. Alfano, K. Yamagishi, H. Anzai, and Y. Yamaguchi, Appl. Phys. Lett. **52**, 1040 (1988);

2. V. Petričević, S. K. Gayen, and R. R. Alfano, Opt. Lett. **14**, 612 (1989).

3. V. Petričević, S. K. Gayen, and R. R. Alfano, Appl. Opt. **27**, 4162 (1988).

4. V. Petričević, S. K. Gayen, and R. R. Alfano, Appl. Phys. Lett. **53**, 2590 (1988).

5. H. R. Verdun, L. M. Thomas, D. M. Andrauskas, T. McCollum, and A. Pinto, Appl. Phys. Lett. **53**, 2593 (1988).

6. V. Petričević, S. K. Gayen, and R. R. Alfano, Appl. Opt. **28**, 1609 (1989).

7. A. Sugimoto, Y. Segawa, Y. Yamaguchi, Y. Nobe, K. Yamagishi, P. H. Kim, and S. Namba, Japanese J. Appl. Phys., to be published.

8. V. Petričević, S. K. Gayen, and R. R. Alfano, in *Tunable Solid-State Lasers*, Vol. 5 of the OSA Proceeding Series, M. L. Shand and H. P. Jenssen, eds. (Optical Society of America, Washington, D.C., 1989), pp. 77-84.

9. H. R. Verdun, L. M. Thomas, and D. M. Andrauskas, in *Tunable Solid-State Lasers*, Vol. 5 of the OSA Proceeding Series, M. L. Shand and H. P. Jenssen, eds. (Optical Society of America, Washington, D.C., 1989), pp. 85-92.

10. R. Moncorge, D. J. Simkin, G. Cormier, and J. A. Capobianco, in *Tunable Solid-State Lasers*, Vol. 5 of the OSA Proceeding Series, M. L. Shand and H. P. Jenssen, eds. (Optical Society of America, Washington, D.C., 1989), pp. 93-97.

11. For a list of Cr^{3+}-based tunable solid-state lasers see S. A. Payne, L. L. Chase, L. K. Smith, W. L. Kway, and H. W. Newkirk, J. Appl. Phys. **66**, 1051 (1989).

12. A. A. Kaminskii, A. V. Butashin, A. A. Demidovich, V. G. Koptev, B. V. Mill, and A. P. Shkadarevich, Phys. Stat. Sol. (a) **112**, 197 (1989).

13. N. B. Angert, N. I. Borodin, V. M. Garmash, V. A. Zhitnyuk, A. G. Okhrimchuk, O. G. Siyuchenko, and A. V. Shestakov, Sov. J. Quantum Electron. **18**, 73 (1988).

14. N. Nishide, Y. Segawa, P. H. Kim, S. Namba, and A. Masuyama, Reza Kagaku Kenkyu **7**, 89 (1985).

15. H. Rager and G. Weiser, Bull. Mineral. **104**, 603 (1981).

16. J. R. Smyth and R. M. Hazen, Am. Mineral. **58**, 588(1973).

17. V. Devarajan and E. Funck, J. Chem. Phys. **62**, 3406 (1975)

18. H. Rager, Phys. Chem. Minerals **1**, 371 (1977).

19. L. V. Bershov, J. M. Gaite, S. S. Hafner, and H. Rager, Phys. Chem. Minerals **9**, 95 (1983).

20. G. S. Kruglik, G. A. Skripko, and A. P. Shkadarevich, *Tunable Lasers Utilizing Activated Crystals* (in Russian), Belorussian Polytechnic Institute, Minsk (1984).

21. J. A. Caird, W. F. Krupke, M. D. Shinn, L. K. Smith, and R. E. Wilder, in Technical Digest, Conference on Lasers and Electrooptics (Optical Society of America, Washington, D. C., 1984), paper THR 3, p. 232.

22. J. A. Caird, M. D. Shinn, T. A. Kirchoff, L. K. Smith, and R. E. Wilder, Appl. Opt. **25**, 4294 (1986).

23. S. E. Stokowski, M. H. Randles, and R. C. Morris, IEEE J. Quantum Electron. **24**, 934 (1988).

24. D. M. Gruen and R. Gutt, Nature **190**, 714 (1961).

25. C. K. Jorgensen, Acta Chem. Scand. **8**, 1945 (1954).

26. S. A. Payne, L. L. Chase, L. K. Smith, W. L. Kway, and H. W. Newkirk, J. Appl. Phys. **66**, 1051 (1989).

27. B. E. Scheetz and W. B. White, Contr. Mineral. Petrol. **37**, 221 (1972).

28. R. G. Burns, Contr. Mineral. Petrol. **51**, 213 (1975).

29. S. Sugano, Y. Tanabe, and H. Kamimura, *Multiplets of Transition-Metal Ions in Crystals*, Academic, New York, 1970.

30. F.A. Cotton, *Chemical Applications of Group Theory*, Wiley, New York (1971).

31. D. S. McClure, in *Solid State Physics, Vol. 9,* edited by F. Seitz and D. Turnbull (Academic, New York, 1959), p. 399.

32. R. C. Powell, L. Xi, X. Gang, G. J. Quarles, and J. C. Walling, Phys. Rev. B **32**, 2788 (1985).

CHAPTER 3

LASER PERFORMANCE OF CHROMIUM-DOPED FORSTERITE

3.1 Introduction

Chromium-doped forsterite ($Cr:Mg_2SiO_4$) has been considered as a potential laser crystal in the past.[1-4] However, these efforts were not successful for two reasons. First, the fluorescence spectra were measured with S-1 photomultipliers, which are not sensitive beyond 1 μm and the larger part of the fluorescence band which actually extends almost to 1.5 μm was undetected. This is best illustrated in Fig. 3.1.1 which shows fluorescence spectra of chromium-doped forsterite measured with S-1 photomultiplier compared to the spectra measured with germanium photodiode. Second, attempts were made to reduce the absorption band between 850 and 1150 nm, without much success. The origin of this band was subject of speculation. The near infrared absorption was attributed to color center formation due to charge compensation or to impurity ions such as Fe^{3+} in the host crystal. Despite all the efforts, laser experiments in the 800 - 900 nm region failed.

When the fluorescence spectrum was measured with a proper photodetector such as a Ge photodiode it became obvious that there is enough fluorescence in the wavelength region beyond 1200 nm where there is no ground state absorption.[5] This fact made a basis for all developments that followed. With a laser cavity designed for 1.2 - 1.3 μm wavelength range, pulsed[5-7] and continuous-wave[8] laser action was obtained and tunability was demonstrated.[9] The lasing center was further identified

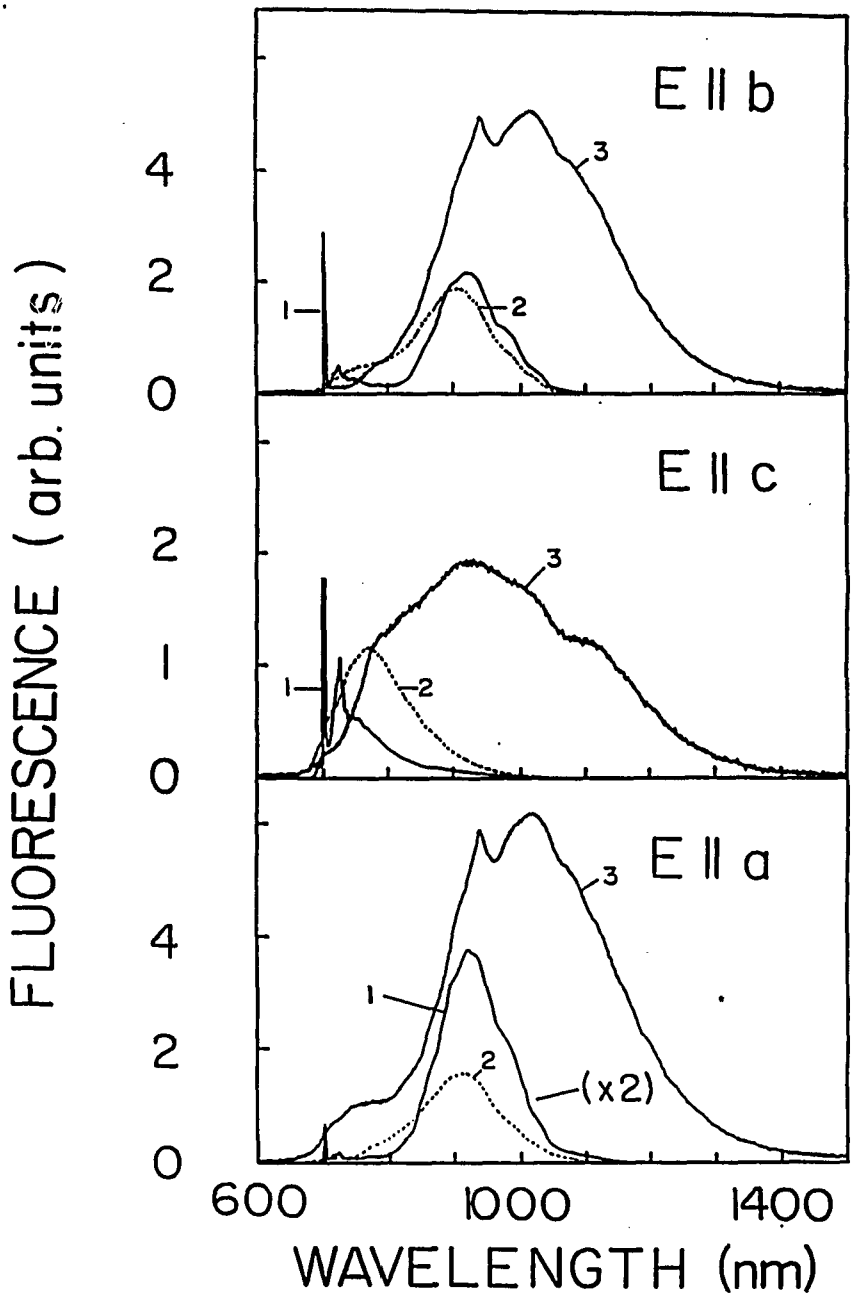

Figure 3.1.1 Room temperature and liquid nitrogen temperature fluorescence spectra of Cr:Mg_2SiO_4 (sample 1) measured with a S-1 photomultiplier tube (curves 1 and 2) compared with the room temperature fluorescence spectra measured with a germanium photodiode (curves 3). All spectra were excited with 488-nm argon-ion laser radiation.

as tetravalent chromium (Cr^{4+}).[7,10] (See Chapter 2) It turned out that the absorption band in the near infrared due to Cr^{4+}, considered to be parasitic, is essential for laser operation, and even could be used to pump the forsterite laser.

In this chapter, laser operation of chromium-doped forsterite is presented. In section 3.2 initial laser experiments for 532-nm and 1064-nm pumping are qualitatively described. In section 3.3 pulsed laser experiments with optimized cavity are presented. Section 3.4 is devoted to tuning experiments and section 3.5 deals with continuous-wave laser operation. Finally, in section 3.6 conclusions are made and directions for future development of practical laser systems are outlined.

3.2 Pulsed Laser Operation. Initial Experiments

3.2.1 532-nm Pumping[5]

First successful attempt to obtain laser action in $Cr:Mg_2SiO_4$ was made with sample 1, described in section 2.2. The room-temperature fluorescence and absorption spectra of that sample for $E \| b$ crystallographic axis are shown in Fig. 3.2.1. The absorption was measured along the *a* axis. The fluorescence spectrum was excited by the 488-nm radiation from an argon-ion laser and recorded by a germanium photodiode. It is evident from Fig. 3.2.1 that the shallow absorption band between 850 and 1150 nm overlaps a significant spectral region of Cr: Mg_2SiO_4 emission, and inhibits laser action in that wavelength range.

The approach that was taken was to design a laser cavity for the wavelength region where there is no significant background absorption. The experimental arrangement for investigating the laser action in $Cr:Mg_2SiO_4$ is shown schematically

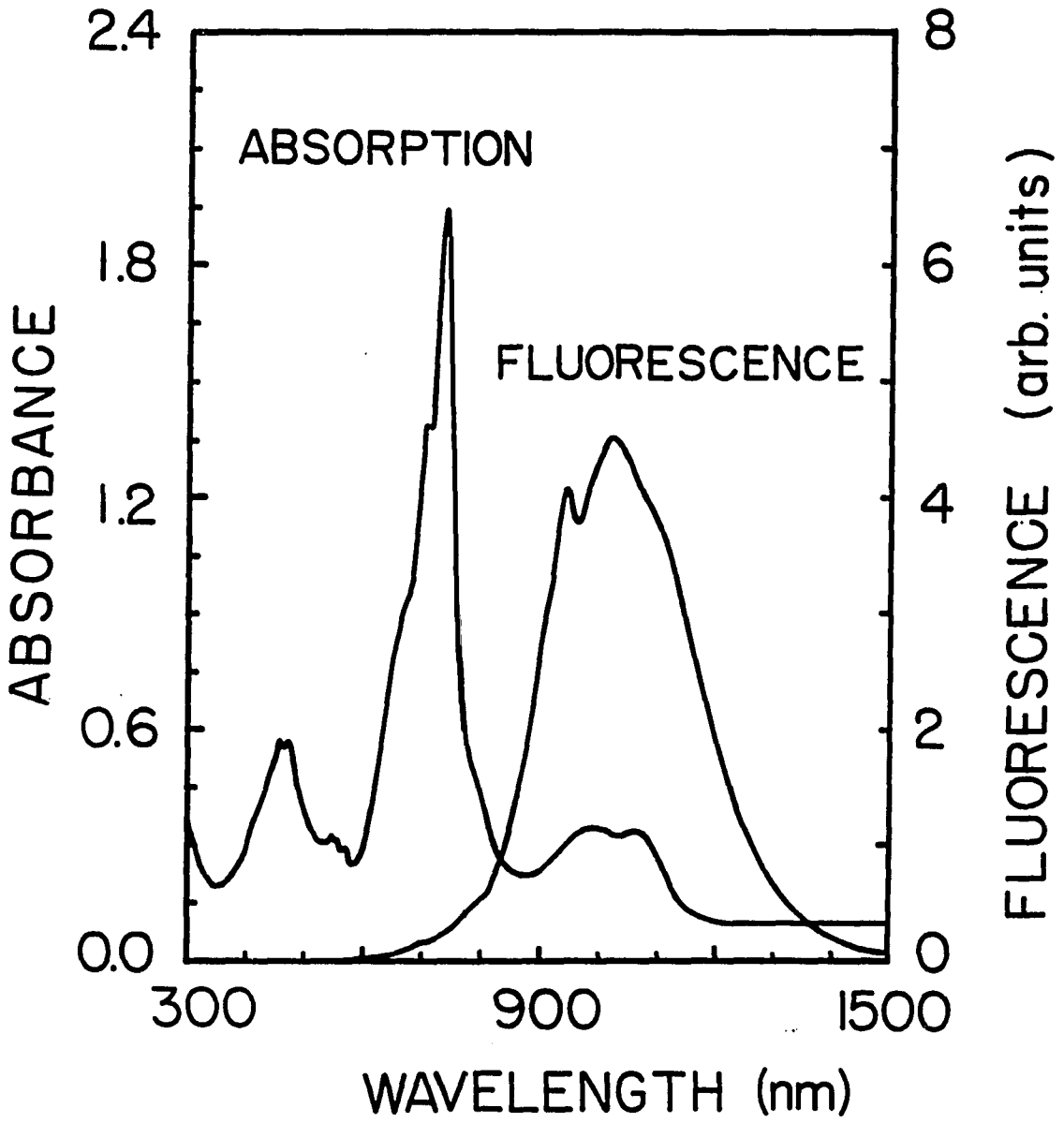

Figure 3.2.1 Absorption and fluorescence spectra of Cr:Mg_2SiO_4 (sample 1) at room temperature. Both the spectra were taken for E $\|$ b axis and excitation along the a axis. The thickness of the sample along the a axis is 4.5 mm.

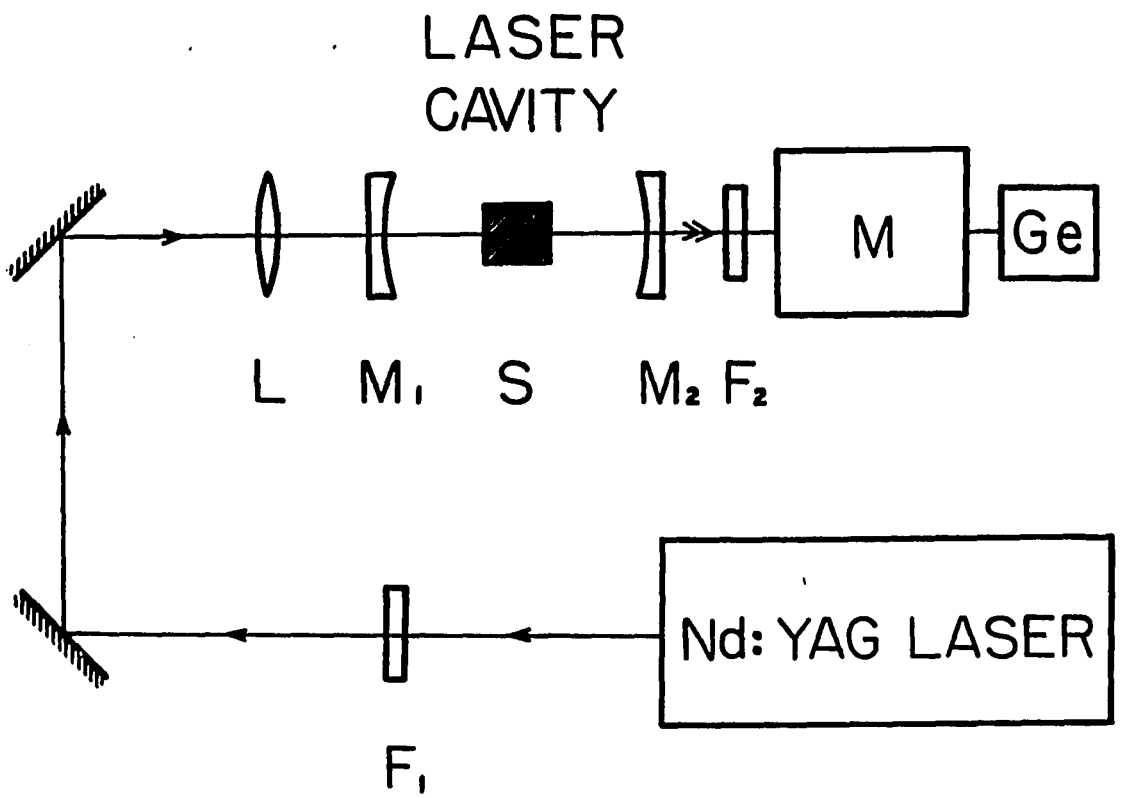

Figure 3.2.2 Schematic diagram of the experimental arrangement for investigating laser action in Cr:Mg_2SiO_4. Key: F1 = 1064-nm blocking filter, F2 = 532-nm blocking, infrared transmitting filter, M1 = back mirror, M2 = output mirror, L = lens, S = sample, Ge = germanium photodiode detector, M = monochromator.

in Fig.3.2.2. The chromium-doped forsterite crystal was placed at the center of a stable resonator formed by two 30-cm-radius-of-curvature mirrors placed 20 cm apart.The mirrors were dielectric coated to transmit the 532-nm pump beam, and to have high reflectivity in the 1150 - 1250 nm spectral range. The reflectivity of the back mirror M_1 is 99.9%, while that of the output mirror M_2 is ~98% for normal incidence overthe specified wavelength range. This spectral region does not correspond to the peak of the fluorescence spectrum, but was chosen so that the absorption is minimal. The sample was longitudinally pumped by frequency-doubled 532-nm, 10-ns full-width-at-half-maximum (FWHM) pulses from a Q-switched Nd:YAG laser (Quanta Ray DCR-1) operating at 10 Hz repetition rate. The spatial profile of the pump pulse was doughnut, a characteristic of an unstable cavity.The pump beam was linearly polarized along the *b* axis and propagated along the *a* axis of the sample. To avoid damaging the sample, the pump beam was focused 3 cm before the smple by a 25-cm focal length lens. The radius of the pump beam at the center of the sample was ~600 μm. No attempt was made to better match the pump beam to the cavity mode. The output from the laser cavity was analyzed by a 0.25-m monochromator and monitored by a germanium photodiode detector. The output of the detector was displayed on a fast oscilloscope. No dispersive element was placed in the cavity and the laser operated in a free-running pulsed mode.

Pulsed laser operation was readily observed for pumping at or above the lasing threshold of 2.2 mJ. A single output laser pulse was obtained, implying a gain-switched mode of operation which is a consequence of pump-pulse duration being much shorter than the lasing-level lifetime. The amplitude and duration of the laser pulse varied, as expected, with the pulse-to-pulse energy fluctuation of the

pump laser. The output was extremely sensitive even to a small misalignment of the cavity, or insertion of a glass plate (8% loss) in the cavity.

The temporal profile of the $Cr:Mg_2SiO_4$ laser pulse is shown in Fig. 3.2.3 (a), and fluctuations in its amplitude, duration, and delay with respect to the pump pulse are displayed in Fig. 3.2.3 (b). The temporal duration (FWHM) of the output laser pulse varied from 200 ns at the threshold to 100 ns at 2.4 times the threshold energy. The delay between the peak of the pump pulse and the peak of the $Cr:Mg_2SiO_4$ laser pulse also varied with pump-pulse energy, from 700 ns at the threshold to less than 200 ns at 2.4 times the threshold energy. This indicated that the laser cavity is highly lossy, and several hundred round trips are required to build up the laser oscillation in the cavity.

The laser threshold and slope efficiency were measured for the cavity used in this experiment and the result is displayed in Fig. 3.2.4. The laser oscillation starts to build up at an absorbed input energy of 2.2 mJ. The measured slope efficiency of 1.4% is rather low, and indicates large losses in the cavity. These losses include ~13% reflection loss from the uncoated sample surfaces, scattering from inhomogeneities in the crystal, and a large mismatch between the size of the pump beam and the $Cr:Mg_2SiO_4$ cavity modes in the sample.

The spectrum of the $Cr:Mg_2SiO_4$ laser is shown in Fig. 3.2.5, for an absorbed pump energy of 3.4 mJ. The spectrum peaks at 1235 nm and has a bandwidth (FWHM) of 22 nm.

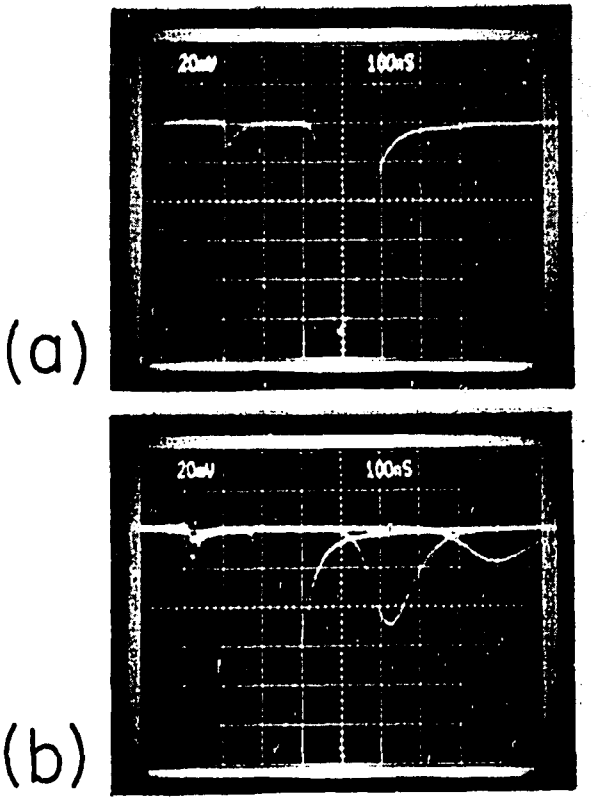

Figure 3.2.3 Temporal profile and delay with respect to the pump pulse of the Cr:Mg_2SiO_4 laser pulse: (a) a single pulse for pump energy 1.7 times the threshold energy; and (b) three pulses for pump energies near (right), twice (middle), and 2.4 times (left) the threshold energy. The narrow pulse at the extreme left of both the oscilloscope traces is the leakage of the pump pulse. For this measurement the monochromator was removed and filters were adjusted to allow a small leakage of pump pulse. The time and voltage scales are 100 ns/div and 20 mV/div, respectively.

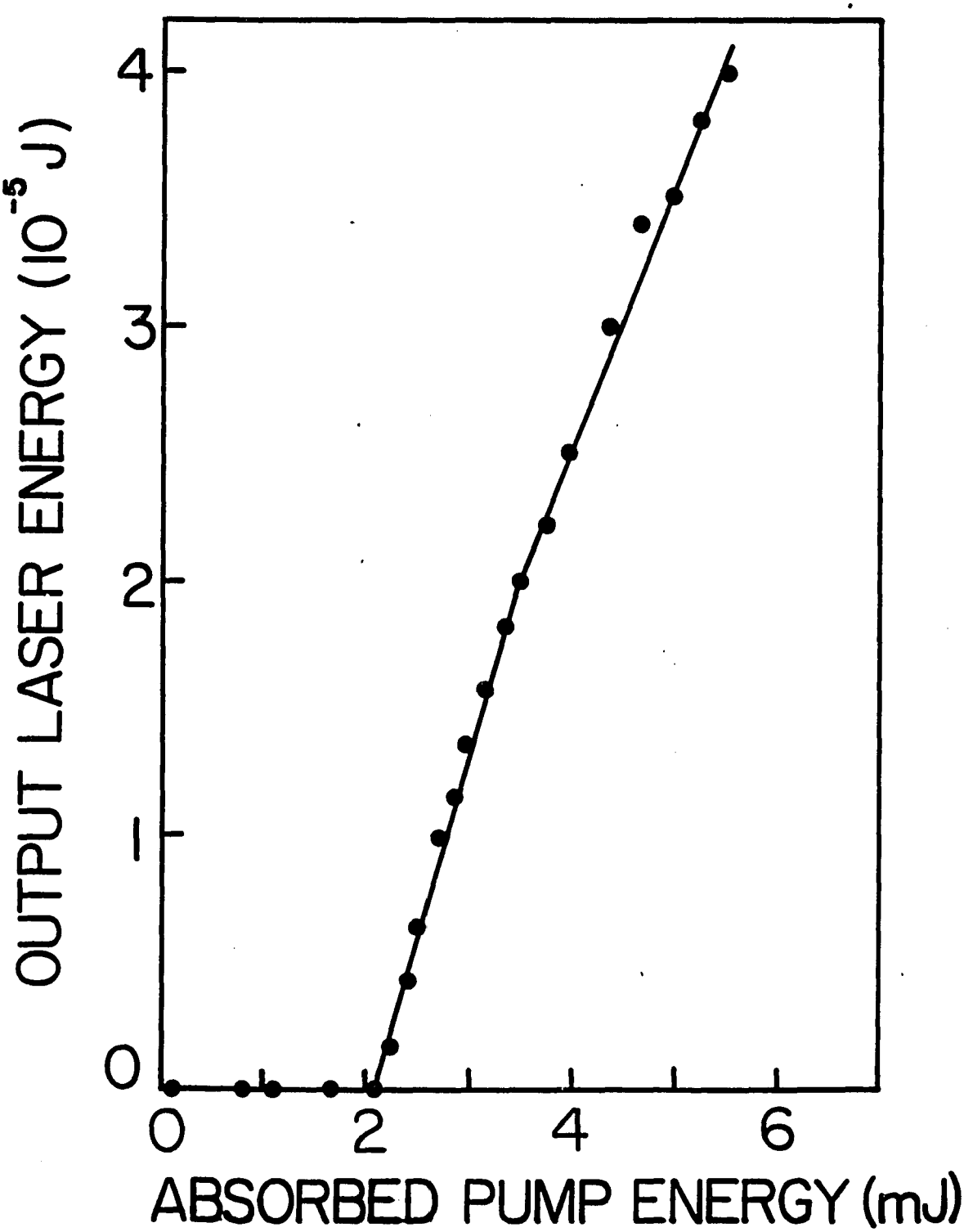

Figure 3.2.4 Output energy of Cr:Mg_2SiO_4 laser as function of input energy for 532-nm pumping.

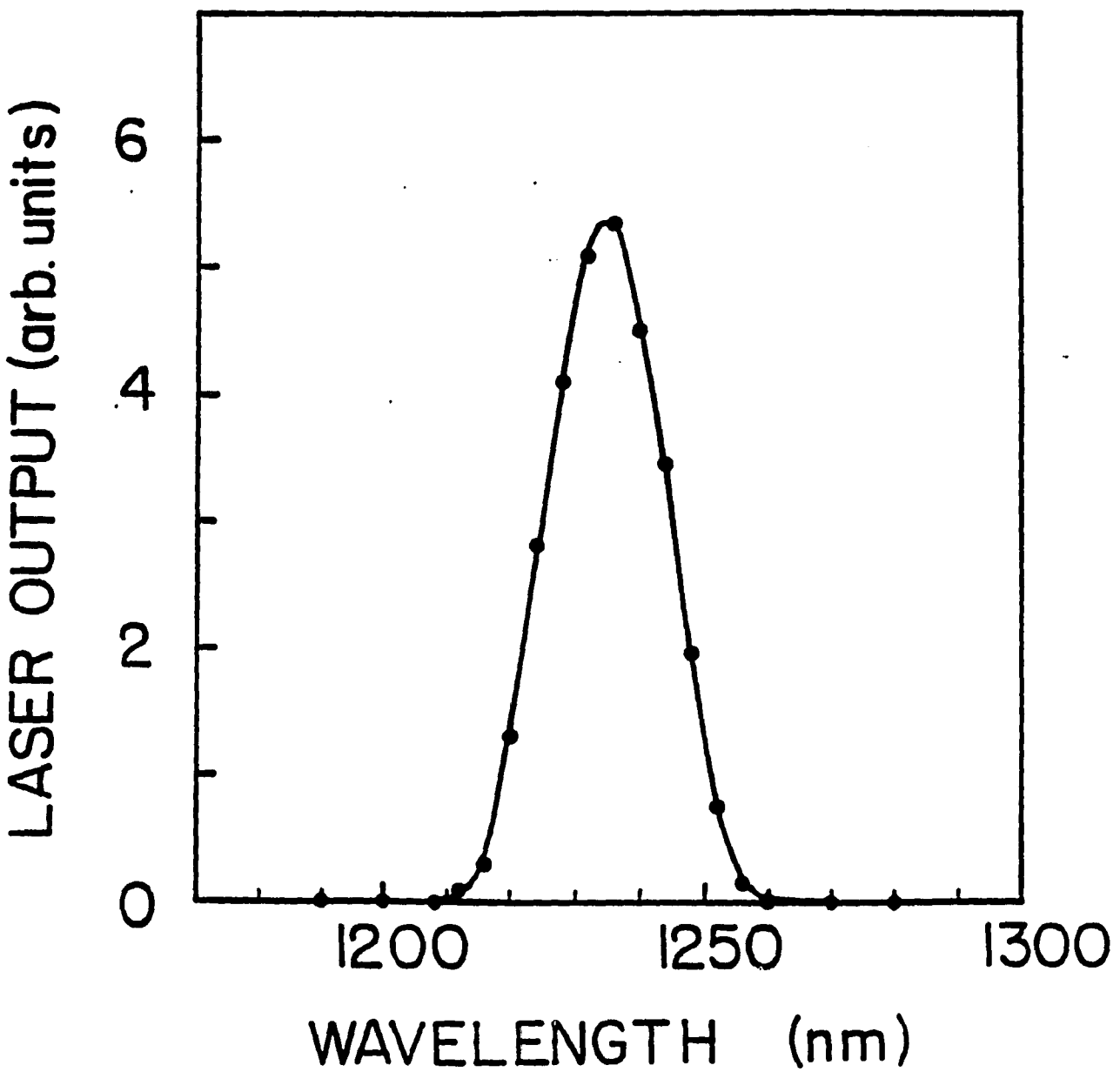

Figure 3.2.5 Spectrum of the free-running Cr:Mg_2SiO_4 laser for 532-nm pumping.

3.2.2 1064-nm Pumping[6]

It was shown in the previous chapter that when the near infrared absorption band in Cr:Mg_2SiO_4 spanning the 850 - 1150 nm wavelength range is pumped by 1064-nm fundamental radiation of Nd:YAG laser, the Stokes-shifted fluorescence extends beyond 1400 nm with maximum at 1140 nm. The absorption and fluorescence spectra in the near infrared region are shown in Fig. 3.2.6.

The near infrared absorption thus turns out to be effective in populating the initial level of the lasing transition. Having that in mind another lasing experiment was attempted. An identical arrangement was used in this measurement as the one described in section 3.2.1, except that the separation between the mirrors was 40 cm, and the pump beam was focused 5 cm in front of the sample by a 50-cm focal length lens. The fundamental and the second-harmonic emissions from a Q-switched Nd:YAG laser were used for excitation of near infrared and the visible bands, respectively. Pulsed laser action was readily observed for both the 1064-nm and the 532-nm pumping at or above the respective thresholds. To switch from one pump wavelength to the other, one merely had to change a filter in the beam path to transmitthe desired wavelength and block the other. The amplitude and duration of the Cr:Mg2SiO4 laser pulse, as well its delay with respect to the pump pulse, varied, as expected, with the pulse-to-pulse energy fluctuation of the pump pulses. However, for a similar level of excitation and within the time resolution of the experiment, there was no appreciable difference in the delay between the pump pulse and the output laser pulse for the two pump wavelengths. The laser thresholds and slope efficiences for the two excitation wavelengths, 1064 and 532 nm, are shown in Fig. 3.2.7. The spectra of the free-running laser for pumping at 1064 and 532 nm are displayed in Figs. 3.2.8 (a) and (b), respectively.

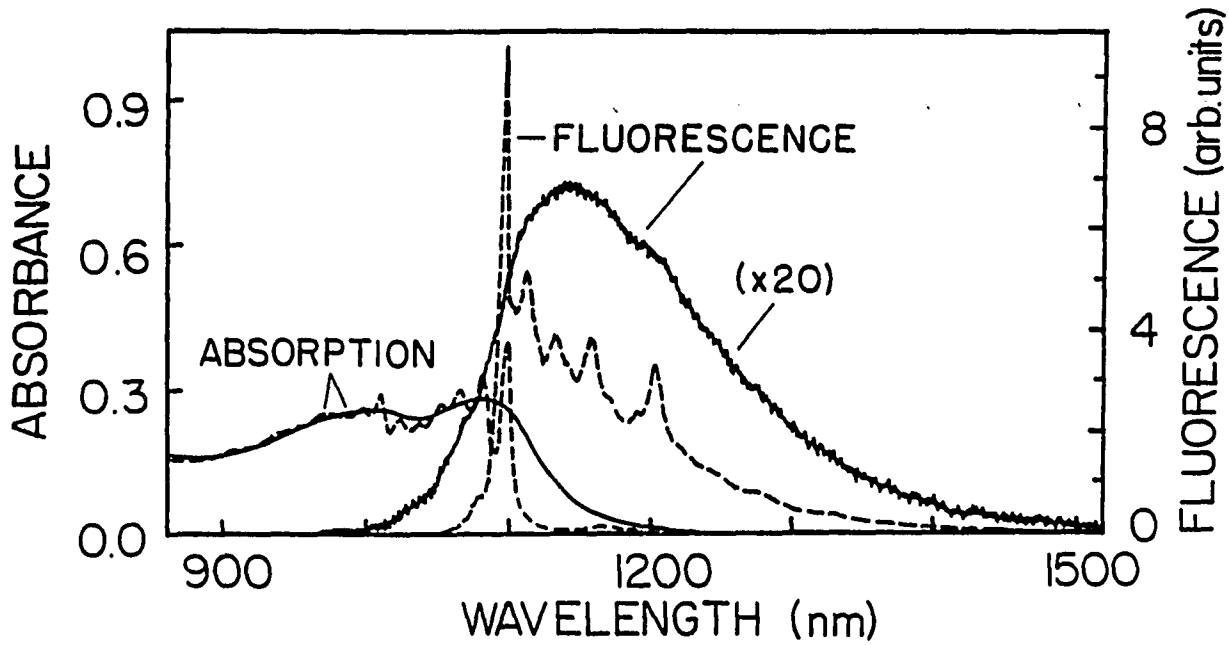

Figure 3.2.6 Near infrared absorption spectrum and fluorescence spectrum for 1064-nm excitation of Cr:Mg_2SiO_4 at room temperature (solid line) and liquid nitrogen temperature (broken line) for E $\|$ b axis.

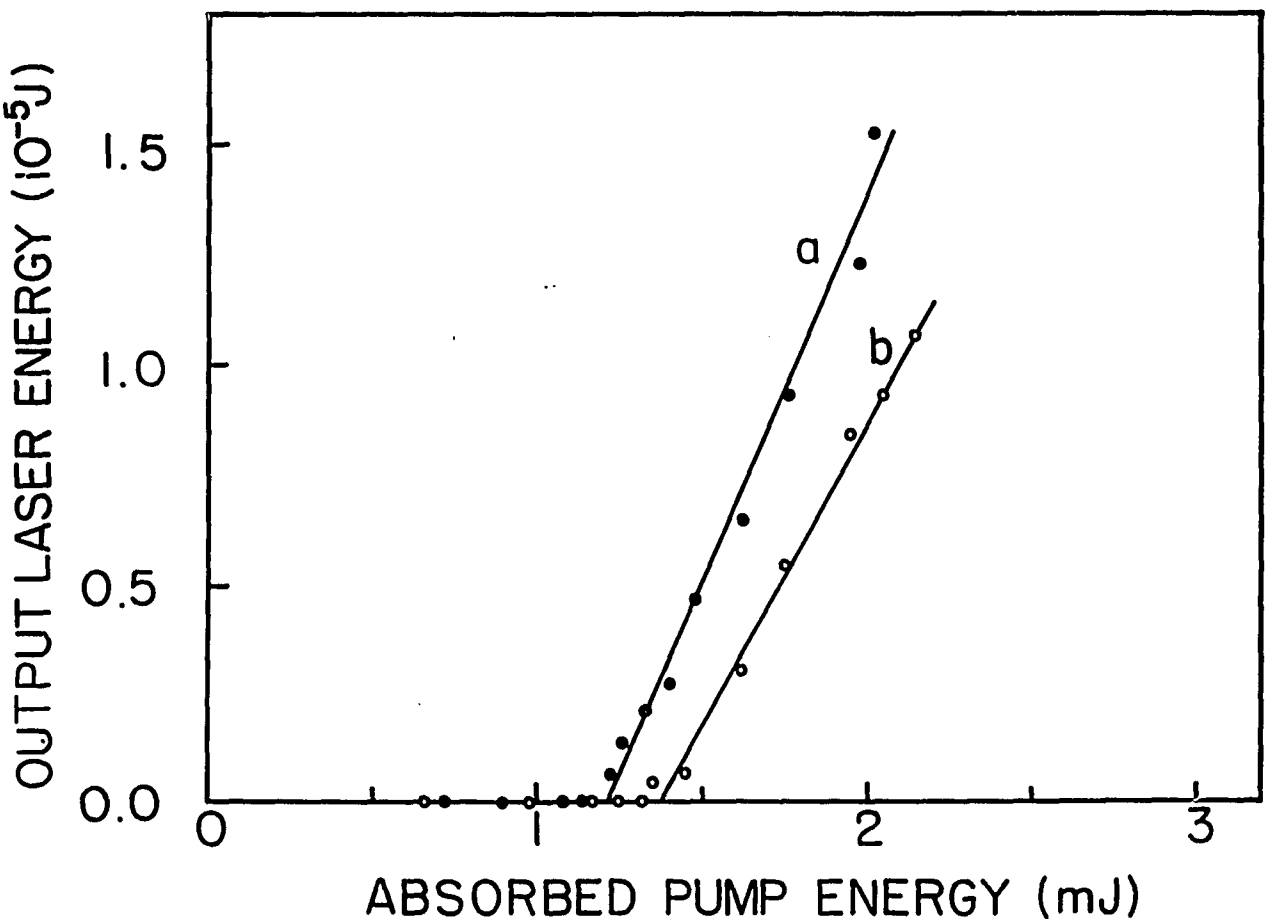

Figure 3.2.7 Output energy of Cr:Mg_2SiO_4 laser as a function of input energy for (a) 1064-nm pumping and (b) 532-nm pumping.

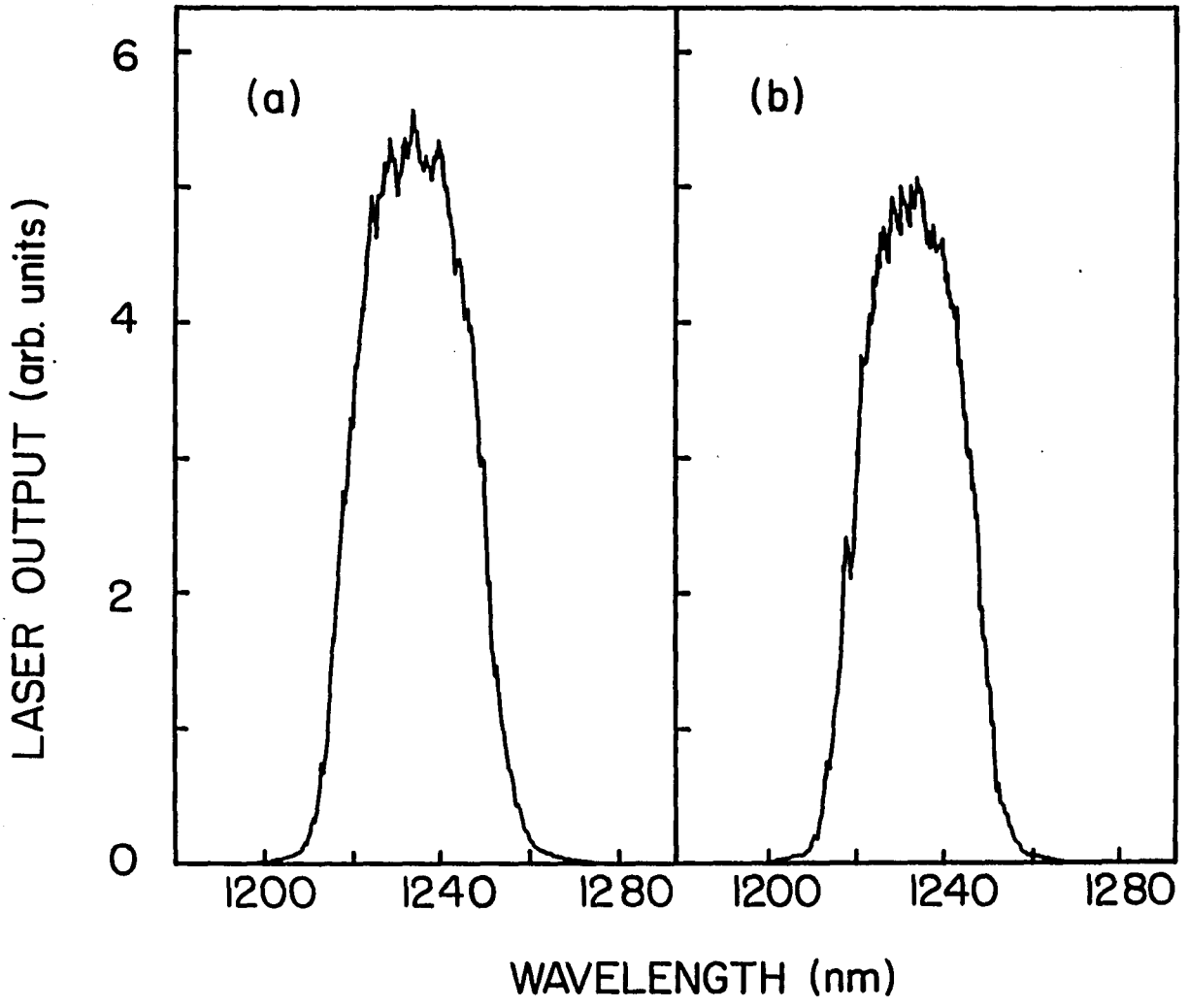

Figure 3.2.8 Spectra of the free-running Cr:Mg_2SiO_4 laser for (a) 1064-nm pumping and (b) 532-nm pumping.

Table 3.2.1 Properties of laser emission for the two excitation wavelengths

Property	Value at the excitation wavelength of	
	1064 nm	532 nm
Lasing threshold (absorbed energy)	1.25 mJ	1.37 mJ
Slope Efficiency	1.8 %	1.4 %
Spectral Bandwidth (FWHM)	30 nm	27 nm
Center Wavelength	1235 nm	1235 nm

Table 3.2 summarizes and compares the characteristics of laser emission for the two excitation wavelengths.

From the presented experimental data and from the spectroscopic measurements described in the previous chapter it is clear that the same center, tetravalent chromium (Cr^{4+}) is active in laser action for both the 532-nm and 1064-nm excitations. For the 1064-nm pumping the $^3T_2$ lasing band of Cr^{4+} ion is directly populated. For the 532-nm pumping there is a fast transfer of excitation from the levels directly pumped to the lasing level. However, at this point it is not clear whether the Cr^{3+} absorption of the 532-nm excitation contributes to the lasing action, or it is only the energy absorbed by Cr^{4+} that is transfered to the upper lasing level via nonradiative processes. A detailed study of the $Cr^{3+} \rightarrow Cr^{4+}$ energy-transfer processes in chromium-doped forsterite is needed to determine the role of Cr^{3+} as sensitizer in this laser system. This may be of particular importance for flash-lamp pumping.

3.3 Pulsed Laser Operation of the Optimized Cr:Mg_2SiO_4 Laser

Laser operation experiments described in section 3.2 were only qualitative. No attempts were made to optimize the laser system in order to improve input/output efficiency. In this section, a set of experiments on pulsed laser operation is described, where some of the losses mentioned earlier were reduced.

To improve the laser performance, sample 2, described in section 2.2 was anti-reflection coated such that reflectivity over the 1050-1250 nm range was less than 0.5%. Spatial profile of the pump beam was Gaussian. Attempts were made to overlap the pump beam and the cavity mode more accurately. The sample was

longitudinally pumped by 1064-nm, 10-ns FWHM pulses from a Q-Switched Nd:YAG laser operating at a 10 Hz repetition rate in a cavity similar to that used earlier. The pump beam was linearly polarized along the *b* axis and propagated along the *a* axis of the crystal. The 1064-nm beam was focused into the center of the sample by a 50-cm focal length lens. The waist of the cavity mode at the sample site was ~225 μm. The position of the focusing lens was adjusted to optimize the overlap between the pump beam spot size and the cavity mode waist monitored by maximizing the output. Different sets of laser mirrors were used. Summary of laser performance for three different laser cavities is presented in Table 3.3.1. Center wavelengths shown in Table 3.3.1 differ for three different output couplers since those have slightly different wavelength-dependent transmission characteristics.

Output energy of the forsterite laser as a function of absorbed pump energy for three different output couplers is shown in Fig. 3.3.1.

Using data from Table 3.3 we have estimated the passive loss L of the forsterite laser and calculated the laser gain cross section. Passive (internal) loss L can be estimated by taking the ratio of the threshold pump energies for two different output mirrors or taking the ratio of slope efficiencies,[11] assuming that

$$E_{thi} \sim L + T_i \qquad (1)$$

and

$$\eta_i \sim T_i/(L+T_i),\ i = 1,2 \qquad (2)$$

where T_i is the output mirror transmission. Loss L is then given by

$$L = (T_2 - R_{th}T_1)/(R_{th} - 1) \qquad (3)$$

where

$$R_{th} = E_{th2}/E_{th1}\,, \qquad (4)$$

or

$$L = (R_\Delta - 1)T_1T_2/(T_2 - R_\Delta T_1) \qquad (5)$$

where

$$R_\Delta = \eta_2/\eta_1\,. \qquad (6)$$

For various combinations of output mirrors a value of 11% for the round trip loss L was obtained by using both techniques.

Laser gain cross section shown in Table 3.3.1 for three different output mirrors was calculated using the expression[12]

$$\sigma = \frac{\pi\tau_P h\nu_P \omega_L^2 (L+T)(a^2+1)}{4\eta\left[1-\exp(-\alpha l)\right]\left[1-\exp(-\tau_P/\tau)\right]E_{P\,th}} \qquad (7)$$

where τ_P is the pump pulsewidth, $h\nu_P$ is the pump photon energy, ω_L is the cavity mode spot size, L is laser internal loss, T is the output mirror transmission, $a=\omega_P/\omega_L$, where ω_P is the pump beam spot size, τ is the upper lasing level radiative lifetime taken to be ~25 μs (the liquid nitrogen temperature fluorescence lifetime), α is the absorption coefficient for the pump radiation, l is the length of the crystal, and E_{Pth} is the threshold pump energy incident on the crystal.

TABLE 3.3.1 : Summary of Laser Parameters for Pulsed Laser Operation of Cr:Mg_2SiO_4 Laser (1064-nm pumping)

Parameter	Output Coupling 13%	2%	6%
Lasing Wavelength	1200 nm	1235 nm	1250 nm
Free-running Bandwidth	-	30 nm	-
Threshold Abs. Energy	0.38 mJ	0.20 mJ	0.27 mJ
Slope Efficiency	22.8%	5.1%	12.1%
Gain Cross Section (10^{-19} cm^2)	1.40	1.44	1.40

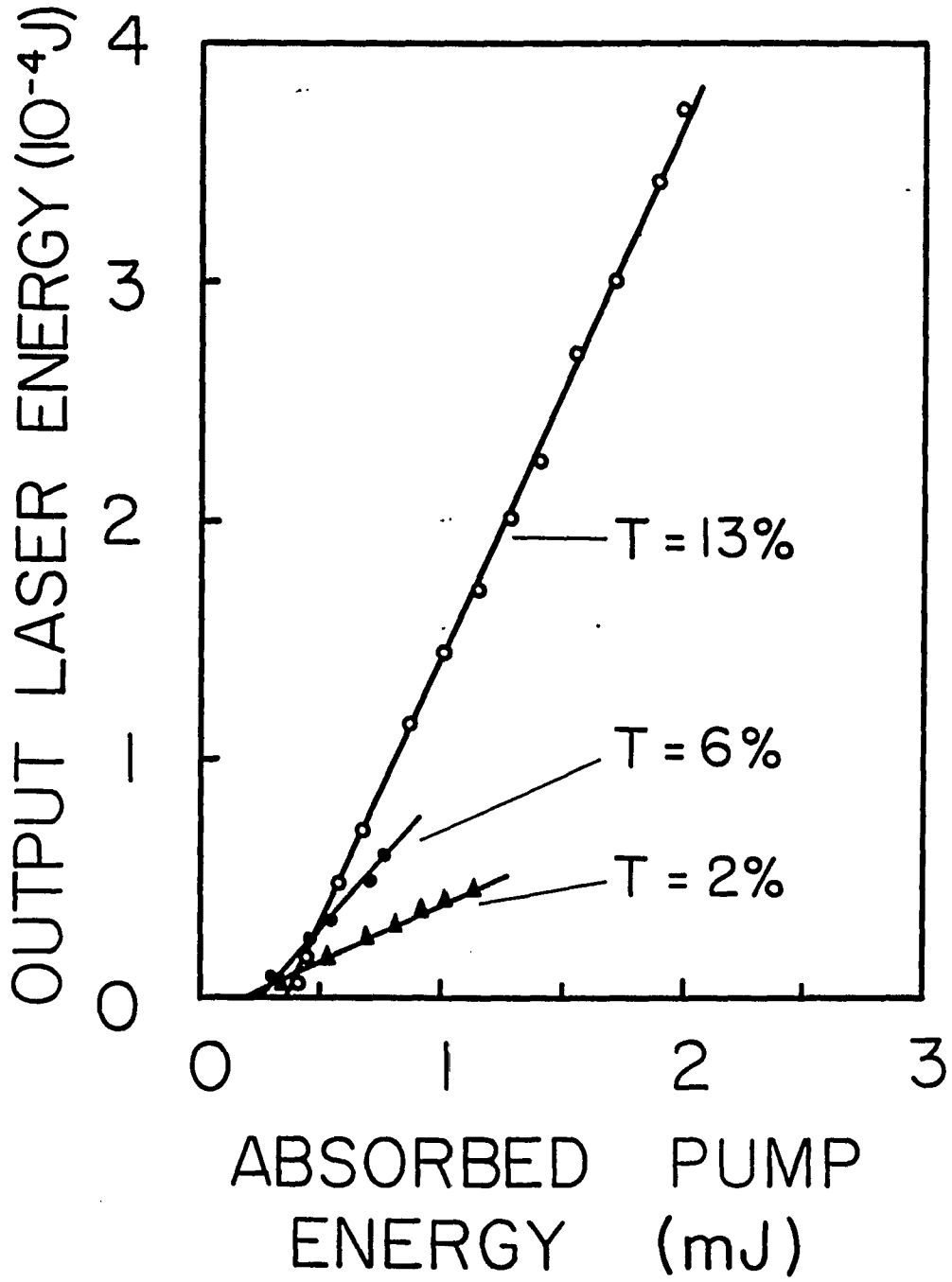

Figure 3.3.1 Output energy of Cr:Mg_2SiO_4 laser as a function of absorbed pump energy for 1064-nm pumping and E ⊥ b axis for three different output couplers.

3.4 Tunable Operation of the Cr:Forsterite Laser[9]

The practical utility of a vibronic solid state laser is determined, to a great extent,by the wavelength range over which it can be tuned effectively.Laser emission in the infrared is of great technological importance for eye-safe ranging, remote sensing, and probably the most important application, optical communications. A number of chromium-based tunable solid state lasers, together with a $Ti^{3+}:Al_2O_3$ laser, span a spectral range of 660 - 1250 nm. A chromium-activated forsterite laser is unique since it extends the tuning range further into the near infrared to 1345 nm. The most important feature of the tuning range of the Cr:forsterite laser is that its tuning range covers 1.3 μm, the wavelength of minimal dispersion in silica fibers.

The room temperature fluorescence spectrum of Cr:forsterite covers the 680 - 1400 nm wavelength range. Laser operation has been obtained in the low energy infrared end of this fluorescence band. The absorption spectrum overlaps most of the high energy end including the peak of the fluorescence spectrum and inhibits laser action in that region. The tunable operation prsented here spans only a fraction of the fluorescence spectrum, the part that is due to Cr^{4+} emission.

The experimental arrangement used to demonstrate wavelength tunability is shown schematically in Fig. 3.4.1. The sample (S) is placed at the center of a stable cavity formed by two 30-cm radius mirrors placed 45 cm apart. The input mirror (M_1) was dielectric coated to transmit the 1064-nm pump beam and to have high reflectivity of 99.9 % in the 1150 - 1250 nm range, which decreased to 98.5 % at 1270 nm. Three different mirrors were used as output couplers (M_2). The first mirror (output coupler A) had a reflectivity of 98 % for the 1200 - 1300-nm range, the reflectivity of the second mirror (output coupler B) varied from 99 % at 1150 nm to

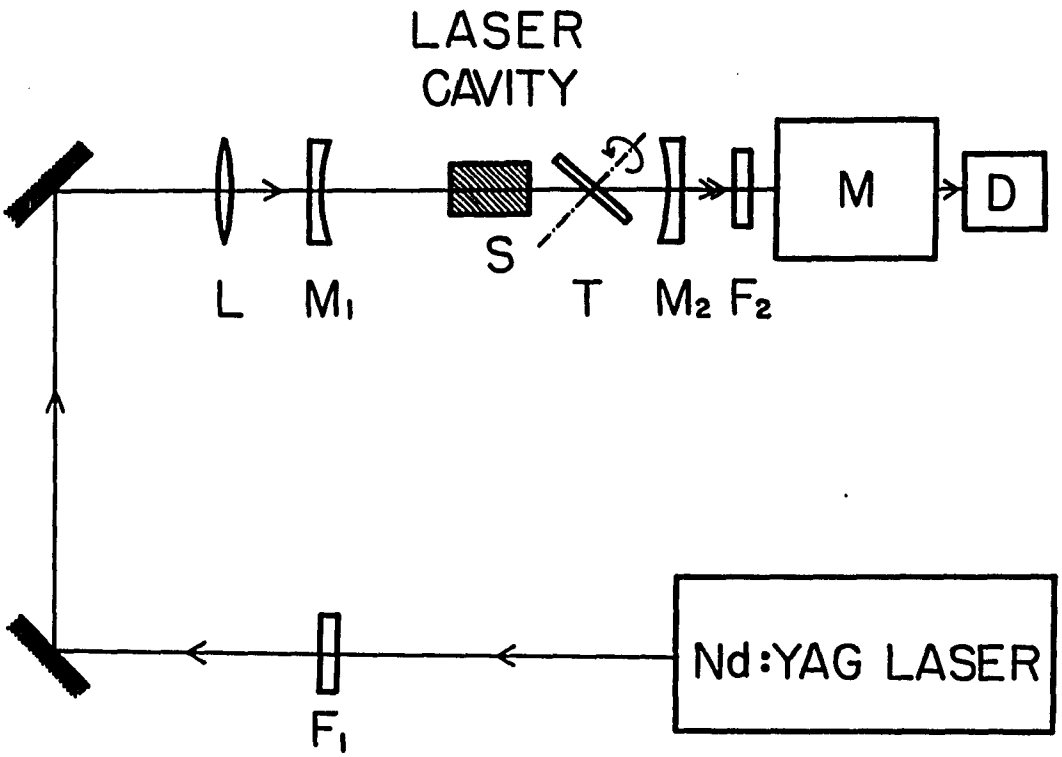

Figure 3.4.1 schematic diagram of the experimental arrangement used for wavelength tuning the Cr:Mg_2SiO_4 laser: F1 = 1064-nm transmitting, visible blocking filter; F2 = pump beam blocking, laser output transmitting filter; L = focusing lens, M1 = back mirror; M2 = output mirror; S = sample; T = birefringent plate tuning element; M = monochromator; and D = detector.

87 % at 1200 nm, while that of the third (output coupler C) varied from 99.8 % at 1150 nm to 90 % at 1200 nm. The left and center curves presented in Fig. 3.4.2 were taken with the first two of these output couplers. The tuning curve on the right was obtained with another pair of mirrors: the input mirror which had high transmission for the 1064-nm pump beam and reflectivity of 99.9 % in the 1275 - 1375-nm range and the output mirror (output coupler D), whose reflectivity varied from 96 % at 1275 nm to 94.5 % at 1375 nm with a maximum of 97 % at 1320 nm.

The dispersive element used for frequency tuning the Cr:forsterite laser output was a single birefringent crystalline quartz plate provided by Apollo Lasers, Inc. The plate was a 30 x 31.75 mm rectangle, 513.4 μm thick, with the optic axis in the plane and paralel to the 30-mm side. The plate was inserted in the cavity at the Brewster's angle with respect to the cavity axis, which is also the ray axis. The tuning of the laser output was effected by rotating the tilted plate about an axus perpendicular to its surface.

The first proof of wavelength tunability was that for four different output couplers, A, B, C, and D free-running laser outputs were centered at 1235, 1200, 1192, and 1250 nm, respectively.

With the birefringent plate inserted in the cavity, smooth tuning was obtained and the result is displayed in Fig. 3.4.2. The center curve taken with output coupler A shows the ratio of the output laser energy to the absorbed pump energy as a function of wavelength, spanning the 1205 -1268-nm spectral range. At the peak of this part of the tuning curve at 1220 nm, the output laser energy is ~7μJ/pulse for an input absorbed energy of 0.9 mJ/pulse.

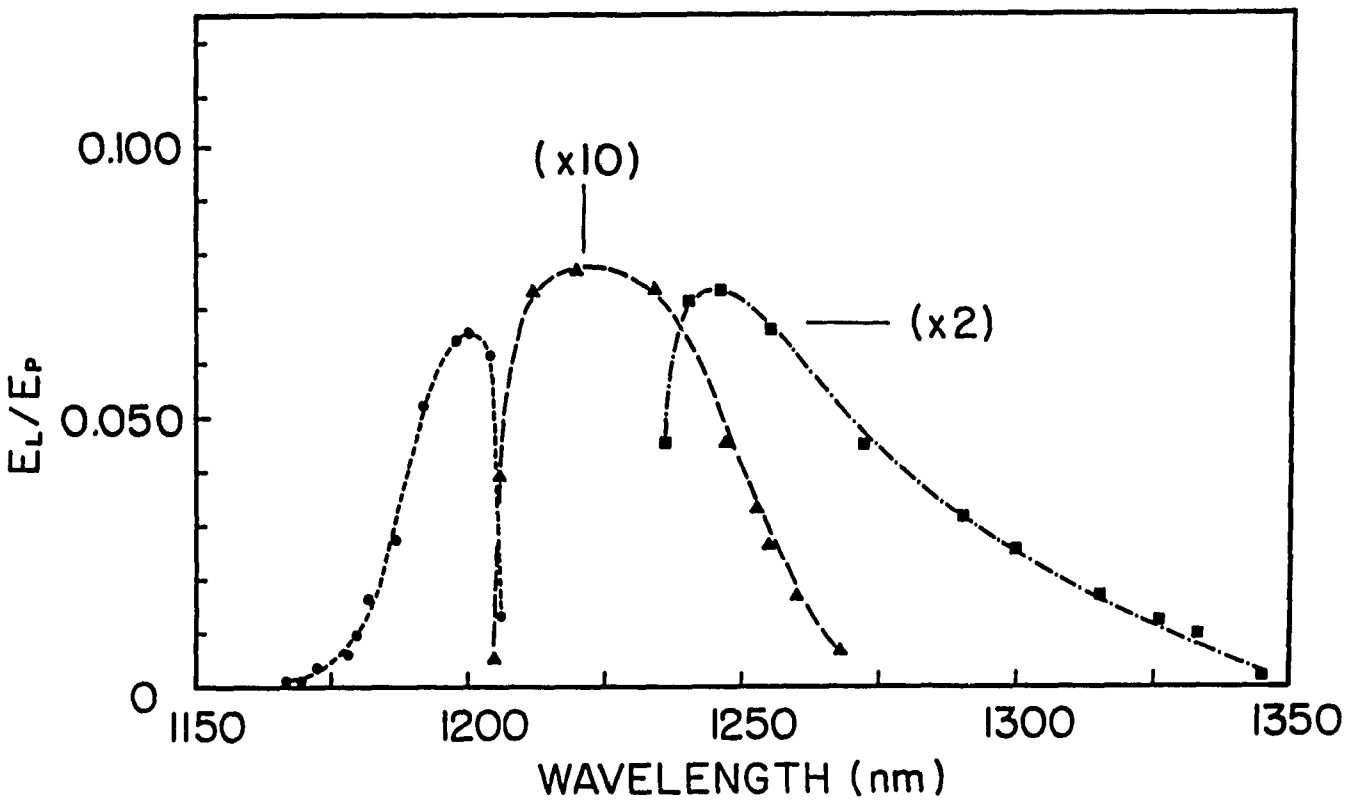

Figure 3.4.2 The ratio of $Cr:Mg_2SiO_4$ laser output (E_L) to the absorbed pump energy (E_P) as a function of wavelength. The three curves correspond to the three output couplers used in tuning measurements. The curve in the center was taken with output coupler A, The one to the left with output coupler B, and the curve to the right with a set of mirrors coated for the 1275 - 1375-nm range. The transmission characteristics of the mirrors and output couplers are described in the text.

The tuning curve on the left covering 1167 - 1206 nm was obtained with output coupler B described earlier. The laser output peaks at 1200 nm with an energy per pulse of 125 μJ for an absorbed input pulse energy of 1.9 mJ. This order of magnitude larger output power for this output coupler is attributed to its higher transmission (13 % at 1200 nm) compared with the output coupler A (<2 % over the tuning range). The free-running output slope efficiencies for the two output couplers, 23 % for coupler B compared to 5 % for coupler A, also reflect the same behavior. The lasing threshold of 0.38 mJ for output coupler B is a factor of ~2 higher than that for coupler A which is expected since the cavity with coupler B is lossier than the one with output coupler A, and is consistent with the respective output slope efficiencies.

The tuning curve on the right was obtained using a pair of mirrors coated for the 1275 - 1375-nm range. It covers the 1236 - 1345-nm wavelength region. The output peaks at 1245 nm with an energy per pulse of 85 μJ for an absorbed pump energy of 2.4 mJ. The free-running output slope efficiency for this pair of mirrors was 12 % with a lasing threshold of 0.27 mJ.

To summarize the results of the tuning experiment, continuously tunable operation of chromium-doped forsterite over the 1167 - 1345 nm spectral range has been demonstrated. At the peak of the tuning curve at 1200 nm an output of 125 mJ/pulse is obtained, with an output to absorbed input energy ratio of 6.6 %.

3.5 Continuous-Wave Laser Operation[8]

The experimental setup for investigating continuous-wave laser operation of $Cr:Mg_2SiO_4$ laser is shown in Fig. 3.5.1.

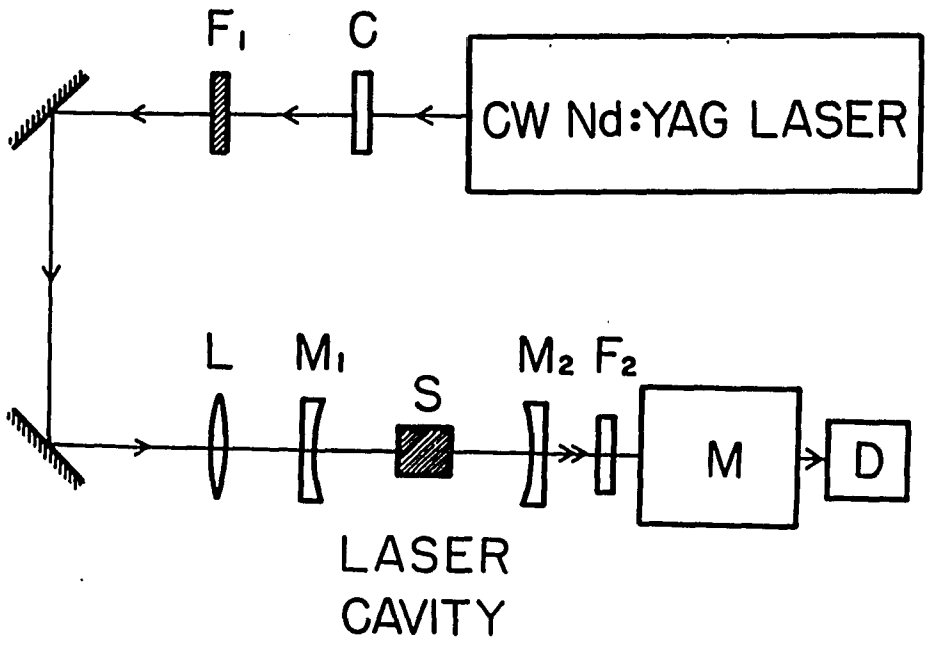

Figure 3.5.1 Schematic diagram of the experimental arrangement for investigating cw laser operation in Cr:forsterite: C, light chopper; F_1, variable neutral density filter; L, focusing lens; M_1, back mirror; M_2, output mirror; S, sample; F_2, 1064-nm cutoff, Cr:forsterite laser emission-transmitting filter; M, monochromator; D, germanium or PbS detector.

To obtain cw laser action a sample of chromium-doped forsterite (sample 1) was placed at the center of a nearly concentric cavity formed by two 5-cm radius-of-curvature mirrors such that a cavity mode waist was 75 μm. The output mirror was dielectric coated to have ~1% transmission for the 1175 - 1250 nm range, and to transmit most of the 1064-nm pump beam. The pump radiation from a cw Nd:YAG laser was focused by a 75-mm focal length lens to pump the sample longitudinally along the 30 mm path length. The pump beam was linearly polarized along the *b* axis and propagated along the *a* axis of the crystal. The beam was chopped at a duty factor of 9:1 to reduce heating effects. The waist of the pump beam at the center of the sample was measured to be 70 μm.

Quasi-cw laser operation was obtained for pumping above the lasing threshold of 1.25 W of absorbed power. Temporal behavior of the cw Cr:forsterite laser emission over the entire duration of the pump pulse is shown in Fig. 3.5.2. The measured slope efficiency was 6.8%. The cw output power of the Cr:forsterite laser as a function of absorbed pump power is displayed in Fig. 3.5.3. Laser operation was possible even when the pump beam was not chopped, but at 40% reduced output indicating losses induced by local heating.

The spectrum of the free-running laser output shown in Fig. 3.5.4 peaks at 1244 nm and has a bandwidth of 12 nm.

Using results obtained from CW lasing experiment several important parameters can be estimated. From an expression for the slope efficiency[13]

$$\eta = \lambda_P T/\lambda_L(L+T) \qquad (8)$$

where T is the total transmission of the cavity mirrors, L is the internal loss, and λ_P and λ_L are pump and lasing wavelengths, respectively, a value of 12.7% for L has

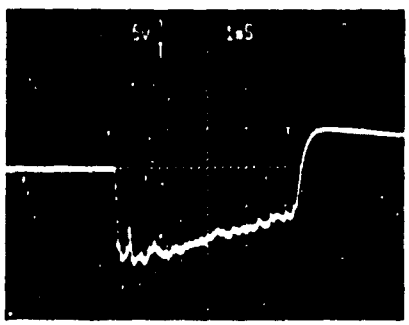

Figure 3.5.2 Temporal behavior of the cw Cr:forsterite laser emission over the entire duration of the pump pulse. (Time scale: 1 ms/division).

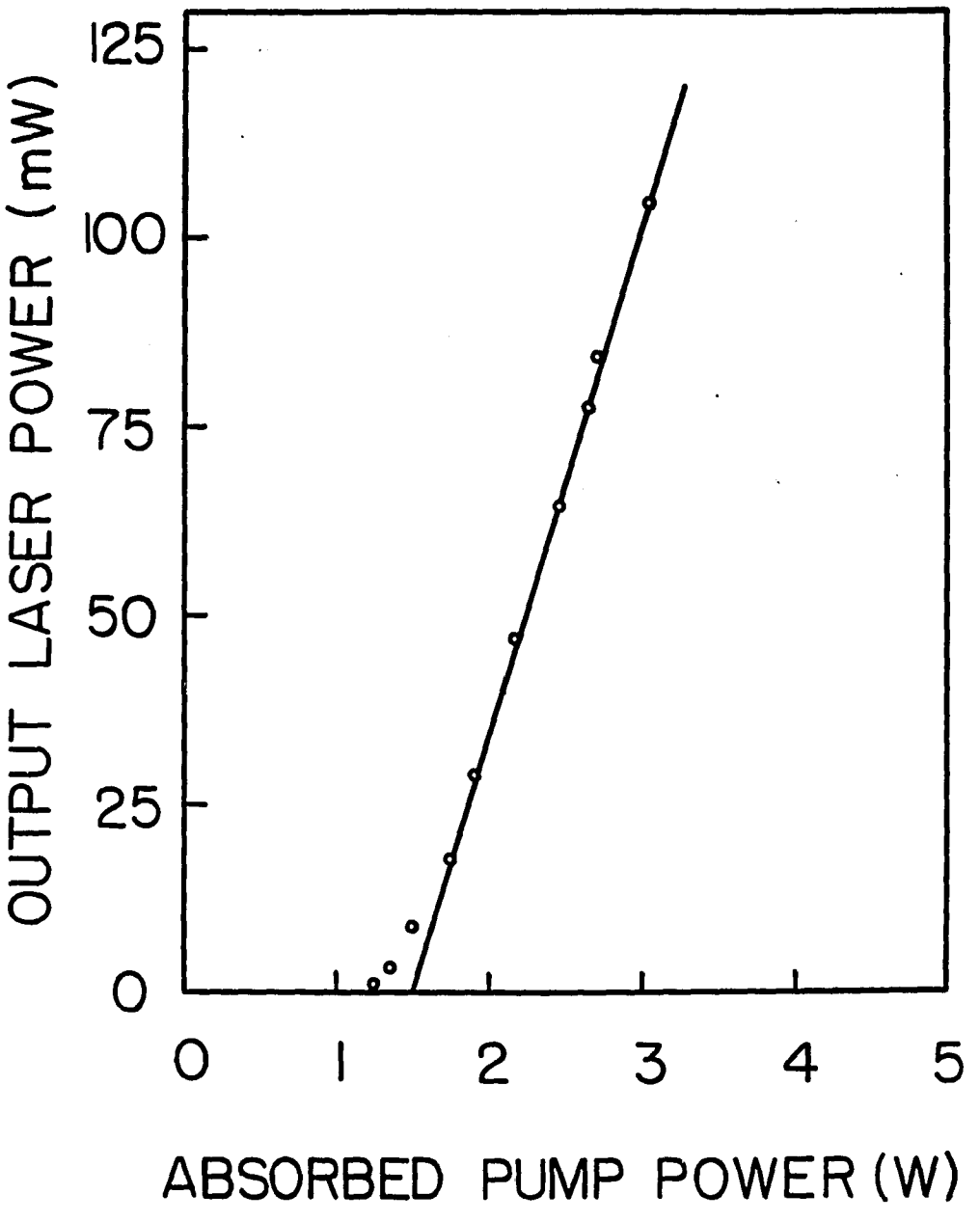

Figure 3.5.3 Output power of the cw $Cr:Mg_2SiO_4$ laser as a function of absorbed pump power.

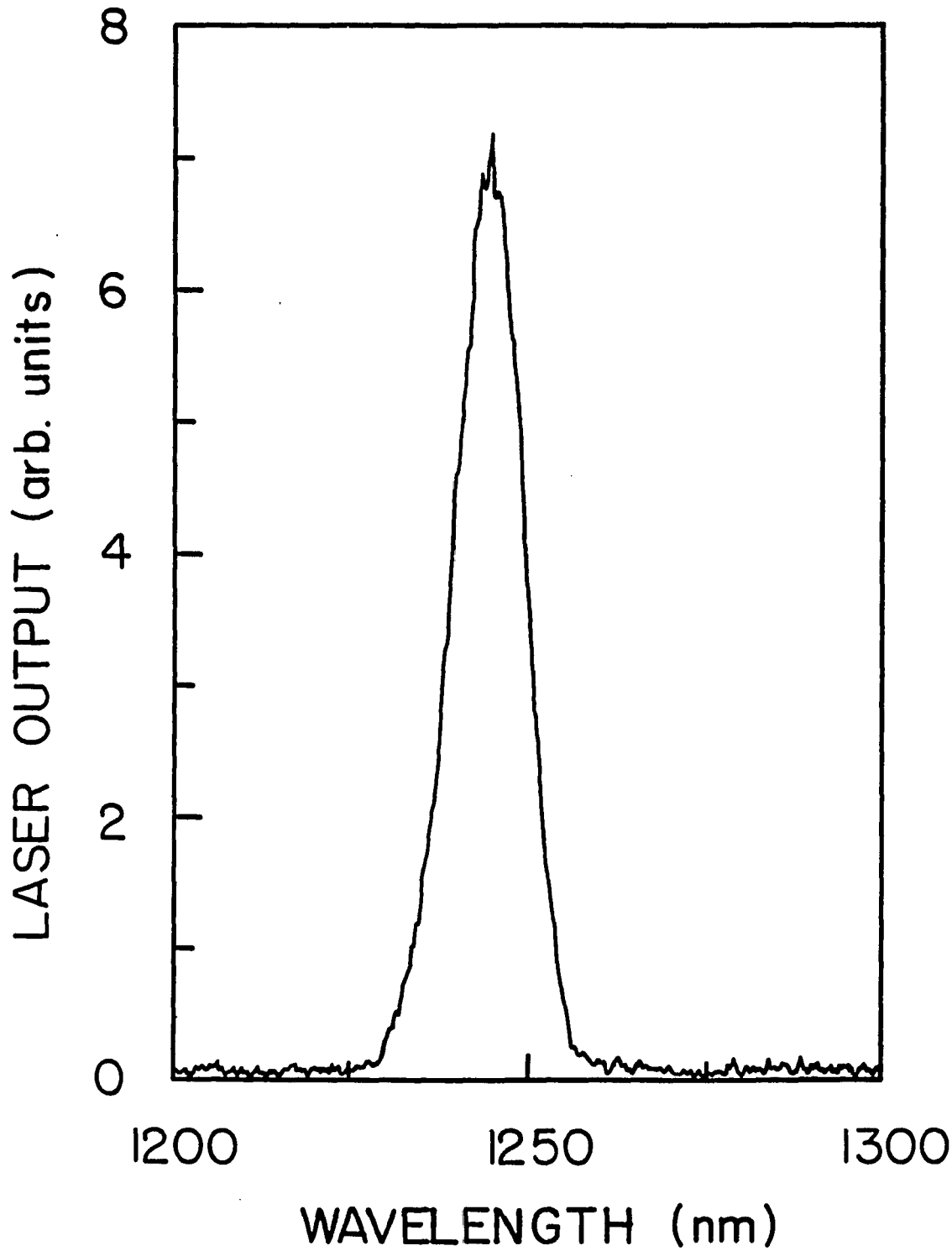

Figure 3.5.4 Spectrum of the free-running cw Cr:forsterite laser.

been estimated. This value is in reasonable agreement with the value of 11% obtained from pulsed measurements.

An expression similar to Eq. (7)

$$P_{th}=\frac{\pi h\nu_p \omega_L^2 (L+T)(a^2+1)}{4\sigma\tau\left[1-\exp(-\alpha l)\right]} \qquad (9)$$

where P_{th} is the incident threshold pump power, was used to calculate the gain cross section from the CW measurements. A value of 1.47×10^{-19} cm^2 was obtained, in excellent agreement with the one obtained from pulsed laser experiments. Both values should be compared to the peak value for the stimulated emission cross section of 2.11×10^{-19} cm^2 obtained from radiative lifetime and lineshape measurements. The discrepancy can arise from another loss mechanism such as excited state absorption.

From the gain cross section and threshold pump power, the threshold population inversion density was estimated using the threshold condition:[14]

$$2\sigma N_{th} l = L+T \qquad (10)$$

A value of 1.6×10^{17} cm^{-3} for the population inversion was calculated.

The key continuous-wave laser parameters are summarized in Table 3.5.1.

TABLE 3.5.1 : Properties of cw Laser Operation of $Cr:Mg_2SiO_4$ Laser

Property	Value
Lasing Wavelength	1244 nm
Spectral Bandwidth (FWHM)	12 nm
Lasing Threshold (Absorbed Power)	1.25 W
Slope Efficiency	6.8%
Threshold Inversion Density	1.6×10^{17} cm^{-3}
Gain Cross Section	1.47×10^{-19} cm^2

3.6. Limiting Slope Efficiency Measurements

The highest slope efficiency of the Cr:forsterite laser was measured to be 23%. (See Fig. 3.3.1). However, this may not be the highest slope efficiency that can be achieved. When the inverse slope efficiency is plotted as a function of the inverse output coupling factor, (when different output mirrors are used), the limiting slope efficiency η_o, which can be achieved in the absence of passive losses, can be determined. In this section, we follow the approach of Caird et al.[14] to determine η_o and estimate the role of various loss mechanisms on laser performance of the Cr: forsterite laser.

The equation (8) of Section 3.5 which gives the slope efficiency as afunction of the output copling parameter T and loss L, originally derived by Danielmeyer,[13] was modified by Caird et al.[14] to include a loss factor due to excited-state absorption:

$$\eta_s = \lambda_P T/\lambda_L(L+T+ 2\sigma_{ESA}N_E\ell) \qquad (1)$$

where σ_{ESA} is the excited state absorption cross section, N_E is the excited state density, and ℓ is the crystal thickness. Similarly, the threshold gain condition given by the equation (10) of Section 3.5 can be changed to

$$2(\sigma_E - \sigma_{ESA})N_E\ell = T + L \qquad (2)$$

where σ_E is the stimulated emission cross section.

Combining equations (1) and (2) one obtains

$$\eta_s = (\lambda_P/\lambda_L)[(\sigma_E - \sigma_{ESA})/\sigma_E)][T/(L+T)]. \qquad (3)$$

We can define the effective gain cross section as

$$\sigma_{EFF} = \sigma_E - \sigma_{ESA} \quad (4)$$

Equation (3) can now be rewritten as

$$\eta_s = (\lambda_P/\lambda_L)(\sigma_{EFF}/\sigma_E)[T/(L+T)] = \eta_o[T/(L+T)] \quad (5)$$

It is obvious from the equation (5) that in order to achieve the quantum defect limited value of the slope efficiency λ_P/λ_L excited state absorption cross section σ_{ESA} must be negligible.

The inverse output power slope efficiency $1/\eta_s$ and the inverse of the limiting slope efficiency $1/\eta_o$ are connected by a linear relationship:

$$1/\eta_s = 1/\eta_o(1+LT^{-1}), \quad (6)$$

where

$$\eta_o = (\lambda_P/\lambda_L)(\sigma_{EFF}/\sigma_E) \quad (7)$$

Therefore, if passive losses L and output coupling factor T can be determined acurately, the value of η_o obtained by extrapolating the inverse slope efficiency as a function of the inverse output coupling can be used to estimate the excited state absorption cross section, i.e. the deviation of the effective gain cross section from the stimulated emission cross section predicted by the lineshape and the lifetime measurements.

The limiting slope efficiency of the Cr:Mg_2SiO_4 laser was measured using a standard 3-mirror astigmatically compensated cavity.[15] The experimental setup is shown in Fig. 3.6.1. Output coupling factor T was varied by changing the flat output mirror. Four different output couplers with transmission of ~1%, ~5 %, ~10 %, and ~15 % over the 1200 - 1300 nm spectral range were used.

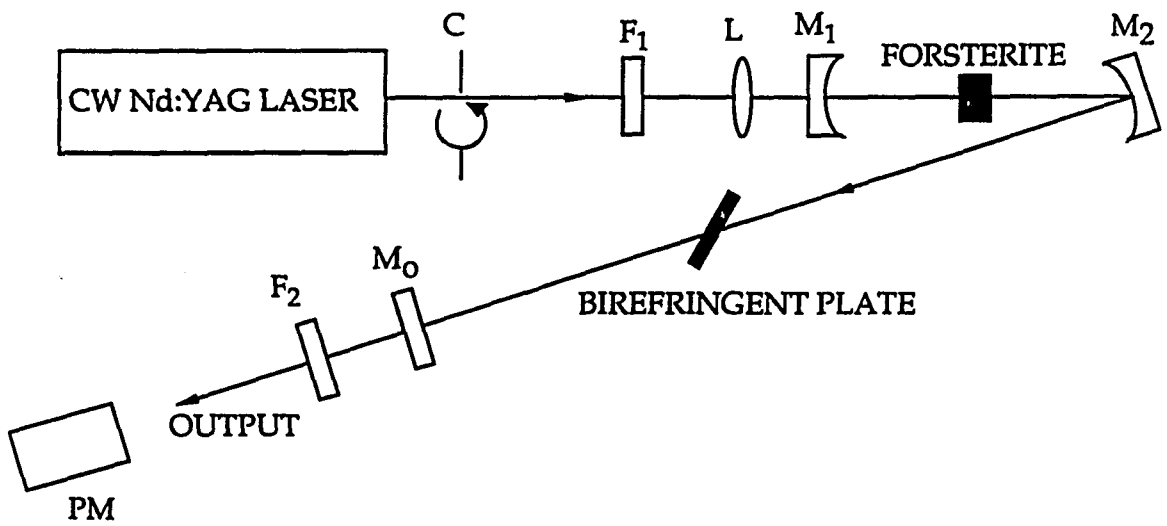

Figure 3.6.1 Schematic diagram of the experimental arrangement for measuring the limiting slope efficiency of Cr:forsterite laser: C, light chopper; F_1, variable neutral density filter; L, focusing lens; M_1, 5-cm radius back mirror; M_2, 10-cm radius folding mirror; M_O, output mirror; S, sample; T, birefingent tuning plate; F_2, 1064-nm cutoff filter, Cr:forsterite laser emission-transmitting filter; PM, power meter.

The chromium-doped forsterite crystal (sample 1) was pumped longitudinally with 1064-nm radiation from a cw Nd:YAG laser. The pump beam was linearly polarized along the *b* axis and propagated along the *a* axis of the crystal. The position of the 7.5-cm-focal-length lens was adjusted for the best overlap of the pump beam and the cavity mode by monitoring the output power. The pump beam was chopped at a duty cycle of 15:1 to reduce thermal effects.

The experimental results are summarized in Table 3.6.1. The inverse slope efficiency as a function of output coupling is shown in Fig. 3.6.2. The inverse slope efficiency extrapolates to a limiting slope efficiency of η_o = ~65 %. Using equation (7) we calculate

$$\sigma_{ESA} = (1 - \eta_o\lambda_L/\lambda_P)\sigma_E = 0.23\sigma_E$$

i.e. the excited state absorption cross section is much smaller than the stimulated emission cross section and therefore does not represent a major loss mechanism in chromium-doped forsterite.

TABLE 3.6.1: Slope Efficiency of cw $Cr:Mg_2SiO_4$ Laser for Various Output Couplers

Output Mirror Transmission [%]	Slope Efficiency [%]	Output Wavelength [nm]
0.65	5.69	1260
3.4	24.65	1258
7.8	31.76	1265
11	37.85	1242

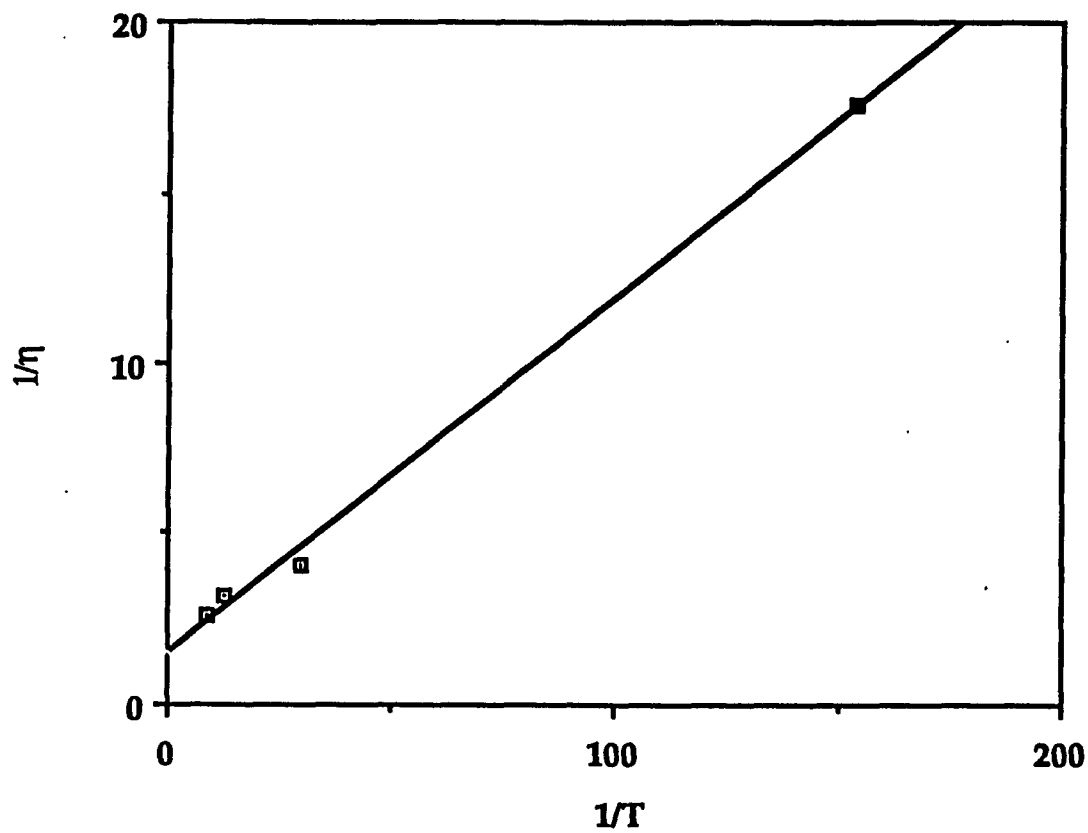

Figure 3.6.2 Inverse slope efficiency $1/\eta_s$ as a function of inverse output coupling 1/T for cw Nd:YAG-pumped continuous-wave Cr:Mg_2SiO_4Laser. Extrapolating the data limiting slope efficiency of η_o >65 % is obtained.

3.7 References

1. N. Nishide, Y. Segawa, P. H. Kim, S. Namba, and A. Masuyama, Reza Kagaku Kenkyu **7**, 89 (1985).

2. K. Yamagishi, H. Shimizu, K. Moriya, T. Saito, Y. Segawa, H. Kin, S. Namba, Jpn. Kokai Tokkyo Koho JP 61,240,692 [86,240,692] (Cl. H01S3/16), 25 Oct 1986, Appl. 85/81397, 18 Apr 1985.

3. B. H. T. Chai and R. C. Morris, private communication.

4. H. R. Verdun, private communication.

5. V. Petričević, S. K. Gayen, R. R. Alfano, K. Yamagishi, H. Anzai, and Y. Yamaguchi, Appl. Phys. Lett. **52**, 1040 (1988).

6. V. Petričević, S. K. Gayen, and R. R. Alfano, Appl. Opt. **27**, 4162 (1988).

7. V. Petričević, S. K. Gayen, and R. R. Alfano, Appl. Phys. Lett. **53**, 2590 (1988).

8. V. Petričević, S. K. Gayen, and R. R. Alfano, Opt. Lett. **14**, 612 (1989).

9. V. Petričević, S. K. Gayen, and R. R. Alfano, Appl. Opt. **28**, 1609 (1989).

10. V. Petričević, S. K. Gayen, and R. R. Alfano, in *Tunable Solid-State Lasers*, Vol. 5 of the OSA Proceeding Series, M. L. Shand and H. P. Jenssen, eds. (Optical Society of America, Washington, D.C., 1989), pp. 77-84.

11. P. F. Moulton, J. Opt. Soc. Am. B, **3**, 125 (1986).

12. P. F. Moulton, IEEE J. Quantum Electron. **QE-21**, 1582 (1985).

13. H. G. Danielmeyer, in *Lasers*, A. K. Levine and A. De Maria, eds. (Dekker, New York, 1975), Vol. IV.

14. J. A. Caird, S. A. Payne, P. R. Staver, A. J. Ramponi, L. L. Chase, and W. F. Krupke, IEEE J. Quantum Electron. 24, 1077 (1988).

15. H. W. Kogelnik, E. P. Ippen, A. Dienes, and C. V. Shank, IEEE J. Quantum Electron. QE-8, 373 (1972).

CHAPTER 4

PUMP-AND-PROBE MEASUREMENTS OF THE EFFECTIVE GAIN CROSS SECTION IN CHROMIUM-DOPED FORSTERITE

4.1. Introduction

As shown in Chapters 2 and 3 chromium-doped forsterite ($Cr:Mg_2SiO_4$) is an important tunable solid-state laser system for the near infrared spectral range. It has been operated in both pulsed[1-3] and continuous-wave[4] mode of operation, as shown in Chapter 3. Its output can be tuned over the 1167-1345 nm range.[5] The most interesting feature that distinguishes this laser system from other chromium-based lasers is that the lasing ion is tetravalent chromium (Cr^{4+}) in a tetrahedrally coordinated site, as shown in Chapter 2.[2,3,6-8] While the spectroscopic properties of chromium-doped forsterite have been studied in some detail,[6-8] the evaluation of the potentials of this crystal for application as a practical laser system is near completion. In this chapter, pump-and-probe measurements of the effective gain cross-section in chromium-doped forsterite are presented. Results of these measurements are used to evaluate the effect of the excited-state absorption (ESA) on the performance of chromium-doped forsterite as a laser crystal.

The most important parameter that characterizes a laser system is the gain cross-section. The gain cross-section can be estimated using the Einstein relation which gives gain as a function of the radiative lifetime and fluorescence lineshape. The gain (or stimulated emission) cross section σ_E is given by[9]

$$\sigma_E(\nu) = (\lambda_0^2/8\pi n^2 \tau) g(\nu,\nu_0) \qquad (1)$$

where λ_0 is the wavelength of the peak of the emission line, n is the index of refraction of the host crystal, τ is the spontaneous emission radiative lifetime, $g(\nu,\nu_0)$ is the normalized lineshape function obtained from the emission spectrum, ν_0 is the center frequency, and ν is frequency. Expression (1) implies that the stimulated emission cross section should have the same frequency (or wavelength) dependence as the fluorescence (spontaneous emission) intensity, i. e. the gain cross section curve should follow the fluorescence curve.

However, very often there is a discrepancy between the values predicted by the relation (1) and the values observed in laser experiments. Lower values of the gain cross section measured in laser experiments are in many cases explained by the existence of loss mechanisms such as excited-state absorption. The net or effective gain cross section is then given by

$$\sigma_{EFF} = \sigma_E - \sigma_{ESA} \qquad (2)$$

where σ_E is the gain cross section, which can be calculated using the Einstein relation and σ_{ESA} is the excited-state absorption cross section.

ESA is a loss mechanism which impedes or, in some cases, completely inhibits laser action in tunable solid-state laser materials. It has been shown that it severely affects laser performance of V^{2+}-doped crystals,[10,11] prevents laser action in Mn^{2+}-doped crystals,[12] and limits the slope efficiency of Cr^{3+}:$Mg_3Ga_2Li_3F_{12}$ laser.[13] It is also present, although without such a detrimental effect, in well developed tunable solid-state lasers such as alexandrite.[14] Absence of ESA is one of the most important advantages of Ti:Al_2O_3 laser.[15]

Measurements of the limiting slope efficiency, described in Chapter 3, indicate that background absorption and scattering losses are major loss mechanisms present in chromium-doped forsterite laser crystals. This was shown by good agreement between the values of the passive loss estimated from laser experiments and the background absorption measured with a spectrophotometer. Role of the ESA was estimated to be minimal.

In the following sections, we present measurements of the effective gain cross-section in $Cr:Mg_2SiO_4$ over the part of its tuning range. These measurements were undertaken as an attempt to estimate the effect of ESA on laser performance of chromium-doped forsterite laser.

4.2. Experimental Methods

The $Cr:Mg_2SiO_4$ sample used in this study is a 38 mm long and 4 mm in diameter single-crystal laser rod with end facets anti-reflection coated for the 1.1-1.4 μm spectral range. The crystal was grown by Czochralski technique at the Electronic Materials Research Laboratory of the Mitsui Mining and Smelting Co., Ltd., Japan. The total chromium ion concentration in the crystal is ~5 x 10^{18} cm^{-3}. The crystal contains both Cr^{3+} and Cr^{4+} ions with the relative concentration of Cr^{3+} and Cr^{4+} ions unknown. The Cr^{4+} concentration was increased by growing the crystal in more oxidizing atmosphere (~1 % oxygen partial pressure). The ground-state absorption spectrum of $Cr:Mg_2SiO_4$ for E || b axis is shown in Fig. 4.2.1. The spectrum shows contributions from both the active ions, Cr^{3+} and Cr^{4+}. The transition assignments in Fig. 4.2.1 were made[6,9] using Tanabe-Sugano diagrams for Cr^{3+} ions in octahedral coordination and Cr^{4+} in tetrahedral coordination.

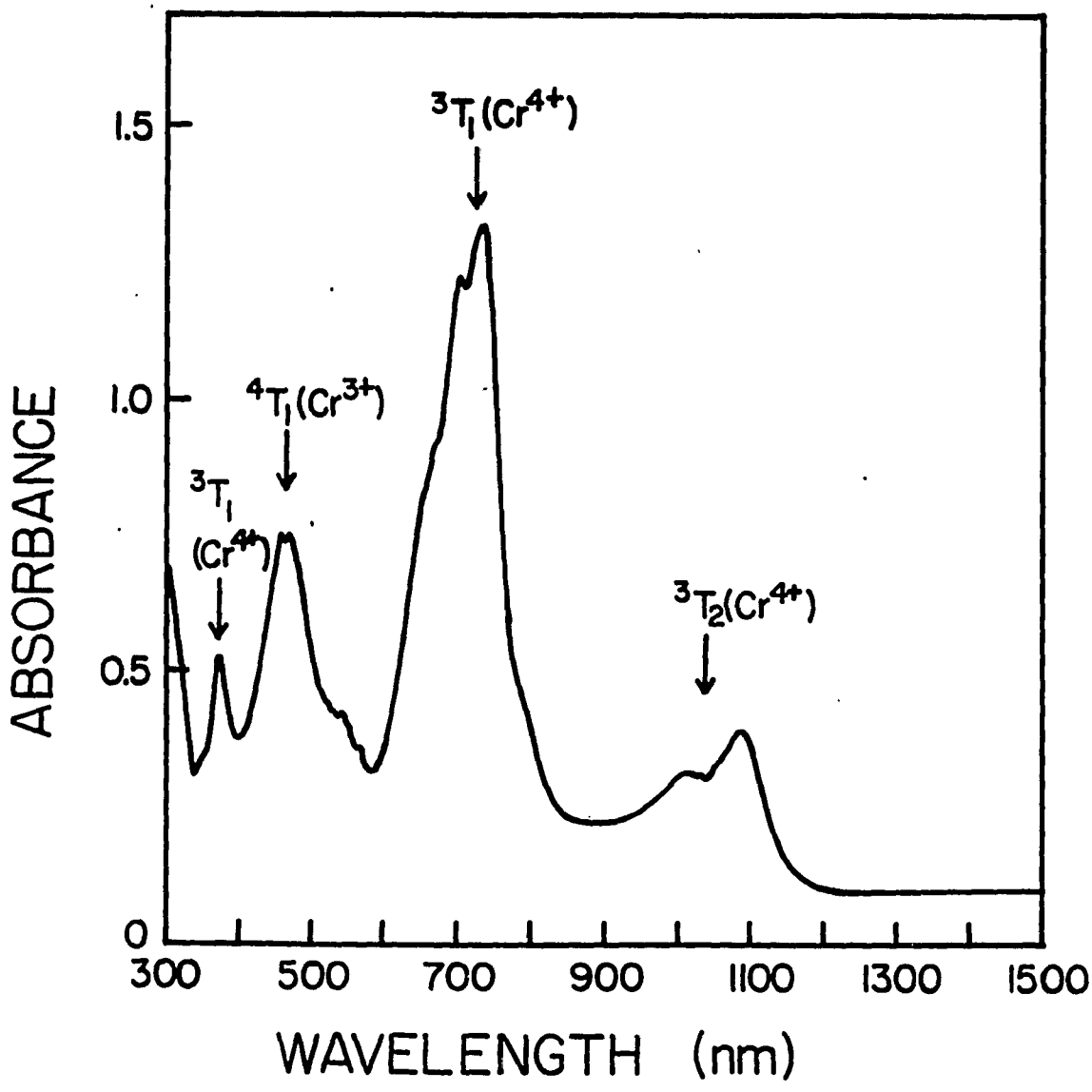

Figure 4.2.1. Room temperature absorption spectrum of Cr:Mg_2SiO_4 for E | | b axis.

The effective gain measurements were performed using standard pump-and-probe arrangement. As a pump source the fundamental 1064-nm radiation from a pulsed Nd:YAG laser was used to selectively populate only the $^3T_2$ state of the Cr^{4+} ion, the upper lasing level of the chromium-doped forsterite laser. The choice of a probe beam source depends on the wavelength range that is being investigated. In the wavelength region where the emission is too intense, i.e. in the tuning range of the laser crystal under investigation, tungsten or xenon lamps cannot be used, since the fluorescence from the sample overwhelms the probe beam.[10,11] Therefore, we decided to use laser as a probe source. A tunable Cr:forsterite laser appeared to be an ideal probe beam source for this measurement.

The experimental setup used to measure the effective gain cross-section is shown schematically in Fig. 4.2.2. The $^3T_2$ state of the Cr^{4+} ion was populated by 1064-nm pump beam obtained from a Q-switched Nd:YAG laser operating at 10 Hz repetition rate. The pump beam was weakly focused to a 400-μm radius spot on the sample by a 1-m focal length lens. Typical pump beam energy incident on the sample was ~1 mJ per pulse, of which 79 % was absorbed in the sample. The excited state was probed by a collinearly propagating probe beam. The weak probe beam (typically ~25 μJ per pulse) was obtained from a tunable Cr:forsterite laser pumped by the same Nd:YAG laser used to pump the sample. Wavelength tuning of the probe beam was accomplished by using a birefringent plate at Brewster's angle as an intracavity dispersive element and by changing the output mirror.[5] The delay between the pump pulse and the probe pulse was smaller than 100 ns. Since the room temperature lifetime of the $^3T_2$ state in chromium-doped forsterite is 2.7 μs, no appreciable depopulation of the excited state takes place before the arrival of the probe pulse. Probe beam was focused on the sample by 30-cm focal length lens to a 150-μm radius spot. The pump and probe beams were carefully overlapped in the

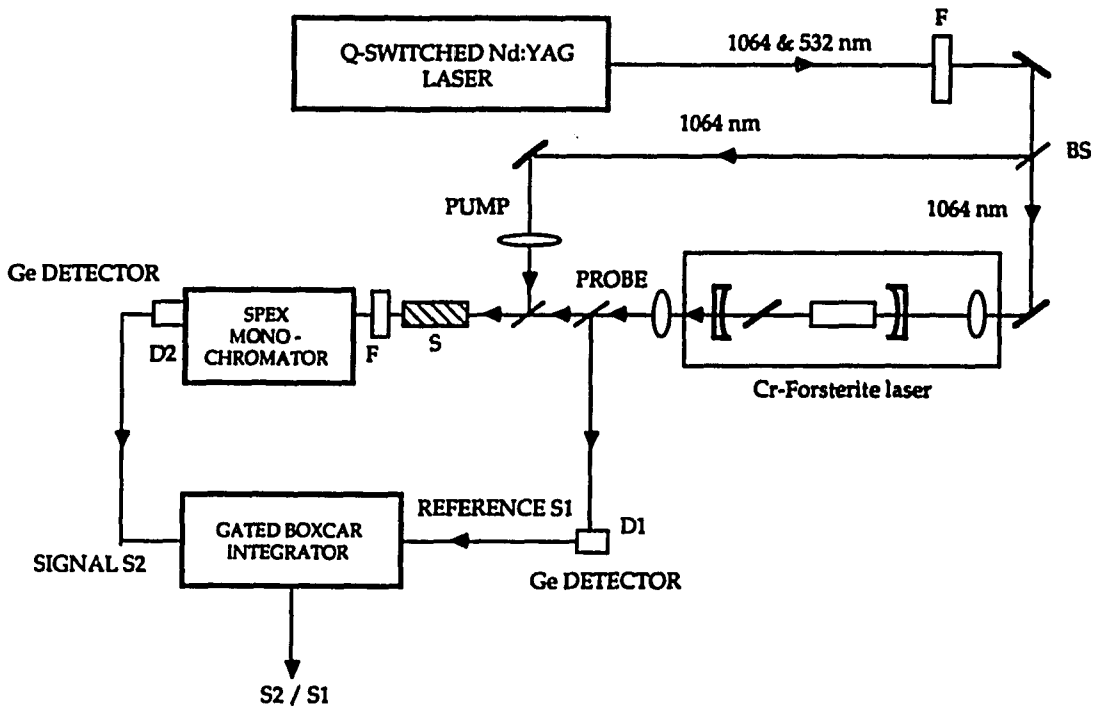

Figure 4.2.2. Experimental setup used to measure the effective gain cross-section in chromium-doped forsterite.

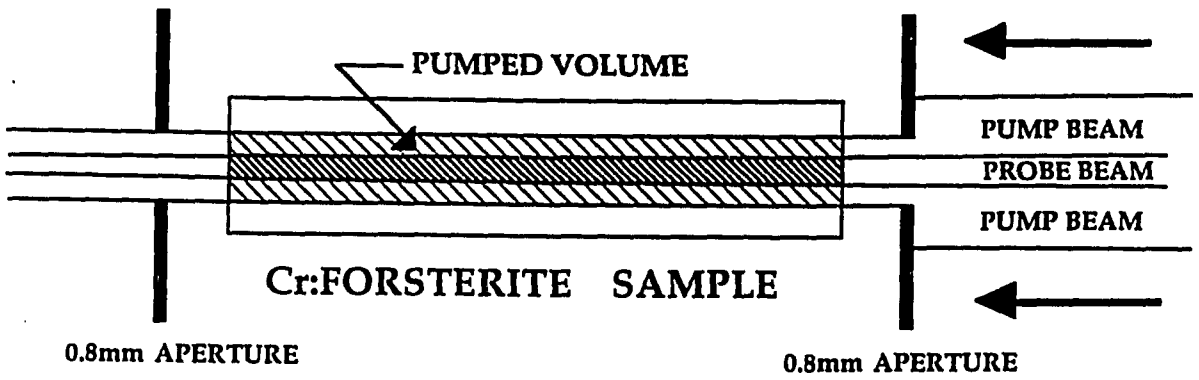

Figure 4.2.3 Overlap of the pump and probe beams in the sample.

sample using two 0.8-mm apertures so that the probe beam was fully concentric within the pump-beam. The overlap of the two beams was checked by scanning a razor blade mounted on a translation stage across the beam in both vertical and horizontal directions, before and behind the sample. Details of the overlap of the pump and probe beams in the sample and typical beams profiles are shown in Fig. 4.2.3.

The effective gain cross section was estimated from the ratio of the transmitted probe intensity for the pumped and unpumped conditions of the sample, respectively. The transmitted probe intensity was normalized with respect to probe intensity before the sample to account for the pulse-to-pulse energy fluctuations. The probe beam intensity before the sample was monitored with a beam splitter and a fast germanium photodiode D_1. The transmitted probe beam was analyzed by a 1/4-meter spectrometer and its intensity was monitored by an identical germanium photodiode D_2. A gated boxcar integrator was used to obtain the average ratio S_2/S_1, where S_2 is the signal proportional to the intensity of the transmitted probe beam measured by a germanium detector D_2 at the end of the spectrometer, and S_1 is proportional to the intensity of the probe beam before the sample measured by a germanium detector D_1. The average was taken over 100 laser shots to enhance the signal-to-noise ratio.

Excited-state population density (N_E) was estimated by measuring the pumped volume of the sample and the energy of the pump pulse absorbed in the crystal, assuming that each absorbed pump photon creates one excited ion. The pumped volume of the crystal was estimated by measuring the size of the pump beam at the position of the sample. Since the pump beam was weakly focused with a long focal-length lens and a 0.8 mm aperture was used in front of the sample, the transverse

beam intensity distribution was measured to be approximately uniform, with the beam radius of 0.4 mm throughout the crystal.

4.3. Experimental Results

The normalized probe transmission S_2/S_1 was used to determine the value of the effective gain cross-section in chromium-doped forsterite. It has been shown[18,19] that the effective gain cross section σ_{EFF} can be calculated using the expression

$$\sigma_{EFF} = \sigma_E - \sigma_{ESA} + \sigma_G = -(1/N_E\ell)\ln R, \qquad (3)$$

where σ_E is the gain cross section, σ_{ESA} is the excited-state absorption cross section, σ_G is the ground state absorption cross section at probe wavelength, N_E is the excited-state population density of , ℓ is the length of the crystal and R is defined by

$$R = (S_2/S_1)_u/(S_2/S_1)_p. \qquad (4)$$

The subscripts u and p refer to unpumped and pumped cases, respectively.

The measured effective (net) gain cross section as a function of wavelength in the 1180-1330 nm wavelength region is presented in Fig. 4.3.1 by triangles superimposed on the fluorescence spectrum. The near-infrared portion of the absorption spectrum is also displayed for comparison.

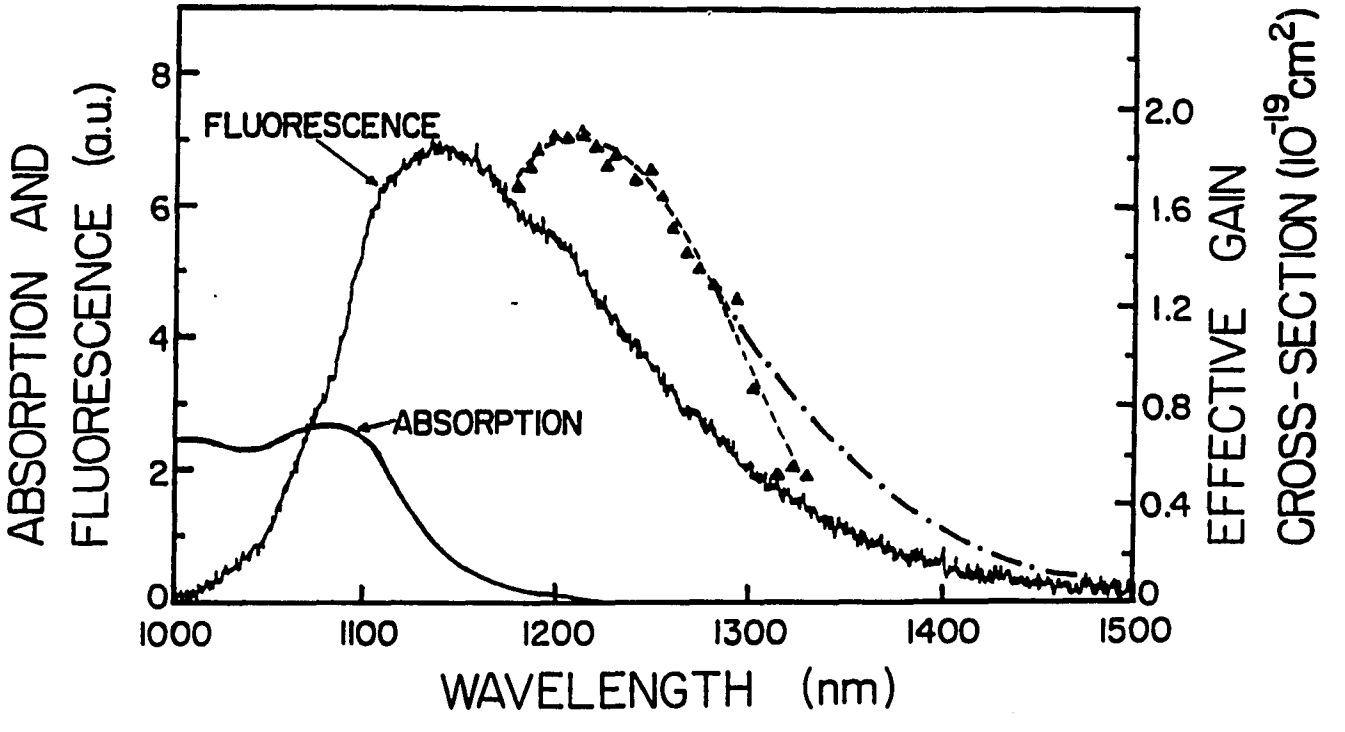

Figure 4.3.1 The Fluorescence spectrum for 1064-nm excitation and the infrared absorption spectrum of chromium-doped forsterite (solid line) and the effective gain cross-section (triangles and broken line). Dot-dash curve shows the expected gain in case there is no ESA.

4.4. Discussion

In Cr-doped forsterite the laser-active ion is tetrahedrally coordinated tetravalent chromium, Cr^{4+} and therefore the possible transitions that may affect laser operation occur between different states of the Cr^{4+} ion.

For near-infrared pumping (e.g. 1064-nm radiation from Nd:YAG laser) only the $^3A_2 \rightarrow {}^3T_2$ transition between the ground state and the first excited state of the Cr^{4+} ion takes place, that is only Cr^{4+} ions are being excited. The ESA transitions are then expected to originate from the relaxed $^3T_2$ state of the Cr^{4+} ion. From the Tanabe-Sugano diagram for tetravalent chromium in $Cr:Mg_2SiO_4$, shown in Fig. 4.4.1, it is possible to predict the wavelength of the peak of the ESA. Using Dq=~880 cm^{-1} and B=970 cm^{-1} for the relaxed $^3T_2$ state, a maximum of ESA due to $^3T_2 \rightarrow {}^3T_1$ transition may be expected at ~1710 nm. (See Appendix 4.6.3.)

It has been suggested[16,17] that the same $^3T_2 \rightarrow {}^3T_1$ transition may be responsible for limited tuning range of the Cr:YAG laser, besides Cr:forsterite the only other successful Cr^{4+}-based laser system, to date. The same process may be the reason that laser experiments in Cr^{4+}-doped garnets such as GSGG, GSAG and YSGG were unsuccessful so far.

The salient features of the gain curve obtained from the pump-and-probe measurements shown in Fig. 4.3.1 are the peak value of 1.9×10^{-19} cm^2 at 1215 nm and the shape of the curve. The shift of the peak of the gain curve with respect to the peak of the fluorescence curve in Fig. 4.3.1 is a consequence of the overlap of the fluorescence band with the low energy tail of the absorption band. The shape of the gain curve, which is expected to follow the fluorescence curve according to (1), deviates slightly from it in the wavelength range beyond 1300 nm as shown by a

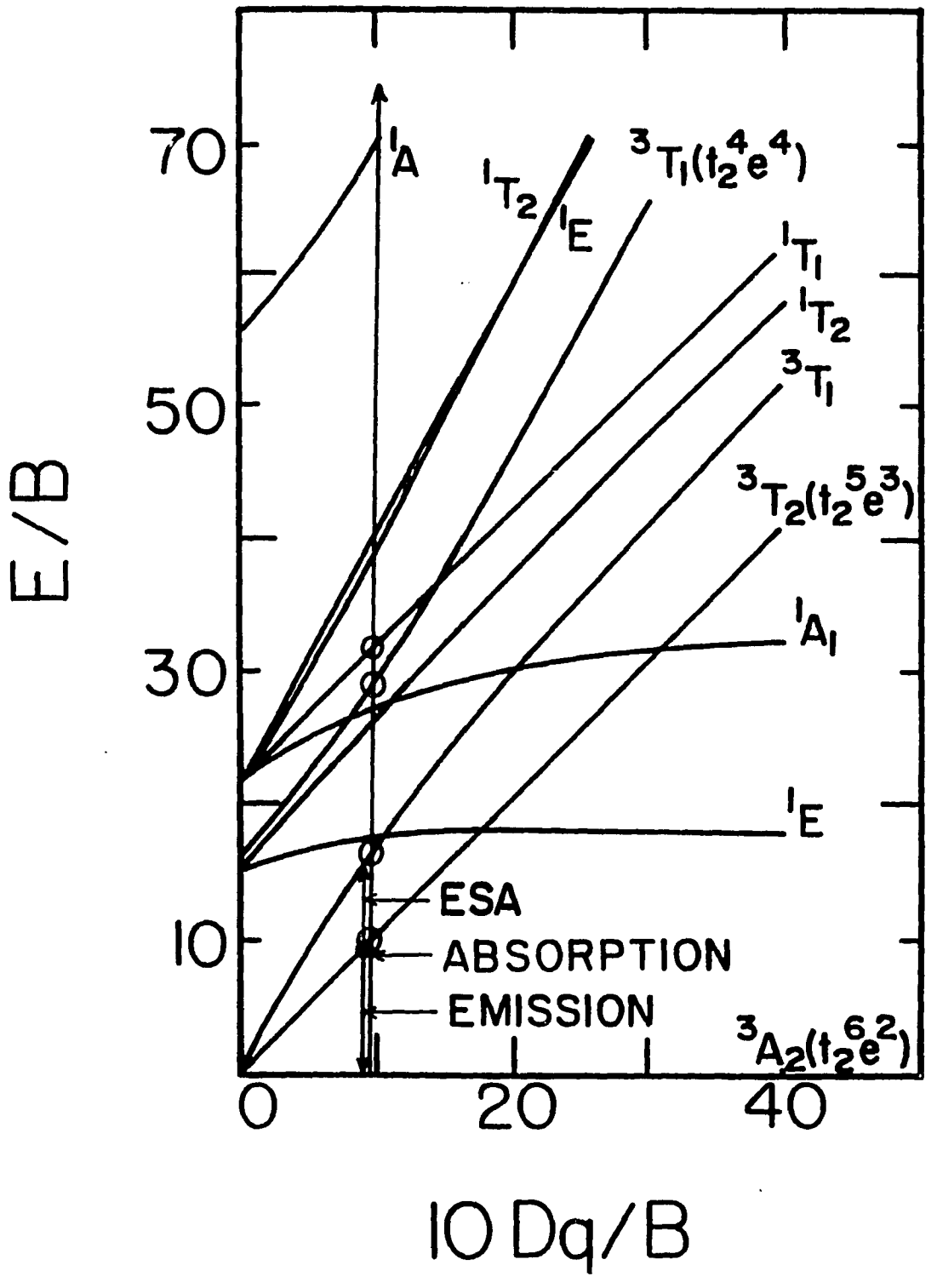

Figure 4.4.1 Tanabe-Sugano diagram for Cr^{4+} in tetrahedral coordination. Crystal field parameter Dq=915 cm^{-1} and Raccah parametr B=970 cm^{-1}. The possible $^3T_2 \rightarrow {}^3T_1$ excited-state absorption is indicated by an arrow.

dot-dash curve. The higher than expected decrease of the gain in this range most likely arises from the onset of the ESA. This is in agreement with the predicted wavelength of ESA approaching 1670 nm. (See Section 4.6.3) This is also in accordance with the suggested ESA in Cr:YAG and Cr: GSGG.

The results of the pump-and-probe experiment show that in the case of chromium-doped forsterite the role of ESA is not so prominent in the bigger portion of the tuning range. The measured values of the net gain cross section are in good agreement with the value of ~2.11 x 10^{-19} cm^2 for the peak gain cross section calculated using modifed equation (1). (See Section 4.6.2 of the Appendices.) In this calculation we used experimental results from the radiative lifetime and fluorescence lineshape measurements. These values are also in excellent agreement with the gain cross-sections obtained from both pulsed and continuous-wave laser experiments. The gain cross sections estimated from different measurements are summarized in Table 4.4.1.

TABLE 4.4.1: Estimates of Gain Cross Section From Different Measurements

Experiment	λ (nm)	σ (cm^2)
Linewidth and Lifetime Measurements	1140	2.11×10^{-19} (calculated)
CW Laser Operation	1244	1.47×10^{-19}
Pulsed Laser Operation	1235	1.44×10^{-19}
Pump-and-probe Experiment	1200	1.8×10^{-19}

4.5. Conclusions

The effective gain cross-section in chromium-doped forsterite laser crystal has been measured over the 1180-1330 nm spectral range. The close agreement between the measured effective gain cross section and the peak gain cross-section predicted using radiative lifetime and fluorescence linewidth indicates that ESA cross section is considerably smaller than the gain cross section. This agreement implies that ESA is not a major loss mechanism in chromium-doped forsterite for wavelengths shorter than 1300 nm. There is a possibility of the onset of a weak ESA occuring beyond 1300 nm.

4.6 Appendices

4.6.1 Pump and Probe Experiment Analysis Method

In the pump-and-probe experiment the absorption coefficient for the probe beam depends on the concentration of excited ions. The concentration of excited ions is proportional to the amount of the pump energy that is absorbed in the sample. Following the approach of Hamilton et al.[19] we derive more general expression which relates gain, excited-state absorption and ground-state absorption cross-sections with the pump- and probe-beam parameters. These results are used to determine the effective gain cross-section in chromium-doped forsterite.

Consider a general case when the crystal has ground-state absorption, excited-state absorption and gain for the wavelength of the probe beam. If with Np(0) we denote the number of incident pump photons, the concentration of

excited-state ions produced when the pump beam travels through the sample can be written as

$$N_E(x,y,z,t) = \alpha_p \beta N_p(0) J(x,y) e^{-\alpha_p z} e^{-t/\tau} \quad (1)$$

where α_p is the ground-state absorption coefficient at the pump-beam wavelength, β the pumping quantum efficiency, J is the transverse spatial profile of the pump beam normalized to unity, and τ is the lifetime of the excited state assumed to be much longer than the duration of the pump-pulse. If the probe pulse arrives at time t much shorter than τ the factor $e^{-t/\tau}$ can be taken to be equal to unity. If we make further assumption that $\beta \sim 1$, i. e. that each photon absorbed in the crystal creates one excited ion, for times much shorter than τ we can write:

$$N_E(x,y,z,t) = \alpha_p N_p(0) J(x,y) e^{-\alpha_p z} \quad (2)$$

On its way through the sample the probe beam is amplified due to stimulated emission and is absorbed by both the excited-state and ground-state ions. If we assume that the probe pulse arrives at time short compared to τ and that its duration is much shorter than τ, the change in the probe-beam flux given by $f = N_{PR}(z) j(x,y)$ in a length element dz due to ground-state absorption, excited-state absorption and optical gain can be written as

$$df = [\sigma_E N_E(x,y,z) - \sigma_{ESA} N_E(x,y,z) - \sigma_G N_G(x,y,z)] j(x,y) N_{PR}(z) dz \quad (3)$$

where

$$N_G(x,y,z) = N_O - N_E(x,y,z). \quad (4)$$

N_O is the total concentration of active ions in the crysatal, assumed to be constant all over the crystal, $j(x,y)$ is the normalized transverse spatial profile of the probe

beam, and $N_{PR}(z)$ is the number of probe-beam photons along the sample. Combining (3) and (4) we obtain

$$df = [(\sigma_E + \sigma_G - \sigma_{ESA})N_E(x,y,z) - \sigma_G N_O]j(x,y)N_{PR}(z)dz \qquad (5)$$

Substituting eq. (2) into (5) and integrating over the transverse coordinates x and y and taking $df = dN_{PR}(z)$ we have

$$dN_{PR}(z) = [(\sigma_E + \sigma_G - \sigma_{ESA})\alpha_p N_p(0)We^{-\alpha_p z} - \sigma_G N_O]N_{PR}(z)dz \qquad (6)$$

where

$$W = \iint j(x,y)J(x,y)dxdy \qquad (7)$$

is the overlap integral of the pump and probe beam profiles. For two concentric Gaussian profiles $W = [\pi R^2(1 + r^2/R^2)]$. Integrating Eq. (6) along the sample of length L we obtain:

$$\ln[N_{PR}(L)/N_{PR}(0)] = (\sigma_E + \sigma_G - \sigma_{ESA})WN_P(0)(1 - e^{-\alpha_p L}) - \sigma_G N_O L \qquad (8)$$

$N_P(0)(1 - e^{-\alpha_p L}) = N_{Pabs}$ is the total number of pump photons that is absorbed in the crystal and $\alpha_G = \sigma_G N_O$ is the ground-state absorption coefficient for the probe-beam wavelength. $N_{PR}(0)$ and $N_{PR}(L)$ are the number of incident and transmitted probe photons, respectively. Now we can write

$$\ln[N_{PRp}(L)/N_{PRp}(0)] = (\sigma_E + \sigma_G - \sigma_{ESA})WN_{Pabs} - \alpha_G L \qquad (9)$$

for the case when the pump beam is on. When the pump beam is blocked Eq. (9) reduces to

$$\ln[N_{PRu}(L)/N_{PRu}(0)] = -\alpha_G L. \qquad (10)$$

Signals monitored by fast germanium detectors before the sample (S1) and behind the sample (S2) are proportional to the intensities of the incident and transmitted probe beam, respectively. For the pumped case

$$S_{1p} = k_1 N_{PRp}(0) \tag{11}$$

and

$$S_{2p} = k_2 N_{PRp}(L) \tag{12}$$

where k_1 and k_2 are constants of proportionality. For the unpumped case

$$S_{1u} = k_1 N_{PRu}(0) = S_{1p} = k_1 N_{PRp}(0) \tag{13}$$

and

$$S_{2u} = k_2 N_{PRu}(L) \tag{14}$$

Let us define ratio R as

$$R = (S_{2p}/S_{1p})/(S_{2u}/S_u) = [N_{PRp}(L)/N_{PRp}(0)]\,/[N_{PRu}(L)/N_{PRu}(0)] \tag{15}$$

or

$$R = [N_{PRp}(L)]/[N_{PRu}(L)]. \tag{16}$$

Combining (9), (10) and (16) we obtain

$$\ln R = (\sigma_E + \sigma_G - \sigma_{ESA}) W N_{Pabs} \tag{17}$$

Eq. (17) is the key equation describing the pump-and-probe experiment. It was used to estimate a number of important laser parameters using experimental data obtained from pump-and-probe experiments.

4.6.2 Calculation of the Stimulated Emission Cross Section

The stimulated emission cross section at freqency ν is given by the relation:

$$\sigma_E(\nu) = (\lambda_0^2/8\pi n^2 \tau) g(\nu,\nu_0) \quad (1)$$

where λ_0 is the wavelength of the peak of the emission line, n is the index of refraction of the host crystal, τ is the spontaneous emission radiative lifetime, $g(\nu,\nu_0)$ is the normalized lineshape function obtained from the emission spectrum, ν_0 is the center frequency, and ν is frequency in units of Hz. The normalized line shape function is obtained from the fluorescence spectrum with the relation[20]

$$g(\nu,\nu_0) = I_n(\nu,\nu_0)/\Delta\nu_{eff} \quad (2)$$

where $I_n(\nu,\nu_0)$ is the fluorescence intensity distribution (photon emission rate per unit frequency) normalized with respect to the peak value, i.e.

$$I_n(\nu,\nu_0) = I(\nu,\nu_0)/I(\nu_0), \quad (3)$$

and $\Delta\nu_{eff}$ is the effective width (full-width-at-half-maximum) of the emission spectrum. The cross section is then given by

$$\sigma_E(\nu) = (\lambda_0^2/8\pi n^2 \tau) I_n(\nu,\nu_0)/\Delta\nu_{eff}. \quad (4)$$

From the room temperature fluorescence spectrum shown in Fig. 4.3.1, it was found that $\Delta\nu_{eff} = 3.65 \times 10^{13}$ Hz, and from the lifetime measurements the radiative lifetime τ is taken to be equal to the liquid nitrogen temperature value of 25 μs. Using n = 1.64, the peak stimulated emission cross section at λ = 1140 nm (for $I_n(\nu,\nu_0) = 1$) is calculated to be $\sigma_E(\lambda = 1140\ nm) = 2.11 \times 10^{-19}\ cm^2$. At λ = 1200 nm from the fluorescence spectrum we find $I_n(\nu,\nu_0) = 0.85$ which gives $\sigma_E(\lambda =$

1200 nm) = 1.79 x 10^{-19} cm^2. These values are in excellent agreement with the values measured by the pump-and-probe technique.

4.6.3 Estimate of the Wavelength of the Peak ESA

ESA is expected to originate from the relaxed excited state. The fluorescence spectrum can be used to determine a value of Dq/B for the relaxed excited state using the formula[20]

$$(Dq/B)_{RES} = E(^3T_2 \rightarrow {}^3A_2)/10B \qquad (1)$$

where $E(^3T_2 \rightarrow {}^3A_2)$ is the energy of the zero-phonon line of the fluorescence band, and the value of the Raccah parameter B is assumed to remain unchanged by the variation of the Cr^{4+} - O^{2-} distance. From the low temperature fluorescence spectrum shown in Fig. 3.2.6 the energy of the zero-phonon line emission at 1093 nm is found to be 9,150 cm^{-1}. The value of the Raccah parameter B was estimated in Chapter 2 to be 970 cm^{-1}. Using formula (1) we obtain $(Dq/B)_{RES}$ = 0.94.

Diagonalizing the Tanabe-Sugano matrices (given in the Appendices of Chapter 2) using the above values for Dq and B and using the fluorescence spectrum, energies of the relaxed $^3T_2$ state and the first next excited state, $^3T_1$ can be determined. The excited-state absorption, if any, most likely arises from the $^3T_2 \rightarrow {}^3T_1$ transition. The difference between the two energies should give the expected wavelength of the peak of ESA.

From the zero-phonon line of the fluorescence spectrum energy of the relaxed excited state has been determined to be $E(^3T_2)$ = 10Dq = 9,150 cm^{-1}. Tanabe-Sugano matrix for the $^3T_1$ state gives $E(^3T_1)$ = 15,150 cm^{-1}. The energy difference is then

$$E(^3T_1) - E(^3T_2) = \sim 6{,}000\ cm^{-1}.$$

This energy corresponds to the wavelength of 1670 nm where the peak of the ESA may be expected according to the single-configuration-coordinate model. This has yet to be shown experimentally.

4.7 References

1. V. Petričević, S. K. Gayen, R. R. Alfano, K. Yamagishi, H. Anzai, and Y. Yamaguchi, Appl. Phys. Lett. 52, 1040 (1988).

2. V. Petričević, S. K. Gayen, and R. R. Alfano, Appl. Phys. Lett. 53, 2590 (1988).

3. H. R. Verdun, L. M. Thomas, D. M. Andrauskas, T. M. Collum, and A. Pinto, Appl. Phys. Lett. 53, 2593 (1988).

4. V. Petričević, S. K. Gayen, and R. R. Alfano, Opt. Lett. 14, 612 (1989).

5. V. Petričević, S. K. Gayen, and R. R. Alfano, Appl. Opt. 28, 1609 (1989).

6. V. Petričević, S. K. Gayen, and R. R. Alfano, in *Tunable Solid-State Lasers*, Vol. 5 of the OSA Proceeding Series, M. L. Shand and H. P. Jenssen, eds. (Optical Society of America, Washington, D.C., 1989), pp. 77-84.

7. H. R. Verdun, L. M. Thomas, and D. M. Andrauskas, in *Tunable Solid-State Lasers*, Vol. 5 of the OSA Proceeding Series, M. L. Shand and H. P. Jenssen, eds. (Optical Society of America, Washington, D.C., 1989), pp. 85-92.

8. R. Moncorge, D. J. Simkin, G. Cormier, and J. A. Capobianco, in *Tunable Solid-State Lasers*, Vol. 5 of the OSA Proceeding Series, M. L. Shand and H. P. Jenssen, eds. (Optical Society of America, Washington, D.C., 1989), pp. 93-97.

9. W. Koechner, *Solid-State Laser Engineering*, Second Edition, Springer-Verlag, New York,1988, p. 15.

10. R. Moncorge and T. Benyattou, Phys. Rev. B 37, 9177 (1988).

11. S. A. Payne, L. L. Chase, and G. D. Wilke, Phys. Rev. B 37, 998 (1988).

12. R. Clausen and K. Petermann, IEEE J. Quantum Electron. 24, 1114 (1988).

13. J. Caird, S. A. Payne, P. R. Staver, A. J. Ramponi, L. L. Chase, and W. E. Krupke, IEEE J. Quantum Electron. 24, 1077 (1988).

14. M. L. Shand and J. C. Walling, IEEE J. Quantum Electron. QE-18, 1152 (1982).

15. P. F. Moulton, J. Opt. Soc. Am. B 3, 125 (1986).

16. A. P. Shkadarevich, in *Tunable Solid-State Lasers*, Vol. 5 of the OSA Proceeding Series, M. L. Shand and H. P. Jenssen, eds. (Optical Society of America, Washington, D.C., 1989), pp. 60-65.

17. G. M. Zverev and A. V. Shestakov, in *Tunable Solid-State Lasers*, Vol. 5 of the OSA Proceeding Series, M. L. Shand and H. P. Jenssen, eds. (Optical Society of America, Washington, D.C., 1989), pp. 66-70.

18. V. Petričević, A. Seas, and R. R. Alfano, to be published.

19. D. S. Hamilton, S. K. Gayen, G. J. Pogatshnik, R. D. Ghen, and W. J. Miniscalco, Phys. Rev. B 39, 8807 (1989).

20. J. A. Caird, S. A. Payne, P. R. Staver, A. J. Ramponi, L. L. Chase, and W. F. Krupke, IEEE J. Quantum Electron. 24, 1077 (1988).

CHAPTER 5

SUMMARY AND FUTURE DIRECTIONS

5.1 Summary

5.1.1 Laser Performance of Chromium-Doped Forsterite

Pulsed laser operation was obtained with samples rich in Cr^{4+} in a stable cavity.[1-3] Pulsed laser action was observed for both the 1064-nm and 532-nm pumping. The spectra of the free-running laser radiation for both the 1064-nm and 532-nm pumping peaked at 1235 nm and had linewidth of 30 nm and 27 nm, respectively. Highest slope efficiency obtained to date is ~23% for 1064-nm pumping with an output mirror having 13% transmission at 1200 nm.

Surface damage of the $Cr:Mg_2SiO_4$ crystal was observed for pumping energies greater than 4 mJ of energy incident on the crystal, for 5-ns pulses, at 10 Hz repetition rate, focused to a 250 μm radius spot. This corresponds to damage threshold energy density greater than 6 J/cm^2, for 5-ns pulses. This means that a 1-cm-diameter laser-pumped forsterite rod can be used to generate pulses of energy in the joule range.

Continuous-wave laser operation was obtained using 1064-nm radiation from a cw Nd:YAG laser as a pumping source.[5] The lasing threshold was 1.25 W of absorbed power. The measured slope efficiency was 6.8%. The spectrum of the free-running laser output peaks at 1244 nm and has a bandwidth of 12 nm.

Tunable operation of Cr:forsterite laser has been demonstrated over the 1167 - 1345 nm spectral range.[4] A birefringent, single crystal quartz plate at Brewster's angle was used as the intracavity dispersive element. Three different output mirrors with transmission in adjacent wavelenth ranges were used to cover the range.

Maximum slope efficiency measured to date of 38 % was obtained for cw operation using 13 % transmission output mirror.

Limiting slope efficiency of the chromium-doped forsterite laser in the absence of passive losses was estimated to be >65 %.

Excited-state absorption is not a major loss mechanism in chromium-doped forsterite. The peak of the excited-state absorption is predicted at 1670 nm, far out of the tuning range.

Most important spectroscopic and laser parameters of Cr:Mg_2SiO_4 are compared with laser parameters of most important commercially available solid state lasers in Table 5.1.1.

TABLE 5.1.1: Basic Laser Properties of Nd:YAG, Alexandrite, Ti:Sapphire, and Cr:Forsterite Lasers

Property	Nd:YAG	Alexandrite	Ti:Sapphire	Cr:Forsterite
Chemical Formula	$Nd^{3+}:Y_3Al_2O_{12}$	$Cr^{3+}:BeAl_2O_4$	$Ti^{3+}:Al_2O_3$	$Cr:Mg_2SiO_4$
Typical Doping Level	1 at. % (1.38×10^{20} cm^{-3})	0.05-0.3 at. % ($0.18\text{-}1\times10^{20}$ cm^{-3})	0.01-0.1 wt. % ($0.3\text{-}3.3\times10^{19}$ cm^{-3})	0.02-0.04 at. % ($0.5\text{-}1\times10^{19}$ cm^{-3})
Laser Wavelength	1064 nm	700-818 nm	660-1100 nm	1167-1345 nm
Spontaneous Lifetime	230 μs	262 μs	3.2 μs	2.7 μs
Radiative Lifetime	550 μs	1.5 ms (^2E) 6.6 μs ($^4T_2$)	3.9 μs	25 μs
Stimulated Emission Cross Section	6.5×10^{-19}	7×10^{-21}	4.1×10^{-19}	2×10^{-19}
Surface Damage Threshold	>3 GW			>0.4 GW
Scattering Loss	0.002 cm^{-1}			0.02 cm^{-1}
Slope Efficiency (Laser Pumping)		71 %	>60 %	23 % (pulsed) 38 % (cw)
Limiting Slope Efficiency		68 ± 10 %		>65 %

5.1.2 Spectroscopic Properties of Chromium-Doped Forsterite

Measurements of the absorption, emission and excitation spectra, as well as the wavelength dependence of fluorescence lifetime provide convincing evidence that chromium ion may enter forsterite (Mg_2SiO_4) host in more than one valence states, as shown in Chapter 2. Trivalent chromium (Cr^{3+}) enters substitutionally for divalent magnesium (Mg^{2+}) in two inequivalent octahedrally coordinated sites, while tetravalent chromium (Cr^{4+}) substitutes for Si^{4+} at tetrahedrally coordinated sites. Of the two Cr^{3+} centers, the one with mirror symmetry (C_s) is optically active due to lack of inversion symmetry and accounts for a number of features in the absorption and emission spectra. The center with inversion symmetry (C_i) is characterized with longer lifetimes that show strong temperature dependence. Features attributed to the Cr^{3+} ion in the inversion site are much more prominent in the sample 1 which has higher chromium ion concentration. The absorption and emission due to transitions within the states of Cr^{4+} ion overlap with those within the states of Cr^{3+} ion. The absorption in the near infrared spectral region between 850 and 1150 nm is primarily due to transitions between the $^3A_2$ ground state and the first excited state $^3T_2$, of the Cr^{4+} ion. The four-level, vibronic mode of laser operation in Cr-doped forsterite feeds on $^3T_2 \rightarrow {}^3A_2$ transition.

5.2 Future Directions

5.2.1 Spectroscopic Studies

There are still several outstanding questions to be addressed with the use of conventional spectroscopy, such as energy transfer between different active centers (important for flashlamp pumping), polarization dependence of the absorption and emission spectra, methods of charge compensation (trivalent Cr^{3+} substitutes for divalent Mg^{2+}) etc.

Time-resolved spectroscopy is expected to provide answers on the dynamics between various levels relevant to laser operation.

Raman spectroscopy will give information about lattice dynamics and vibrational processes which are crucial for vibronic laser operation.

5.2.2 Development of Various Modes of Laser Operation

All possible modes of operation, such as continuous-wave, pulsed, Q-switched and mode-locked operation, as well as different pumping techniques, including laser-diode pumping, may be investigated.

Flashlamp pumping is very important mode of operation for many applications. Since Cr:forsterite has relatively short fluorescence lifetime, for efficient pumping a pump source with shorter pulses is needed to match the fluorescence lifetime. This mode of operation will make passive mode locking (using saturable absorber dyes) and Q-switching possible. High damage threshold promises generation of nanosecond pulses in the Joule-range.

Semiconductor diode pumping offers all-solid-state configuration which is expected to be very reliable with possibility of scaling.

Wide emission band makes generation of ultrafast pulses in the femtosecond range possible through mode-locked operation. Attractive techniques for obtaining a mode locked operation are by synchronous pumping, additive pulse mode locking and active mode-locking using an acoustooptic modulator.

5.2.3 Development of New Cr^{4+}-Ion Based Tunable Solid State Lasers

Chromium-doped forsterite ($Cr:Mg_2SiO_4$) is an important laser system for the near infrared spectral range. We have demonstrated room-temperature pulsed laser action in this crystal for both the 532-nm and 1064-nm excitation[1-3], tunability over the 1167-1345 nm spectral range[4], and continuous-wave laser operation for 1064-nm pumping at room temperature[5]. Successful room temperature laser operation of chromium-doped forsterite was originally attributed to Cr^{3+} ion substituting for Mg^{2+} in the octahedrally coordinated site with mirror symmetry (C_s). Spectroscopic investigations that followed, as well as laser operation of chromium-doped forsterite for near infrared pumping[2,3,6] indicated that a center other than Cr^{3+} is responsible for laser action in the near infrared spectral region. This center was identified[3,6] as Cr^{4+} substituting for Si^{4+} in a tetrahedrally coordinated site. Most recent spectroscopic studies performed on chromium-doped forsterite crystals grown under different conditions (in different oxygen partial pressures) and calculations using Tanabe-Sugano formalism[6] offer convincing evidence that tetrahedrally coordinated Cr^{4+} is really the lasing ion in chromium-doped forsterite.

Tetrahedrally coordinated Cr^{4+} is presumably the lasing ion in chromium-doped YAG.[7-9]

In the future, we plan to extend our research efforts to other low field host crystals, such as silicates, titanites and germanates, doped with Cr^{4+} as an active ion. Tunable solid-state lasers based on tetravalent chromium are expected to cover the 1 - 2 μm range which is of great importance for optical communications, remote sensing, eye-safe ranging, lidar, scientific and various medical applications. Spectroscopic and laser properties of these new crystals will be investigated. We also plan to continue the experimental studies for better understanding of the role of Cr^{4+} responsible for laser action in crystals that will be developed.

Earlier spectroscopic work[10] on chromium-doped forsterite was based on the assumption that only trivalent chromium (Cr^{3+}) substitutes for the octahedrally coordinated Mg^{2+} ions in Mg_2SiO_4 host. There are two inequivalent Mg^{2+} sites in forsterite, one with mirror symmetry (C_s) and the other with inversion symmetry (C_i). Trivalent chromium ion enters the inversion and the mirror site in a ratio of 3:2. Our recent spectroscopic measurements indicate that, in addition to Cr^{3+} ions in those sites, tetrahedrally coordinated Cr^{4+} ions are also present in the Czochralski-grown forsterite.

When a transition-metal ion is incorporated in a host crystal during the crystal-growing process its free-ion energy levels split due to the crystal field produced by surrounding (so-called ligand) ions. The effect of ligand ions around the impurity ion depends on the number of of ligand ions around the impurity ion and the symmetry of the site occupied by the impurity ion. Cr^{3+}, the most common lasing ion, always occupies octahedral sites, surrounded by six ligand ions.

In tetrahedral coordination, the transition-metal cation such as Cr^{4+} sits at the center of a tetrahedron surrounded by four anion ligands. Tetrahedral coordination produces lower crystal field splittings than octahedral coordination. For equal ligand ion charges and transition-metal impurity ion - ligand distances the ratio of the tetrahedral to octahedral crystal field strength is given by[11]

$$Dq(tet)/Dq(oct) = -4/9$$

The most important consequence of this relation is that the absorption and the Stokes-shifted luminescence of ions residing in a tetrahedral environment is expected to shift significantly into infrared spectral region. Consequently, tunable laser operation is expected to cover the range between 1 - 2 μm. This is best illustrated by Tanabe-Sugano diagram for $3d^2$ ion such as Cr^{4+} in tetrahedral coordination shown in Figure 1. Assuming the crystal field splitting 10Dq~10,000 cm^{-1} and Raccah parameter for Cr^{4+} B~1,000 cm^{-1} it is obvious that the emission should occur in the 1 - 2 μm spectral region. This is indeed the case for Cr^{4+} in forsterite and YAG. This lead us to believe that Cr^{4+} is a transition-metal ion which, when incorporated in different dielectric crystal hosts, can exhibit laser action in different parts of infrared region due to different crystal fields acting on Cr^{4+} ion.

Very important feature of $3d^2$ ions in tetrahedral sites, as seen from the Tanabe-Sugano diagram, is the existence of 3 spin-allowed absorption bands, indicated in the diagram, which is of great importance for efficient laser pumping, especially for flashlamp pumping. Due to lack of inversion symmetry, electric dipole transitions with high transition strengths are expected.

Another important aspect of Cr^{4+} substituting for tetravalent cation, such as Si^{4+} in forsterite, is that tetrahedral site provides ideal environment for covalent

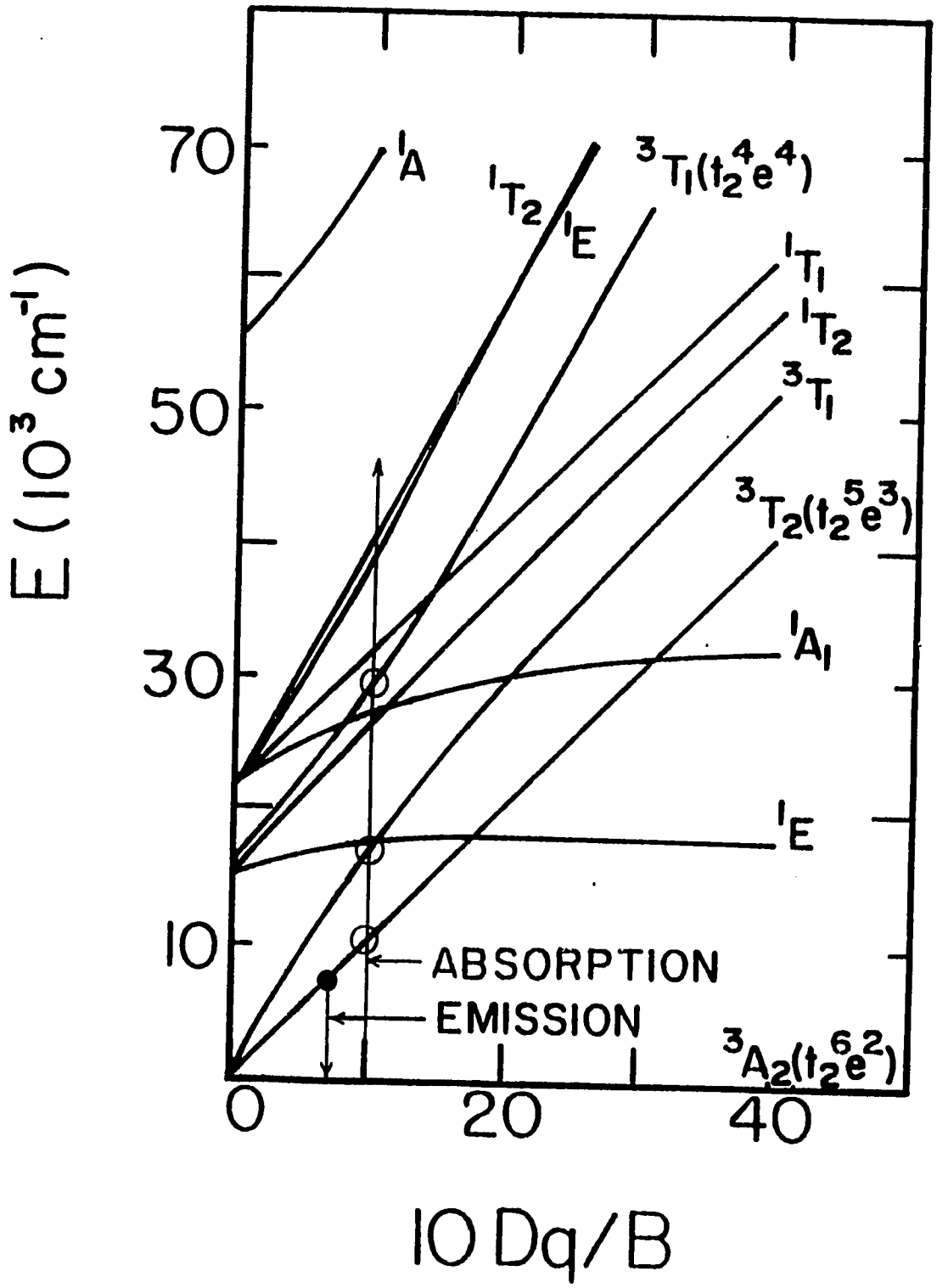

Figure 1. Tanabe-Sugano diagram for Cr^{4+} in tetrahedral coordination

bonding with surrounding ligand ions, such as divalent oxygen. High covalency of Cr(IV)-O(II) bond in forsterite can account for high chemical stability against both the oxidation and reduction of the Cr^{4+} ion.

Many known laser crystal hosts posses both octahedral and tetrahedral sites. Trivalent chromium (Cr^{3+}) shows strong preference for octahedrally coordinated sites[12]. It has been shown[3,6] that in at least one crystal (forsterite, Mg_2SiO_4), having both octahedral and tetrahedral sites, some of the chromium ions of tetravalent state can be forced to substitute for Si^{4+} in tetrahedral sites. This was accomplished by growing the crystal in more oxidizing atmosphere (with higher oxygen partial pressure). It has also been known[13] that in garnets presence of divalent impurities (such as Ca^{2+} or Mg^{2+}) promotes formation of an optically active center tentatively identified as Cr^{4+}in tetrahedral coordination. Therefore, it is possible, either by controlling the crystal-growing atmosphere, or by changing the starting materials for crystal-growing process, to incorporate tetravalent chromium (Cr^{4+}) into tetrahedral sites of the host crystal.

By controlling the growing process Cr^{4+} can be incorporated in tetrahedral sites in a variety of other materials such as silicates, germanates and titanites. Germanates and titanites are particularly promising since there is better size match of the ionic radii, and larger infrared shift is expected due to bigger size of the Ge or Ti tetrahedra, and consequently smaller crystal field at the Ge or Ti site.

Cr^{4+} in these proposed hosts will form new important class of tunable solid state lasers for 1 - 2 μm wavelength region with unique properties. Cr^{4+} in tetrahedral sites forming covalent bond with surrounding oxygen ions will be chemically stable. The wavelength range these lasers are expected to cover is of great technological importance. Most of the proposed host materials are nontoxic, of good

thermomechanical and optical properties and are relatively easy to grow by Czochralski, Bridgman or hydrothermal growth method.

5.2.4 Applications

The unique properties of forsterite laser make it a prime candidate for many practical applications in a variety of fields. Some examples are laser radar (lidar), night vision technology, remote sensing, countermeasures, semiconductor diagnosis, medical (eye surgery, HPD using the second harmonic), and optical communication. In all of these fields scientists are searching for an all solid state, compact, tunable laser in the near infrared region.

Particularly interesting area of future development may be finding application of Cr^{4+}-based laser materials in optical communications.

The unique features of this new solid-state laser system is that its tuning range includes the wavelength of minimal dispersion in optical fibers. Tuning range of future Cr^{4+}-based laser sytems that will be developed is expected to include both the wavelengths of minimal dispersion (1.3 μm) and minimal attenuation (1.55 μm) in optical fibers. High power continuous-wave lasers with fast optical modulators may be developed to be used as drivers in optical communications systems. Tunable solid-state laser crystals are ideal gain medium for optical amplifiers. Various configurations of optical amplifiers for 1 - 2 μm range will be developed for fiber-optic communications systems.

Another important direction to follow is development of active fibers which may be used as optical amplifiers in fiber-optic communications systems. Rare-earth-doped fibers are emerging as an alternative to conventional semiconductor-

laser amplifiers. Transition-metal-ion-doped fibers may have significant advantages, primarily due to their wavelength tunability. Single-crystal fibers of high crystalline perfection and near theoretical strength can be grown by laser-heated pedestal growth method. Single-crystal or polycrystalline fibers doped with Cr^{4+} and other transition metal ions can be developed for tunable fiber laser oscillators and amplifiers in the wavelength range of minimal loss and minimal dispersion.

5.3 References

1. V. Petričević, S. K. Gayen, R. R. Alfano, K. Yamagishi, H. Anzai, and Y. Yamaguchi, Appl. Phys. Lett. **52**, 1040 (1988).

2. V. Petričević, S. K. Gayen, and R. R. Alfano, Appl. Opt. **27**, 4162 (1988).

3. V. Petričević, S. K. Gayen, and R. R. Alfano, Appl. Phys. Lett. **53**, 2590 (1988).

4. V. Petričević, S. K. Gayen, and R. R. Alfano, Appl. Opt. **28**, 1609 (1989).

5. V. Petričević, S. K. Gayen, and R. R. Alfano, Opt. Lett. **14**, 612 (1989).

6. V. Petričević, S. K. Gayen, and R. R. Alfano, in *Tunable Solid-State Lasers*, Vol. 5 of the OSA Proceeding Series, M. L. Shand and H. P. Jenssen, eds. (Optical Society of America, Washington, D.C., 1989), pp. 77-84.

7. N. B. Angert, N. I. Borodin, V. M. Garmash, V. A. Zhitnyuk, A. G. Okhrimchuk, O. G. Siyuchenko, and A. V. Shestakov, Sov. J. Quantum Electron. **18**, 73 (1988).

8. A. I. Shkadarevich, Presented at Fifth International Conference on Tunable Lasers, Irkutsk, U. S. S. R., Sept. 20-22, 1989.

9. N. I. Borodin, V. A. Zhitnyuk, A. G. Okrimchuk, and A. V. Shestakov, Presented at Fifth International Conference on Tunable Lasers, Irkutsk, U. S. S. R., Sept. 20-22, 1989.

10. H. Rager and G. Weiser, Bull. Mineral. **104**, 603 (1981).

11. F. A. Cotton, *Chemical Applications of Group Theory*, Wiley-Interscience, New York, (1971).

12. J. A. Caird, in *Tunable Solid-State Lasers II*, A. B. Budgor, L. E. Esterowitz, and L. G. DeShazer, editors, Springer-Verlag (1986).

13. S. E. Stokowski, M. H. Randles, and R. C. Morris, IEEE J. Quantum Electron. 24, 934 (1988).